Incoherent Projection Moire Contour Sensing with Coherent Processing for Large Structures

by

Melanie N. Ott

Thesis submitted to the Faculty of the

Virginia Polytechnic Institute and State University

in partial fulfillment of the requirements for the degree of

Master of Science

in

Electrical Engineering

APPROVED:

Richard O. Claus

Dr. Richard O. Claus, Chairman

G Indebetouw

Dr. Guy Indebetouw

Kent A. Murphy

Dr. Kent Murphy

Sharon L. Welch

Ms. Sharon Welch

October, 1993

Blacksburg, Virginia

Incoherent Projection Moire Contour Sensing with Coherent Processing for Large Structures

by

Melanie N. Ott

Dr. Richard O. Claus, Chairman

Bradley Department of Electrical Engineering

Virginia Polytechnic Institute and State University

(ABSTRACT)

This paper presents the theory and results of three Moire methods 1) the incoherent projection Moire method, 2) the electronic phase detection method, and 3) the fringe multiplication method. It is proposed that these three methods be used together in a system to measure out of plane displacements of large diffusely reflecting surfaces. The operation of the system is divided into two processes. The first process records an incoherent moire pattern which contains the out of plane displacement information. The second process uses a transduced coherent image of the pattern produced in the first process to optically generate a quantiative result with variable sensitivity. The coherent processing is a technique that uses the fringe multiplication method with the electronic phase detection method. The result is the quantitative, out of plane displacement measurement with sensitivity enhancement that can be altered during coherent processing of the Moire fringe pattern.

ACKNOWLEDGEMENTS

I would like to thank Dr. Richard O. Claus, director of the Fiber and Electro Optics Research Center, who has been a great influence througout my education, for inspiring me to continue my formal education and for providing the opportunity for me to learn and experience the fascinating field of optics. With his enthusiasm and humor he has taught me to take myself less seriously while empowering my desire to learn. I admire and appreciate the commitment he has to his students that goes beyond the call of duty. I would like to thank Dr. Guy Indebetouw for teaching me an intuitive understanding of Fourier transforms, for his patience and time when answering my many questions, and for being a brilliant optics professor. I thank Dr. Kent Murphy for teaching me valuable practical lab skills, inspiring me creatively and for his incredible sense of humor. I would like to thank Ms. Linda Jones for her immense wisdom, good judgment and for being a good friend. At NASA Langley Spacecraft Controls Branch, I thank my sponsor and mentor Ms. Sharon Welch for sharing her philosophies with me, providing technical leadership on this project, teaching me writing skills, research skills and all about diffraction theory. For practical support, technical education, and friendship I thank: David Cox, Walter "Gumbi" Duncan and Kevin Shelton. I thank John Franke for his enthusiastic technical assistance. For laboratory support I thank Jim Clemmons. I would like to thank my very good friend Shari Feth, who is very understanding, an incredible support always, and I love very much. Most of all I would like to thank my husband Bill Miller for his love, devotion, emotional support, and for holding me when I cry. I would like to thank my mother for teaching me endurance and that what doesn't kill you only makes you stronger. I dedicate this thesis to my parents Earl and Sheila Oyer who are facing a turning point in their lives as I face a turning point in mine.

TABLE OF CONTENTS

1.0. Introduction 1

1.1. Problem Statement 1

1.2. Fringe Projection Moire for Surface Shape Sensing 2

1.3. Outline 3

2.0. The Theory of Projection Moire 4

2.1. Description of Fringe Projection Moire 4

2.1.1 Moire Pattern of Two Sinusoidal Gratings 4

2.1.2 The Moire Pattern of Two Ronchi Gratings 9

2.2. Analysis of the Moire Pattern Parameters 11

2.2.1 The Effects of Varying Pitch 11

2.2.2 The Effects of Varying Grating Alignment Angle 13

2.2.3 The Effects of Varying Viewing Angle 14

3.0. Interpretation of Moire Fringes 32

3.1 Intensity Based Phase Detection 32

3.2 Frequency Based Phase Detection 33

3.2.1 Theory of Electronic Phase Detection 34

3.2.2 Methods for Generating Moving Fringes 35

3.3 Coherent Optical Processing of Moire Fringes 38

3.3.1 Fringe Multiplication 38

3.3.2 Frequency Based Phase Detection of the Multiplied Moire Fringes ...45

4.0. Projection Moire at Large Scale 60

4.1 The Incoherent Projection Moire System 60

4.1.1 Source Power 60
4.1.2 Bandwidth 62
4.1.3 Range and Resolution 65
4.2 The Coherent Processing System 66
4.2.1 System Power Considerations 66
4.2.2 Bandwidth 69
4.2.3 Sensitivity 71
5.0 Experimental Results 83
5.1 Intensity Projection Moiré 83
5.1.1 Data Analysis of Intensity Patterns 84
5.1.2 Processing Results 85
5.2 Electronic Phase Detection 85
5.2.1 Data and Results 87
5.3 Fringe Multiplication 87
5.3.1 Experimental Results 88
6.0. Conclusions 107
7.0. References 109
Appendix A 112
Vita 116

LIST OF FIGURES

Chapter 2.0:

2.1 Schematic for Projection Moire.....15

2.2 Coordinate System Labels 16

2.3 Transmittance of Sinusoidal Amplitude Grating.....17

2.4a Plot of Equation 2.2.13 18

2.4b Plot of First Term in Equation 2.2.13.....19

2.4c Plot of Second Term in Equation 2.2.13.....20

2.5a Plot of First Term of Equation 2.1.12.....21

2.5b Plot of Second Term of Equation 2.1.12 22

2.6 Transmission of Ronchi Amplitude Grating 23

2.7a,b Moire Pattern Caused by Pitch Mismatch 24

2.8a,b Bar and Space Width of a Ronchi Gratings 25

2.9 Intensity Profile of Moire Fringes.....26

2.10a,b Fringe Contrast of Two Gratings 27

2.11 Moire Pitch Dependence on Angular Misalignment θ.....28

2.12a,b Moire Pattern Caused by Angular Misalignment.....29

2.13a,b Moire Pattern Caused by Angular Misalignment of Ronchi Gratings.....30

2.14 Sensitivity as a Result of Viewing Angle Variation 31

Chapter 3.0:

3.1 Acousto-Optic Modulator 46

3.2 Michelson Interferometer with One Moving Mirror.....47

3.3a,b Two Mirrors of a Michelson Interferometer.....48

3.4 Transducing from an Incoherent System to a Coherent System.....49

3.5 Double Diffraction from Two Gratings Superimposed.....50

3.6 Schematic for Fringe Multiplication.....51

3.7 Transmission of Ronchi Grating G_1.....52

3.8 Transmission of Ronchi Grating G_2.....53

3.9a F(u) for m = 1 and n from -9 to 9.....54

3.9b F(u) for m = 2 and n from -9 to 9.....54

3.9c F(u) for m = 3 and n from -9 to 9.....55

3.10a Magnitude of the n = 1st order of F(u) with m = 1.....56

3.10b Magnitude of the n = -1st order of F(u) with m = 1.....56

3.11a Magnitude of the n = 2nd order of F(u) with m = 1.....57

3.11b Magnitude of the n = -2nd order of F(u) with m = 1.....57

3.12 Magnitude of the n = 0th order of F(u) with m = 1.....58

3.13a F(u) with m = 1 and n = -4 to 4.....59

3.13b F(u) with m = 2 and n = -5 to 5.....59

3.13c F(u) with m = 3 and n = -6 to 6.....59

Chapter 4.0:

4.1 Transmission Coefficients of the mth Order Pair.....74

4.2 Transmission Coefficients for r Order Groups with m = 1.....75

4.3a Visibility of Fringes in r Groups for m = 1.....76

4.3b Visibility of Fringes in r Groups for m = 3.....77

Chapter 5.0:

5.1 Experimental Set-up for Intensity Projection Moire.....90

5.2 Unfiltered Data of Moire Vertical Intensity Plot for $z_0 = 0$.....91

5.3 Filtered Data of Vertical Moire Intensity Plot for $z_0 = 0$ 92

5.4 Center Four Fringes from the Moire Filtered Pattern with $z_0 = 0$ 93

5.5 Simulated Sinusoidal Fringe Pattern to Average Moire Fringe Group .....
Position 94

5.6 Out of Phase Sinusoidal Pattern and Moire Fringe Group, $z_0 = 0$ 95

5.7 Sinusoidal Pattern and Moire Fringe Group with $z_0 = 0$, In Phase 96

5.8 Sinusoidal Pattern and Moire Fringe Group with $z_0 = .635$, In Phase . .97

5.9 Experimental Data for Intensity Projection Moire (with Linear Fit).....98

5.10 Experimental Set-up for Phase Detection 99

5.11 Electronic Phase Detection Experimental Data (with Linear Fit).....100

5.12 Experimental Set-up for Fringe Multiplication.....101

5.13a Experimental Data for Fringe Multiplication with Grating Frequency
10 lp/mm and m = 1 102

5.13b Experimental Data for Fringe Multiplication with Grating Frequency
10 lp/mm and m = 3 102

5.14a Moire Pattern Using Fringe Multiplication of r Group = 0 and m
Order Pair =1.....103

5.14b Moire Pattern Using Fringe Multiplication of r Group = 0 and m
Order Pair = 3.....104

5.15a Moire Pattern Using Fringe Multiplication of r Group = - 1 and m
Order Pair = 1.....105

5.15b Moire Pattern Using Fringe Multiplication of r Group = - 3 and m
Order Pair = 3.....106

LIST OF TABLES

Chapter 4.0

4.1 Transmission Coefficients for r Order Groups with m = 1 78

4.2 Transmission Coefficients for r Order Groups with m = 3.....79

4.3 Transmission Coefficients for r Order Groups with m = 5.....80

4.4a Transmission Coefficients of m Order Pairs.....81

4.4b Transmission Coefficients of the r = 0 Order Group.....81

4.5 Sensitivity of h per unit degree for Odd Orders m =1 to 19 82

List of Symbols

The Incoherent Projection Moire System

G_A - first grating (projected grating)

G_B - second grating (reference grating)

p_o - pitch of first grating

p_B - pitch of second grating

p_A - pitch of the image of first grating in the plane of the second grating

M_A - magnification from projection optics to test surface

M_B - magnification from surface to second grating

M_C - magnification from the second grating to the CCD camera detector array

Σ - diffuse test surface

z_o - out of plane displacement of test surface

n_A - position index for Ronchi grating one

n_B - position index for Ronchi grating two

l_m - position index for Moire fringe pattern

N - total number of a quantity

c - index number

p - pitch of a grating

n - index of a grating

Δy - shift of moire fringes in y direction

p_{moire} - pitch of moire fringe pattern

ϕ - viewing angle

θ - grating misalighment angle

γ - angular rotation about the x axis

φ - angular rotation about the y axis

κ - angular rotation about the z axis

η - reflectivity of test surface

Δ_{CCD} - CCD camera pixel size

ζ, ξ - angles

P_s - source power

τ - transmittance of lenses used for projection

A_{col} - area of collimated projected beam

I_{GA} - intensity of collimated beam at the first grating

I_{Σ} - intensity of beam at surface

I_{GB} - intensity of image at second grating

$F_1^{\#}$ - f number of imaging lens to second grating

$F_2^{\#}$ - f number of imaging lens to CCD camera

I_{CCD} - intensity at CCD camera

I_{total} - intensity of moire pattern

S - sensitivity

T - transmittance

v - velocity of moving grating

D - window length of acousto optic cell

T_s - time window of acousto optic cell

V_s - velocity of sound in an acousto optic cell

F_{mod} - modulating frequency

p_{AO} - pitch of grating generated by acousto optic cell

t - time

d - distance difference between two mirrors

d_1 - distance from beamsplitter to mirror one of a michelson

d_2 - distance from beamsplitter to mirror two of a michelson

I - intensity

σ - angular misalignment of moving mirror

ω - frequency in radians

λ - wavelength of light

The Coherent Processing System

G_1 - first grating

p_1 - pitch of first grating

m - diffraction order of grating one

G_2 - second grating

p_2 - pitch of second grating

n - diffraction order of second grating

F - Fourier transform

k - spatial frequency

T_1 - transmittance of grating one

T_2 - transmittance of grating two

F_1 - filter one

F_2 - filter two

r - diffraction order of image at filter two

ρ - pitch of first grating image at second grating

h - translation of first grating

a_m - fourier component of grating one

a_n - fourier component of grating two

P_{sc} - coherent source power

τ_m - transmission coefficent from first filter

τ_r - transmission coefficent from second filter

P_{G_2} - power at second grating

P_{det} - power at detector

w_{det} - width of detector

v_{SLM} - velocity of scanning fringes in spatial light modulator

f_r - frame rate of spatial light modulator

t_{lenses} - transmission of system lenses

1.0 Introduction

1.1 Problem Statement

Development of sensors for control of large space structures is an on-going area of research. To reduce payload requirements, many structures are designed to be lightweight and as a result, are highly flexible. To control these structures and damp out vibrations in the presence of modelling uncertainties, sensors are required which can convey sufficient information to determine the states of the structures. This information, both spatial and temporal, is usually conveyed via a network of high temporal bandwidth sensors placed at strategic points on the structure [1].

Recent efforts have focused on the developments of embedded sensors including fiber optic and micro-sensors [2-4]. Embedded sensors have the advantages of enabling greater numbers of individual sensors to be placed on a structure, and thus increasing the spatial resolution, as well as reducing the weight and power requirements for sensing. However, for some controls problems, embedded sensors cannot provide the necessary measurement. An example of such problems include shape measurement and control of large segmented space telescopes and large segmented radiometers. Segmented mirrors on the order of 20 meters in diameter and segmented reflectors on the order of 40 meters in diameter have been proposed for future space telescopes and radiometers, respectively [5]. To control the shape of a large segmented reflector, it is necessary to maintain the alignment of one segment with repect to the neighboring segments to high accuracy and simultaneously maintain the overall shape of the reflector relative to a coordinate system fixed to the focal plane.

Currently, ground-based segmented telescopes with active control systems use a system of integrated sensors, that is, sensors attached to each of the panels to measure relative panel-to-panel alignment and another single wavefront sensor located near the focal plane to

measure the overall shape of the reflector [6-7]. Similar integrated sensing systems have been proposed for active space telescopes and a variety of wavefront sensor designs have been investigated for telescopes which operate in the visible and near infrared [8-10]. However, the designs of these wavefront sensors are not readily adapted to shape measurement of a large diffusely reflecting surface as found in a large segmented radiometer. Thus, the problem of optically sensing the shape of a large segmented radiometer for control purposes remains.

In this paper, one type of distributed optical sensing technique, fringe projection Moire, is analyzed for sensing the contour of a large diffusely reflecting surface. The spatial resolution and temporal bandwith are quantified and two techniques for increasing the spatial resolution are analyzed in detail.

1.2 Fringe Projection Moire for Surface Shape Sensing

Fringe projection Moire is an optical technique which can be used to measure the displacement of a surface or surface contour through incoherent imaging. Lord Rayleigh first described Moire around 1874 [11]. In 1948, Shepard introduced fringe projection Moire for contour measurement [12]. In the early 1970's the technique was studied again for surface contour measurement and many refinements of the technique were proposed [13-15]. Briefly, to measure the contour of a surface using fringe projection Moire, an image of a pattern, most often a striped pattern from a grating, is projected at an angle onto the surface. The surface and pattern are then imaged against a reference pattern and the interference of the image and reference patterns produces contour fringes which are the Moire pattern (figure 2.1). The shape and spacing of fringes will be a function of the angles of projection and viewing, the shape and spacing of the projected and reference patterns, and the height of the object at any point. Thus, if the angles of projection and

viewing are known, as well as the resolution of the projected and reference patterns, then the height of the object can be determined at each point from the phase of the fringes in the Moire pattern.

To improve the sensitivity of the measurement, or increase the resolution of height, it is necessary to interpolate between the contour fringes. Three approaches commonly used to interpolate between the fringes are: 1) digital image processing, 2) fringe multiplication, and 3) electronic phase detection [16-21]. The first technique is computationally intensive and typically done offline with interactive programs. Some algorithms have been developed in recent years for automatic fringe identification and interpolation, but are still computationally intensive and are not suitable for dynamic measurements [15]. For this reason, the first approach will not be considered in this paper. The second approach, which is optical, and the third, which is electronic, have potentially high temporal bandwidths. Therefore these two approaches have been analyzed in detail. The results of this analysis and the potential advantages and disadvantages of these two methods for improving resolution when sensing the contour of a large diffusely reflecting surface are the subjects of this thesis.

1.3 Outline

This thesis is organized as follows. In section 2, the theory of optical projection Moire for contour sensing is reviewed. In section 3, discusses the interpretation of the Moire fringes. Specifically, intensity-based and frequency-based phase measurements are described and fringe multiplication, a coherent method of processing the Moire fringes to improve resolution, is analyzed. Projection Moire is analyzed at large scale in section 4. Experimental results are presented for both methods of phase measurement and for fringe multiplication in section 5. Conclusions are presented in section 6.

2.0 The Theory of Projection Moire

2.1 Description of Fringe Projection Moire

Figure 2.1 illustrates the sensing geometry for the Moire fringe projection method used in this paper. An image of a transmission grating G_A, consisting of straight line fringes, is projected along the optical axis onto surface Σ whose contour is to be measured. The reflection of surface Σ and the projected pattern of G_A are focused by imaging optics at a viewing angle ϕ from the optic axis onto a plane containing a transmission grating G_B, which is a straight lined ruled grating. The Moire pattern created by the transmission of the image of surface Σ and the pattern from G_A through G_B is detected behind G_B. The spacing and phase of the Moire fringe pattern behind G_B is a function of viewing angle ϕ, the angular misalignment between the two gratings θ, (Figure 2.2) the difference in grating spacing and the surface height z_0, with respect to a zero reference position where $z_0 = 0$.

2.1.1 Moire Pattern of Two Sinusoidal Gratings

A sinusoidal amplitude grating G_A, of period or pitch p_0, is incoherently projected on to a surface Σ. The surface and projected grating are imaged onto a sinusoidal reference grating G_B. The Moire pattern behind G_B will contain information concerning differences in the two gratings as well as the position of surface Σ. The objective is to determine the out of plane displacement z_0, of the surface Σ. The details are examined here.

Let G_A be a sinusoidal amplitude grating of period or pitch p_0. Define a coordinate system (Figure 2.2) with the x axis perpendicular to the rulings of G_A, y axis parallel to the

rulings, and z axis coincident with the optic axis z' of the projection system.. Along x, the transmittance of G_A is

$$\frac{1}{2} + \frac{1}{2}\cos\left(\frac{2\pi x}{p_o}\right) \tag{2.1.1}$$

as shown in Figure 2.3. At every $x = cp_o$, where c = 0, 1, 2, 3.. the grating transmittance is maximum and at every $x = (2c + 1)p_o/2$ the transmittance is minimum. If this grating is rotated about the z axis by an angle $\kappa = \theta/2$, the new grating spacing is determined by the rotation of coordinates (Figure 2.2). Using the rotation matrix for a right handed Cartesian coordinate system with γ and $\varphi = 0$ (Appendix A) the relationship of the new coordinates x', y' to the current coordinates x, y is represented by

$$\begin{bmatrix} x' \\ y' \\ z' \end{bmatrix} = \begin{bmatrix} \cos\frac{\theta}{2} & -\sin\frac{\theta}{2} & 0 \\ \sin\frac{\theta}{2} & \cos\frac{\theta}{2} & 0 \\ 0 & 0 & 1 \end{bmatrix} \begin{bmatrix} x \\ y \\ z \end{bmatrix} . \tag{2.1.2}$$

The transmittance of G_A along x' is

$$\frac{1}{2} + \frac{1}{2}\cos\left(\frac{2\pi}{p_o}x\cos\left(\frac{\theta}{2}\right) - \frac{2\pi}{p_o}y\sin\left(\frac{\theta}{2}\right)\right) . \tag{2.1.3}$$

The intensity of the projected image of G_A on the flat surface Σ is the product of the intensity of the illumination and the transmittance of G_A multiplied by a magnification factor M_A. Assuming that the illumination is uniform over the field of view then the intensity at Σ is proportional to;

$$\frac{1}{2} + \frac{1}{2}\cos\left(\frac{2\pi}{M_A p_o}x\cos\left(\frac{\theta}{2}\right) - \frac{2\pi}{M_A p_o}y\sin\left(\frac{\theta}{2}\right) + \frac{2\pi}{M_A p_o}z_o\right) , \tag{2.1.4}$$

where z_o is the position of the flat surface along the z axis with respect to a zero reference (Figure 2.1).

The spacing and phase of the projected grating image of G_A in the plane of G_B are altered by the magnification M_B and the viewing angle ϕ. The relationship in grating spacing is determined by the transformation of coordinates from that of the projection plane to that of the image plane. Using the rotation matrix for a rotation around the y axis (Appendix A) by $\varphi = -\phi$ and $\gamma = \kappa = 0$, the relationship between coordinates is

$$\begin{bmatrix} x'' \\ y'' \\ z'' \end{bmatrix} = \begin{bmatrix} \cos\phi & 0 & -\sin\phi \\ 0 & 1 & 0 \\ \sin\phi & 0 & \cos\phi \end{bmatrix} \begin{bmatrix} x' \\ y' \\ z' \end{bmatrix} . \qquad (2.1.5)$$

The intensity pattern at G_B of the projected grating image given that $z' = z_o$ is proportional to

$$\frac{1}{2} + \frac{1}{2}\cos\left(\frac{2\pi}{M_B M_A p_o} x\cos\left(\frac{\theta}{2}\right)\cos\phi - \frac{2\pi}{M_B M_A p_o} y\sin\left(\frac{\theta}{2}\right) - \frac{2\pi M_B}{M_B M_A p_o} z_o \sin\phi\right) . \qquad (2.1.6)$$

Let the pitch of the grating image be

$$p_A = \frac{M_B M_A p_o}{\cos\phi} , \qquad (2.1.7)$$

then (2.1.6) is

$$\frac{1}{2} + \frac{1}{2}\cos\left(\frac{2\pi}{p_A} x\cos\left(\frac{\theta}{2}\right) - \frac{2\pi}{p_A\cos\phi} y\sin\left(\frac{\theta}{2}\right) - \frac{2\pi M_B}{p_A} z_o\tan\phi\right) . \qquad (2.1.8)$$

Assume that the grating G_B is the same sinusoidal amplitude type grating as G_A given in (2.1.1) with a pitch of p_B and is tilted about the z axis by an angle $\kappa = -\theta/2$. Using the same rotation matrix from (2.1.2) to determine the change in grating spacing as a result of coordinate transformation, the transmittance of G_B along x'' is

$$\frac{1}{2} + \frac{1}{2}\cos\left(\frac{2\pi}{p_B} x\cos\left(\frac{\theta}{2}\right) + \frac{2\pi}{p_B} y\sin\left(\frac{\theta}{2}\right)\right) . \qquad (2.1.9)$$

The intensity behind G_B is proportional to the product of the image intensity of G_A and the transmittance of G_B, and is,

$$I_{total} \propto \frac{1}{4} + \frac{1}{4}\cos\left(\frac{2\pi}{p_A}x\cos\left(\frac{\theta}{2}\right) - \frac{2\pi}{p_A\cos\phi}y\sin\left(\frac{\theta}{2}\right) - \frac{2\pi M_B}{p_A}z_o\tan\phi\right) + \frac{1}{4}\cos\left(\frac{2\pi}{p_B}x\cos\left(\frac{\theta}{2}\right) + \frac{2\pi}{p_B}y\sin\left(\frac{\theta}{2}\right)\right) + \frac{1}{4}\cos\left(\frac{2\pi}{p_A}x\cos\left(\frac{\theta}{2}\right) - \frac{2\pi}{p_A\cos\phi}y\sin\left(\frac{\theta}{2}\right) - \frac{2\pi M_B}{p_A}z_o\tan\phi\right)\cos\left(\frac{2\pi}{p_B}x\cos\left(\frac{\theta}{2}\right) + \frac{2\pi}{p_B}y\sin\left(\frac{\theta}{2}\right)\right). \quad (2.1.10)$$

The last term of (2.1.10) is the term that contains the expression for the Moire pattern. Using the identity

$$\cos\xi\cos\zeta = \cos(\xi + \zeta) + \cos(\xi - \zeta) \ , \quad (2.1.11)$$

the last term in (2.1.10) can be written as the sum and difference of the original cosine arguments as

$$\frac{1}{4}\cos\left(2\pi x\cos\left(\frac{\theta}{2}\right)\left(\frac{1}{p_A} + \frac{1}{p_B}\right) + 2\pi y\sin\left(\frac{\theta}{2}\right)\left(\frac{1}{p_B} - \frac{1}{p_A\cos\phi}\right) - \frac{2\pi M_B}{p_A}z_o\tan\phi\right) + \frac{1}{4}\cos\left(2\pi x\cos\left(\frac{\theta}{2}\right)\left(\frac{1}{p_A} - \frac{1}{p_B}\right) - 2\pi y\sin\left(\frac{\theta}{2}\right)\left(\frac{1}{p_B} + \frac{1}{p_A\cos\phi}\right) - \frac{2\pi M_B}{p_A}z_o\tan\phi\right) . \quad (2.1.12)$$

The second term (or the difference term) of (2.1.12) is the expression which describes the intensity of the Moire fringe pattern. If $p_A = p_B$ then (2.1.12) simplifies to

$$\frac{1}{4}\cos\left(4\pi x\cos\left(\frac{\theta}{2}\right)\left(\frac{1}{p_A}\right) + 2\pi y\sin\left(\frac{\theta}{2}\right)\frac{1}{p_A}\left(\frac{\cos\phi - 1}{\cos\phi}\right) - \frac{2\pi M_B}{p_A}z_o\tan\phi\right) + \frac{1}{4}\cos\left(2\pi y\sin\left(\frac{\theta}{2}\right)\frac{1}{p_A}\left(\frac{\cos\phi + 1}{\cos\phi}\right) + \frac{2\pi M_B}{p_A}z_o\tan\phi\right) . \quad (2.1.13)$$

Figure 2.4a is a graph of (2.1.13). Note that the magnitude of the function graphed in Figure 2.4a varies in both the x and y directions. Figure 2.4b shows a graph of the first term (or the sum term) in (2.1.13) which shows the variation in both x and y. The second

term of (2.1.13), which is the Moire term, is graphed in Figure 2.4c and displays the lowest frequency pattern of the Figures in 2.4 with a periodic variation in the y direction only. The variation in the y direction allows for the measurement of out of plane displacement, z_0 to be extracted as a phase shift of the Moire fringe pattern. Since the spatial frequency of the Moire pattern or second term in (2.1.13) is lower than that of the sum term and the other carrier patterns, the Moire pattern can be optically low pass filtered. To show more clearly that the spatial frequency of the Moire term can be much smaller than the sum term, 2.5a is a graph of the first term (sum term) in (2.1.12) with $z_0 = 0$, $\theta/2 = 0$, $\phi = 45$ degrees, $p_A = .333$ mm, and $p_B = .308$ mm. Figure 2.5b is the Moire term of (2.1.12) given the above parameters. It is apparent here that of the two terms in (2.1.12) the Moire term contains the lowest spatial frequency.

The information that determines the Moire pattern spacing and phase is contained in the argument of the Moire term in (2.1.13) when the argument is set equal to increments of 2π. Solving for y by equating the argument of the difference or Moire term to $2\pi l_m$,

$$y = \frac{l_m p_A}{\sin\left(\frac{\theta}{2}\right)}\left(\frac{\cos\phi}{\cos\phi + 1}\right) + \frac{M_B z_o \sin\phi}{\sin\left(\frac{\theta}{2}\right)}\left(\frac{1}{\cos\phi + 1}\right), \qquad (2.1.14)$$

which is the form: $y = l_m p_{moire} + \Delta y$ where $l_m = 0, 1, 2, 3...$ The pitch of the Moire pattern is

$$p_{moire} = \frac{p_A}{\sin\left(\frac{\theta}{2}\right)}\left(\frac{\cos\phi}{\cos\phi + 1}\right) \qquad (2.1.15)$$

and Δy the shift of the fringes in distance is

$$\Delta y = \frac{M_B z_o \sin\phi}{\sin\left(\frac{\theta}{2}\right)}\left(\frac{1}{\cos\phi + 1}\right). \qquad (2.1.16)$$

It is apparent here that the position of the Moire pattern fringes Δy, or the phase term where the phase, defined as phase = $2\pi\ \Delta y / p_{moire}$, yields the out of plane information. The out of plane displacement is dependent on the pitch of the two original gratings, the magnification from the surface to the second grating, the angular misalignment between the two gratings, and the system viewing angle.

It is possible to determine the spacing and phase of the Moire pattern by: 1) setting the arguments of the two gratings equal to increments of 2π (as done previously) and 2) subtracting the resulting two equations. The result is an equation like that of (2.1.14) that only describes the spacing and phase of the Moire pattern. This method is used to describe the Moire pattern of two Ronchi type gratings in the next section.

2.1.2 The Moire Pattern of Two Ronchi Gratings

The theory described previously applies in the case of Ronchi type gratings. Let the transmission of a Ronchi type grating (bar and space) be described by the convolution of the rect function with a series of delta functions arranged periodically as in the expression

$$\text{rect}\left[\frac{x}{p}\right] * \sum_{n=0}^{N} \delta(x-np)$$

$$\text{where} \quad \text{rect}\left[\frac{x}{p}\right] = \begin{cases} 1 & \text{for } -\frac{p}{2} \le x \le \frac{p}{2} \\ 0 & \text{elsewhere} \end{cases} \qquad (2.1.17)$$

$$\text{and} \quad \delta(x-np) = \begin{cases} 1 & \text{when } x = np \quad \text{for} \quad n = 0, 1, 2, 3, \ldots \\ 0 & \text{elsewhere} \end{cases}$$

as in Figure 2.6. By examining Figure 2.6 it is apparent that the transmission function of (2.1.17) can be written in terms of pitch and phase. An expression denoting only the center position of each space in the grating along x is written as x=np, where n = 0, 1, 2, 3, ...In

this form G_A can be written,

$$x = n_A p_o \tag{2.1.18}$$

where $n_A = 0,1,2,3...$ If the grating G_A is shifted about the +z axis by $\theta/2$, projected onto surface Σ, and viewed at an angle ϕ oblique to the -z axis as in the previous section, the image at G_B is

$$x \cos\phi \cos\frac{\theta}{2} - y \sin\frac{\theta}{2} - z_o M_B \sin\phi = n_A p_o M_A M_B \ . \tag{2.1.19}$$

G_B is again shifted around the +z axis by an angle $-\theta/2$ and represented as

$$x \cos\frac{\theta}{2} + y \sin\frac{\theta}{2} = n_B p_B \ , \tag{2.1.20}$$

where $n_B = 0, 1, 2, 3,...$ Again making the substitution for p_A where

$$p_A = \frac{p_o M_A M_B}{\cos\phi} \ , \tag{2.1.21}$$

the Moire fringe pattern is found by taking the difference between (2.1.19) and (2.1.20) and is

$$x\left[\frac{1}{p_A} - \frac{1}{p_B}\right]\cos\frac{\theta}{2} - y\left[\frac{1}{p_A\cos\phi} + \frac{1}{p_B}\right]\sin\frac{\theta}{2} - \frac{z_o M_B \tan\phi}{p_A} = l_m \ . \tag{2.1.22}$$

When $p_A = p_B$, (2.1.22) is simplified to the form similar to the argument of term two in (2.1.14) in which the variation in x is zero. Therefore, solving for y will yield the information about the pitch and phase of the Moire fringe pattern where

$$y = \frac{l_m p_A \cos\phi}{\left[1 + \cos\phi\right]\sin\frac{\theta}{2}} - \frac{z_o M_B \sin\phi}{\left[1 + \cos\phi\right]\sin\frac{\theta}{2}} \tag{2.1.23}$$

which has the form $y = l_m\, p_{moire} + \Delta y$ and where $l_m = n_A - n_B = 0, 1, 2,...$ Note that

(2.1.23) is identical to (2.1.15).

As previously determined the phase shift of the Moire pattern (phase of (2.1.22)) yields the out of plane displacement information, z_0. Therefore, by monitoring the phase of the Moire intensity fringe pattern the out of plane displacement of surface Σ can be determined. The effects of these parameters as well as the grating pitch on the Moire pattern will be discussed in the next section.

2.2 Analysis of the Moire Pattern Parameters

For a fixed viewing angle the Moire fringe intensity pattern can be altered by adjusting the pitch of either or both gratings or the angular misalignment θ, between the two gratings. The effects of varying pitch, misalignment angle, and viewing angle will now be explored.

2.2.1 The Effects of Varying Pitch

From equation (2.2.14) it follows that for p_A not equal to p_B, and $\theta = 0$, that

$$x\left(\frac{1}{p_A} - \frac{1}{p_B}\right) - \frac{z_o M_B \tan\phi}{p_A} = l_m \ , \qquad (2.2.1)$$

where $l_m = 0, 1, 2, 3, ...$Note that in this case the fringes are a function of x only with period or pitch, $(p_A p_B) / (p_B - p_A)$. Rearranging (2.2.1) the relationship between x and z_0 is

$$x = l_m\left(\frac{p_A p_B}{p_B - p_A}\right) + z_o M_B \tan\phi\left(\frac{p_B}{p_B - p_A}\right) . \qquad (2.2.2)$$

As the relative difference in grating pitch increases the pitch of the Moire pattern decreases.

In Figure 2.7a the grating pitches of G_A and G_B are approximately 0.6 mm and 1.23 mm respectively. The difference in pitch is roughly 0.63 mm producing a Moire pattern with a 1.2 mm pitch. In Figure 2.7b the pitch of G_A is changed to 1.5 mm resulting in a pitch difference of .25 mm and a Moire pitch of 7.0 mm. The pitch difference in Figure 2.7b was smaller than the pitch difference in Figure 2.7a and hence there was a larger Moire pitch in Figure 2.7b.

There are two effects that influence the contrast or visibility of the Moire fringes: 1) the pitch difference between the two gratings, and 2) the ratio of bar to space width in the case of Ronchi-type gratings.

If the out of plane displacement z_o, and the angular misalignment θ, are set to zero, then from (2.1.12), the resulting intensity pattern is

$$I_{total} \propto \frac{1}{4} + \frac{1}{4}\cos\left(\frac{2\pi x}{p_A}\right) + \frac{1}{4}\cos\left(\frac{2\pi x}{p_B}\right) + \frac{1}{4}\cos\left(2\pi x\left\{\frac{1}{p_A}+\frac{1}{p_B}\right\}\right) + \frac{1}{4}\cos\left(2\pi x\left\{\frac{1}{p_A}-\frac{1}{p_B}\right\}\right) . \quad (2.2.3)$$

If $p_A = 2p_B$ (2.2.3) becomes

$$I_{total} \propto \frac{1}{4} + \frac{1}{4}\cos\left(\frac{\pi x}{p_B}\right) + \frac{1}{4}\cos\left(\frac{2\pi x}{p_B}\right) + \frac{1}{4}\cos\left(\frac{3\pi x}{p_B}\right) + \frac{1}{4}\cos\left(\frac{\pi x}{p_B}\right) . \quad (2.2.4)$$

The Moire term (last term of (2.2.4) and (2.2.3)) now has the same spatial frequency as the first term or sum term in (2.2.4). Thus, $p_A = p_B$, it is impossible to separate the Moire pattern from the pattern of the first or second gratings. To separate the Moire pattern from other patterns within the image, the difference between p_A and p_B must be small enough so that the frequency of the Moire pattern does not approach the frequency of either of the two gratings, or

$$p_A - p_B \ll p_A \text{ or } p_B . \quad (2.2.5)$$

Another effect that influences the visibility of the Moire fringes is the ratio of bar width

to space width of Ronchi gratings. Using the parameters defined by Post in reference [18], R = bar width / space width of a Ronchi grating (Figure 2.8a,b) and the transmittance of a Ronchi grating is defined as T = 1 / (R+1). For optimum fringe sharpness, if R = a for grating one, then R = 1/a for grating two or vice versa. In other words, if grating one had a transmittance represented by Figure 2.8a and grating two had a transmittance represented in Figure 2.8b, the result would be a sharper Moire fringe. According to Post the width of the bright fringe H, (Figure 2.9) can be predicted by the transmittance of the grating with the larger R (Figure 2.8a) such that

$$\frac{W}{H} = T = \frac{1}{1+R} = \frac{\text{space width}}{\text{bar width + space width}}\ , \qquad (2.2.6)$$

where W is the width of a dark fringe. It is also possible to achieve sharper fringes with two gratings that both have R greater than one but the overall intensity of the pattern is reduced. Figure 2.10a illustrates the sharper fringes using a grating of R greater than one together with a grating of R less than one. In Figure 2.10b the Moire fringes are not as well defined since both gratings have the same R less than one.

2.2.2 The Effects of Varying Grating Alignment Angle

The pitch of the Moire pattern (2.1.15) shows an inverse dependence on $\sin(\theta/2)$. Figure 2.11 is a plot of $1/\sin(\theta)$ showing the multiplication factor of the Moire pitch for increasing angle θ. To further illustrate the point, Figure 2.12a shows the Moire pattern of two amplitude sinusoidal gratings with the same pitch but with an angular misalignment of four degrees. There are twice as many fringes in the Moire pattern of the same two gratings with an angular misalignment of eight degrees as seen in Figure 2.12b. To demonstrate the effect with two Ronchi gratings, Figure 2.13a shows two gratings

misaligned by angle θ and Figure 2.13b shows two gratings misaligned by an angle larger than the θ in Figure 2.13a. It is apparent here that increasing the angle θ increases the total number of fringes in the Moire pattern.

2.2.3 The Effects of Varying Viewing Angle

Another parameter to consider is the viewing angle of the Moire projection system. By altering the viewing angle, the pitch of G_A at G_B is changed and therefore, so is the pitch of the Moire pattern. In equation (2.2.1) the sensitivity of z_0 is determined by the pitch of the gratings used to form the Moire pattern, the magnification required to image G_A on to G_B such that the grating pitches are nearly the same, and by the tangent of the viewing angle ϕ. Solving for the sensitivity S described by the phase shift (of single degree) per out of plane displacement z_0,

$$S = \frac{\text{phase}}{z_o} = \frac{M_B \tan\phi}{p_A} \quad . \tag{2.2.7}$$

Figure 2.14 is a graph of $\tan\phi$ and illustrates that as the viewing angle is increased the sensitivity of the phase per out of plane displacement z_0 is increased as well.

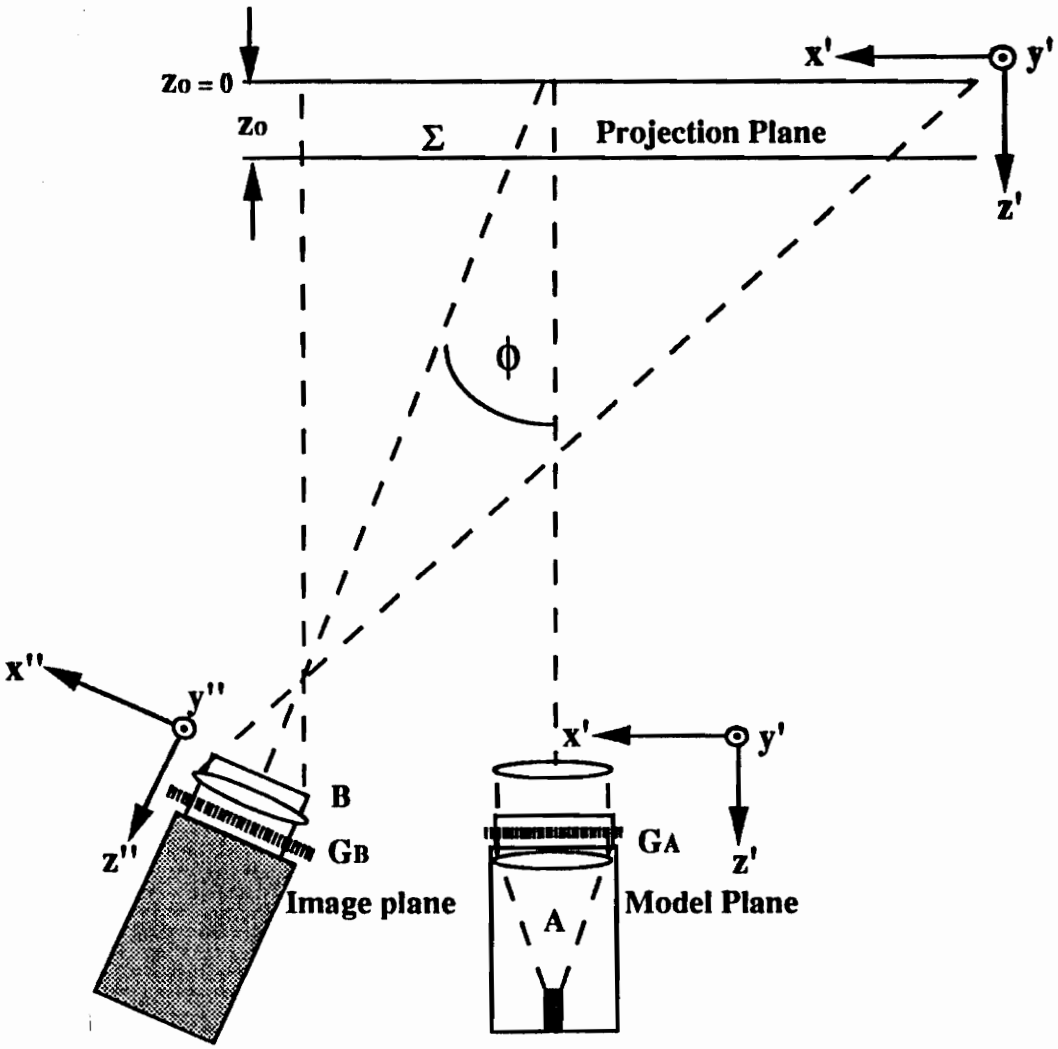

Schematic for Projection Moire

Figure 2.1

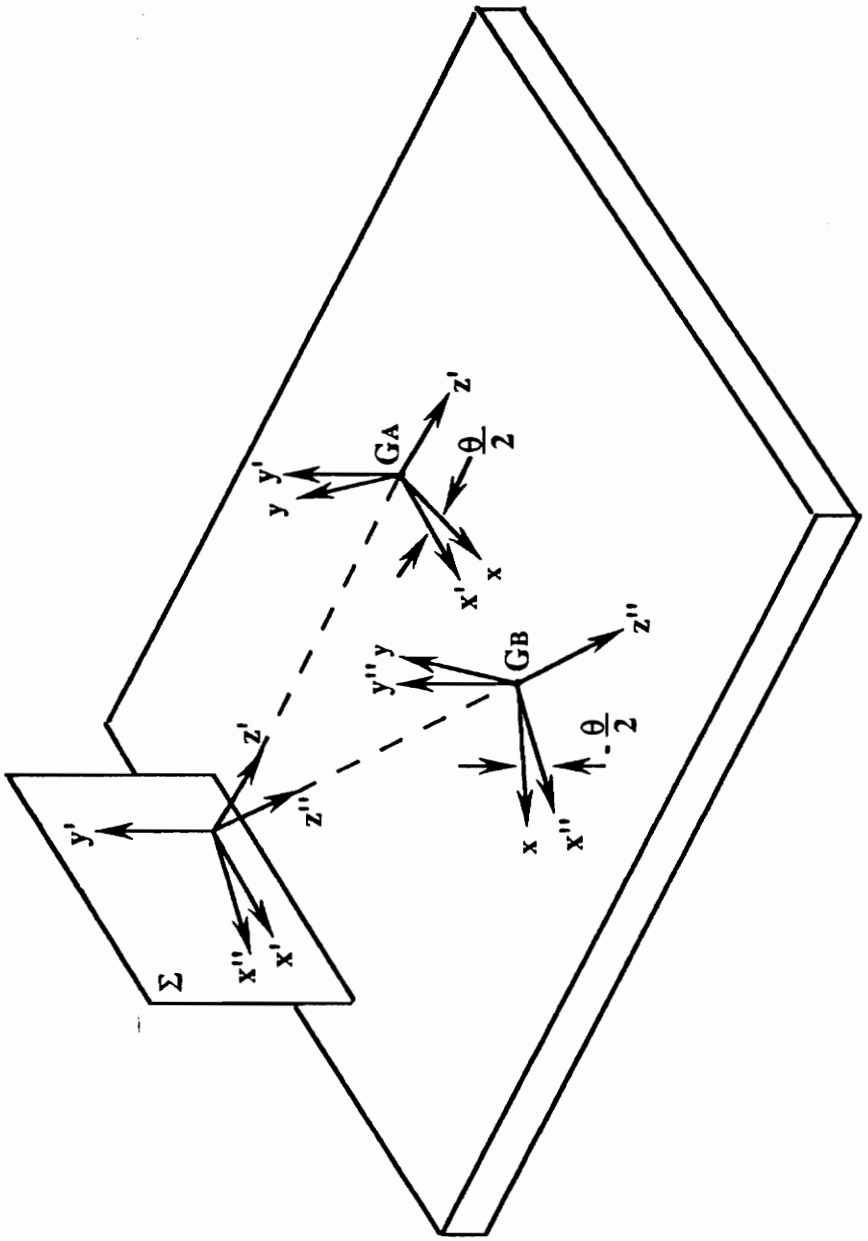

Coordinate System Labels

Figure 2.2

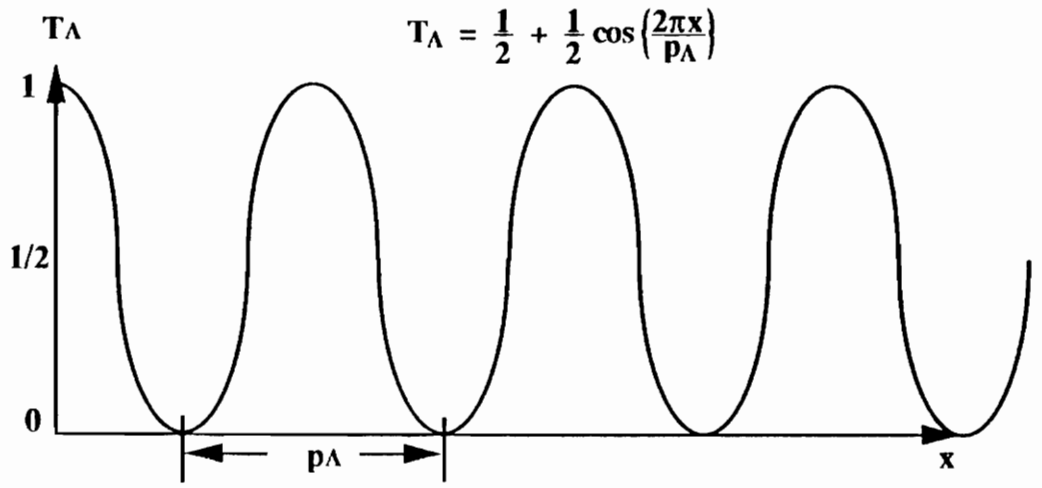

Transmittance of Sinusoidal Amplitude Grating

Figure 2.3

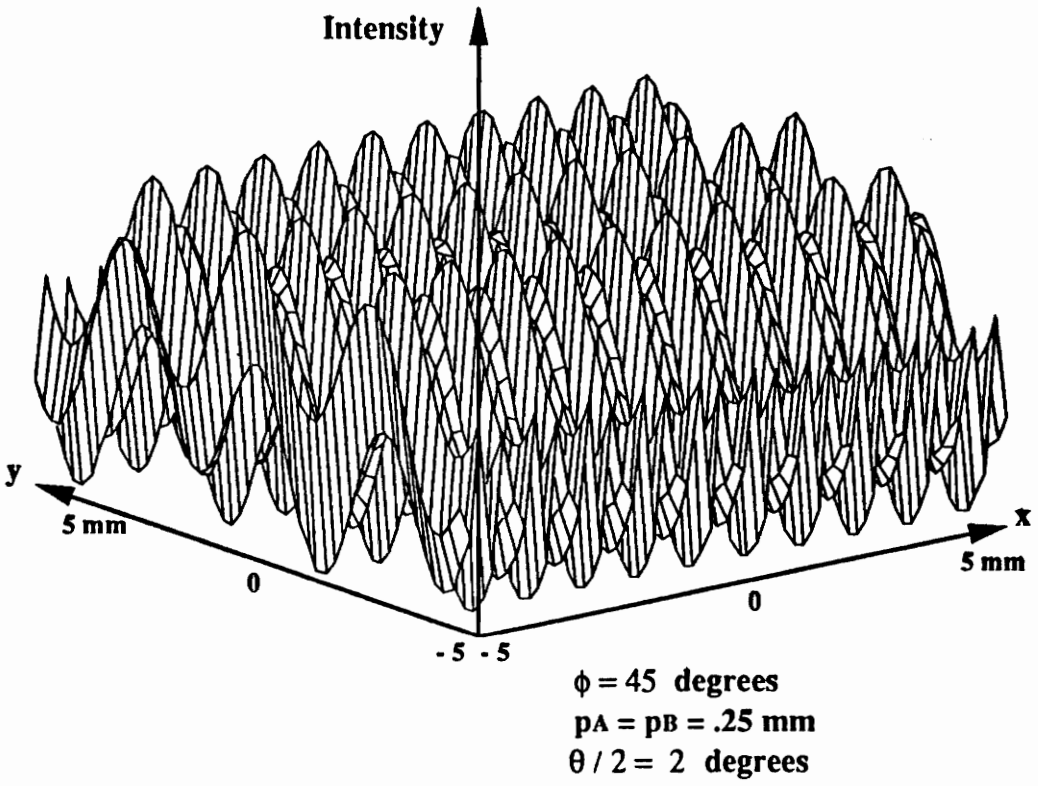

Plot of Equation (2.2.13)

Figure 2.4a

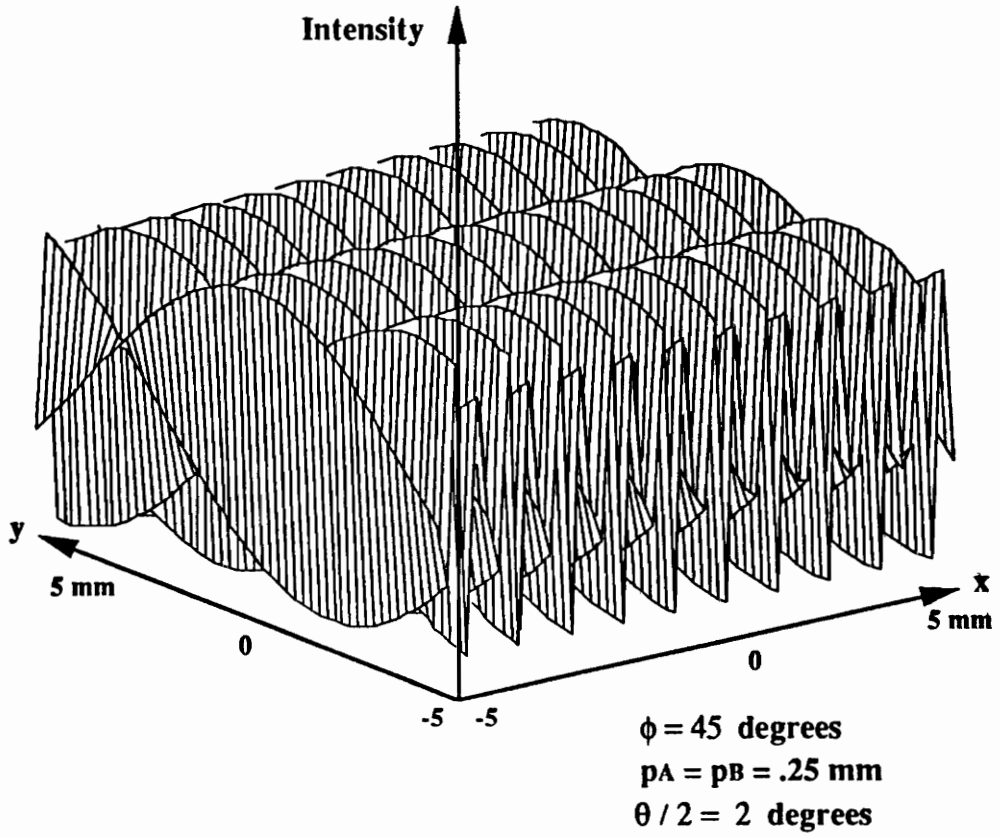

Plot of First Term of (2.2.13)

Figure 2.4b

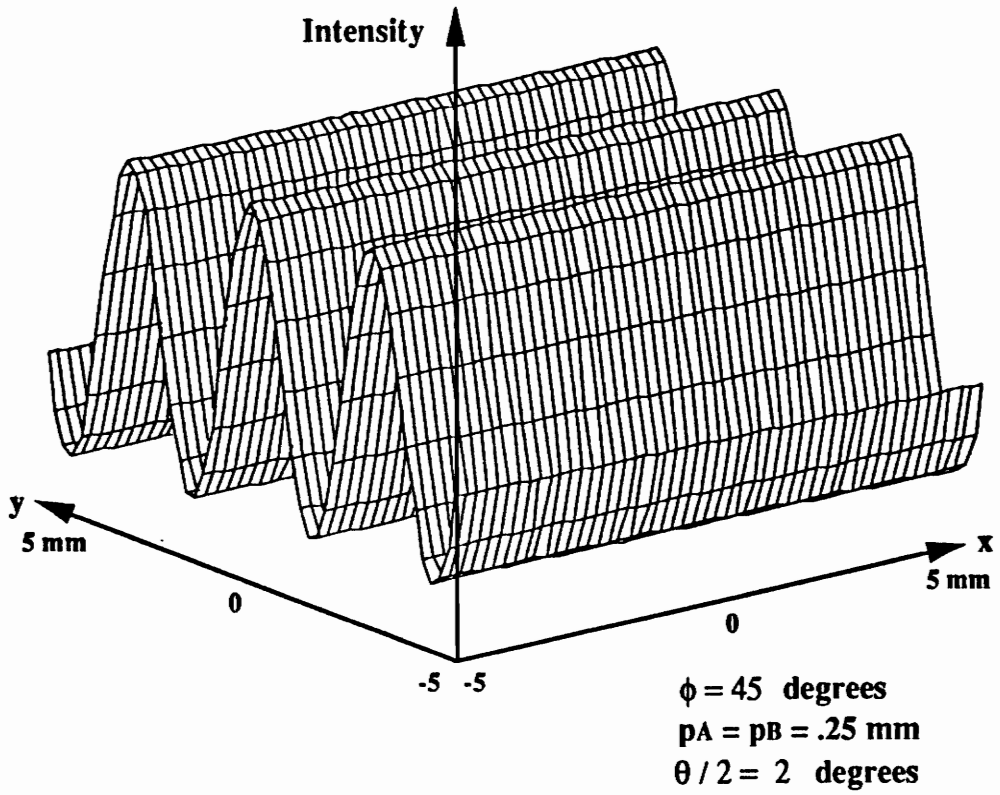

Plot of Second Term of (2.2.13)

Figure 2.4c

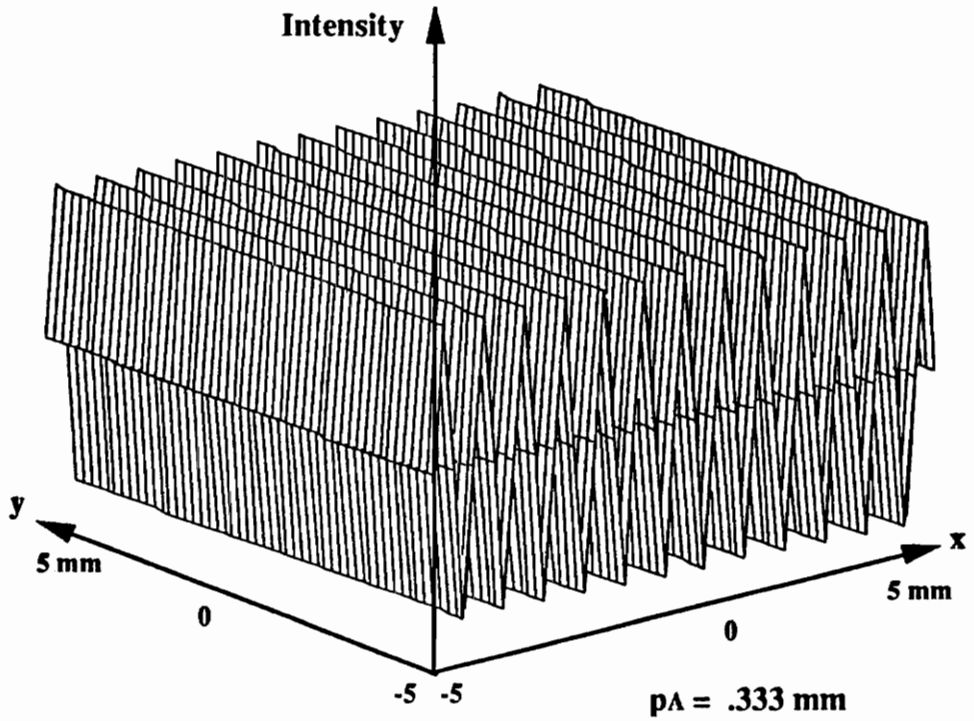

Pitch Mismatch Only

$p_A = .333$ mm
$p_B = .308$ mm
$\phi = 45$ degrees
$\theta / 2 = 0$ degrees
$z_o = 0$

Plot of First Term of (2.1.12)

Figure 2.5a

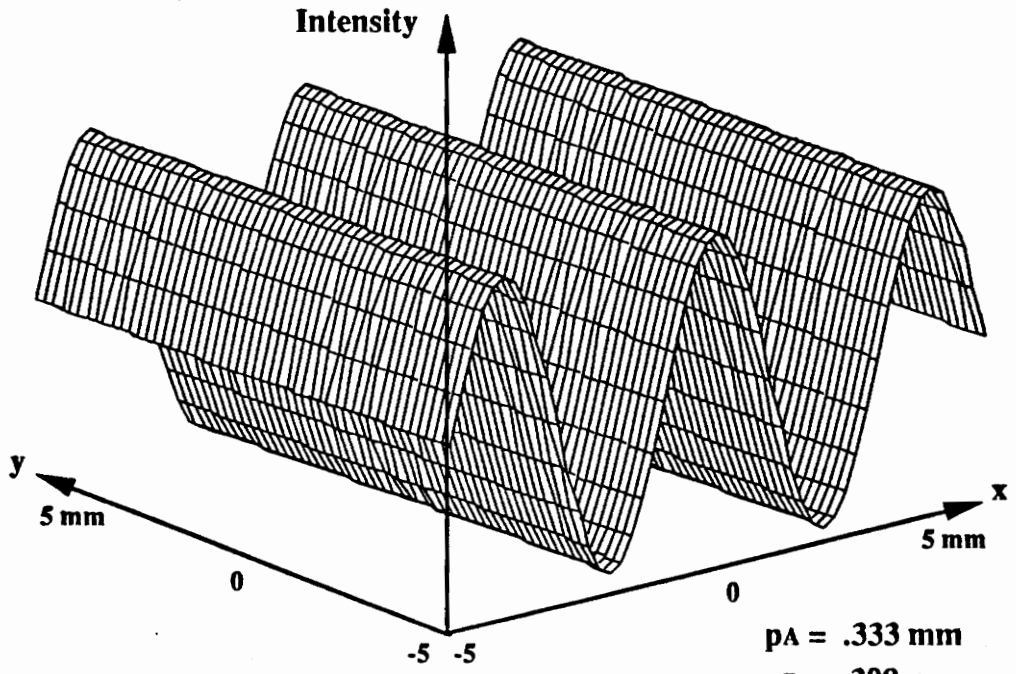

Plot of Second Term of (2.1.12)

Figure 2.5b

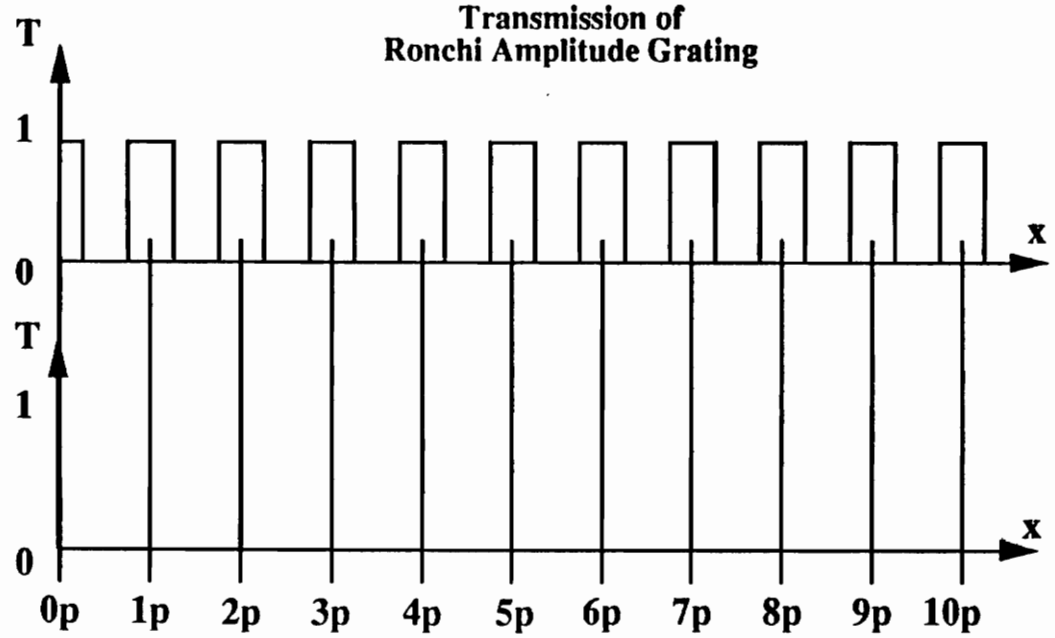
Transmission of
Ronchi Amplitude Grating
T
1
0
x
T
1
0
x
0p
1p
2p
3p
4p
5p
6p
7p
8p
9p
10p

Figure 2.6

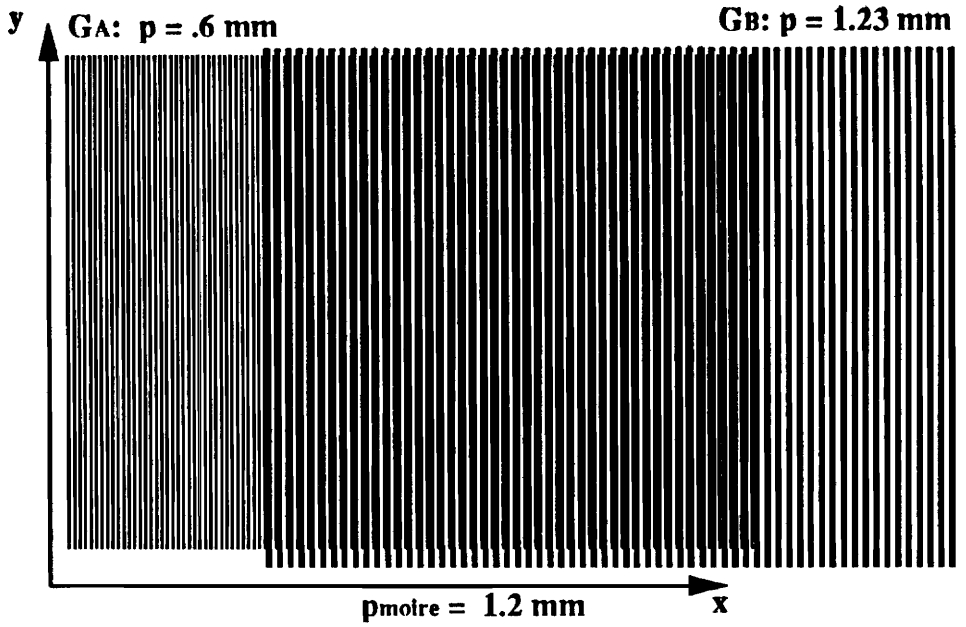

Moire Pattern Caused by Pitch Mismatch

Figure 2.7a

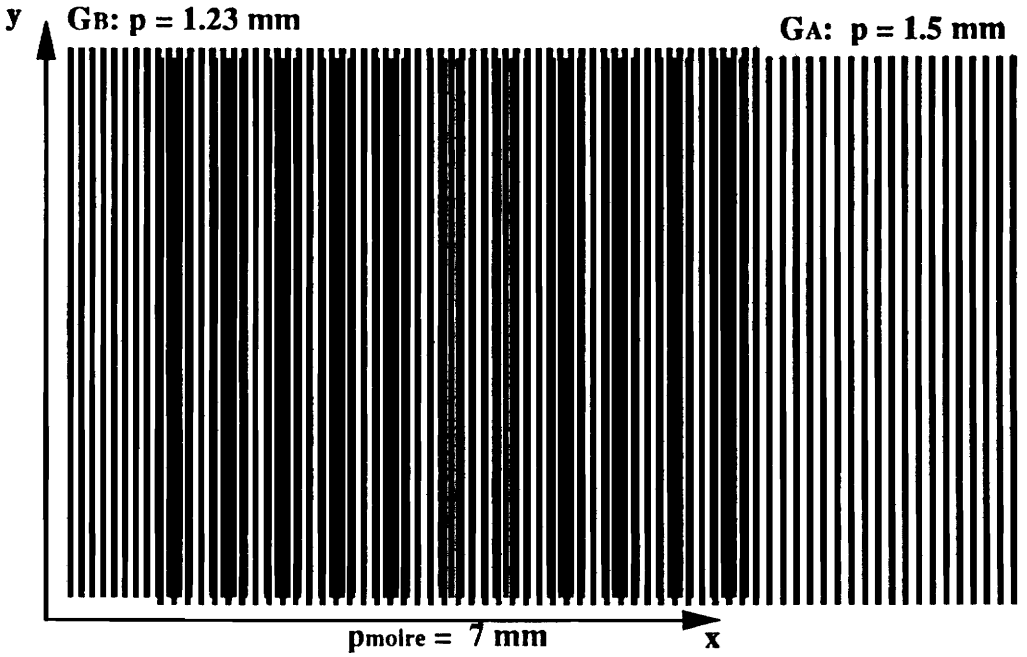

Moire Pattern Caused by Pitch Mismatch

Figure 2.7b

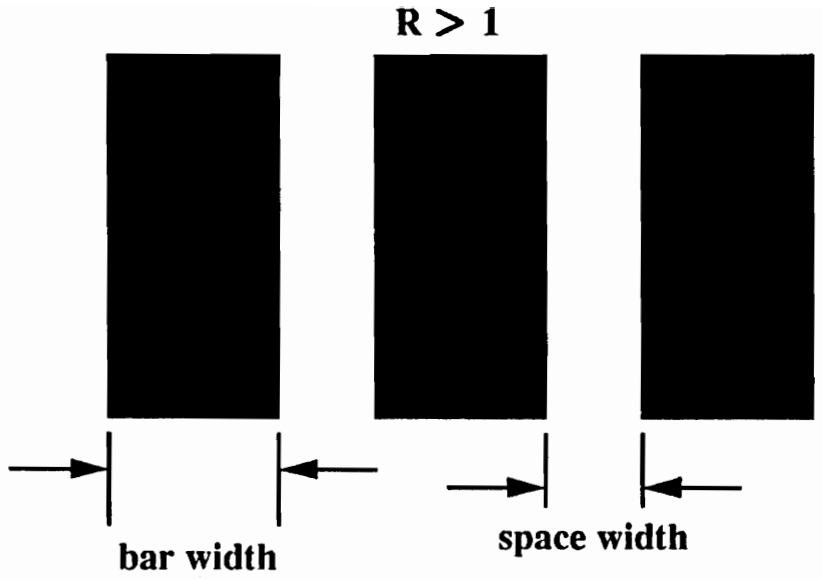

Bar and Space Width of a Ronchi Grating

Figure 2.8a

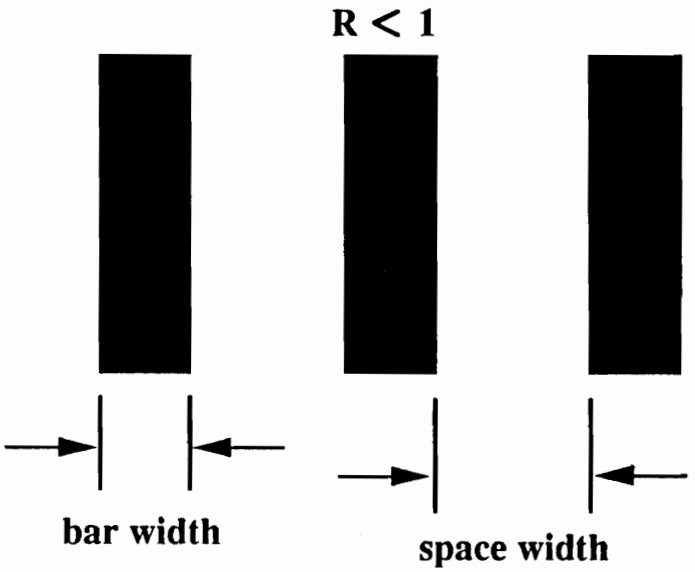

Bar and Space Width of a Ronchi Grating

Figure 2.8b

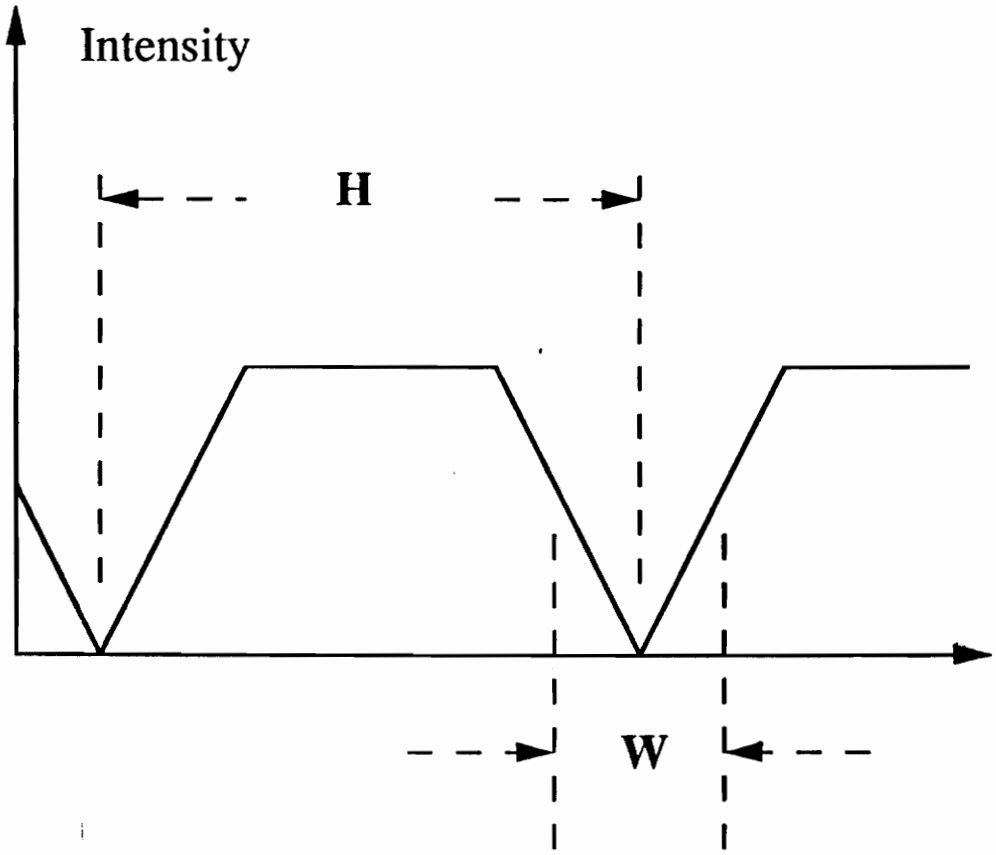

Intensity Profile of Moire Fringes

Figure 2.9

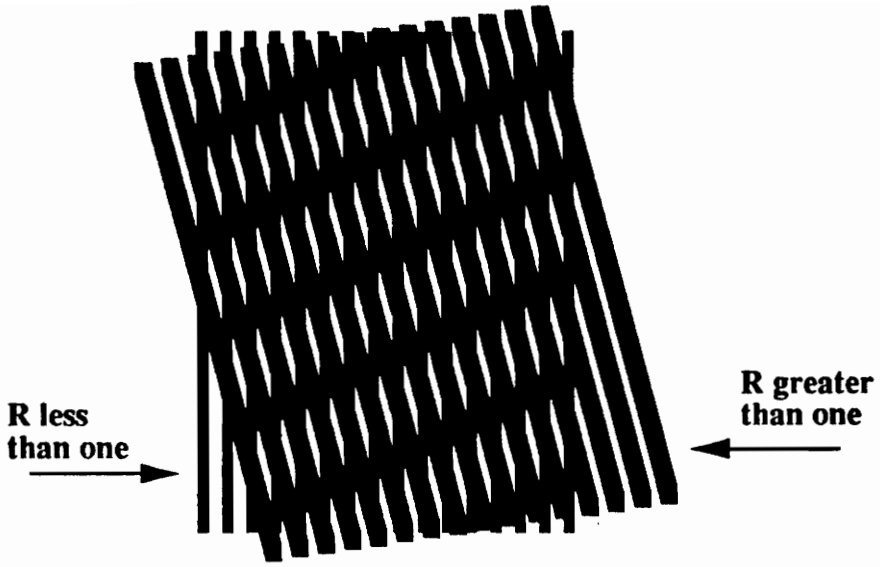

Fringe Contrast of Two Gratings:
R greater than one
R less than one

Figure 2.10a

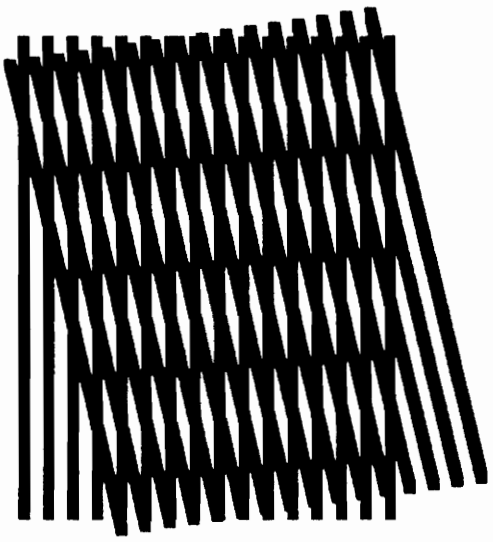

Fringe Contrast of Two Gratings:
Equal R less than one

Figure 2.10b

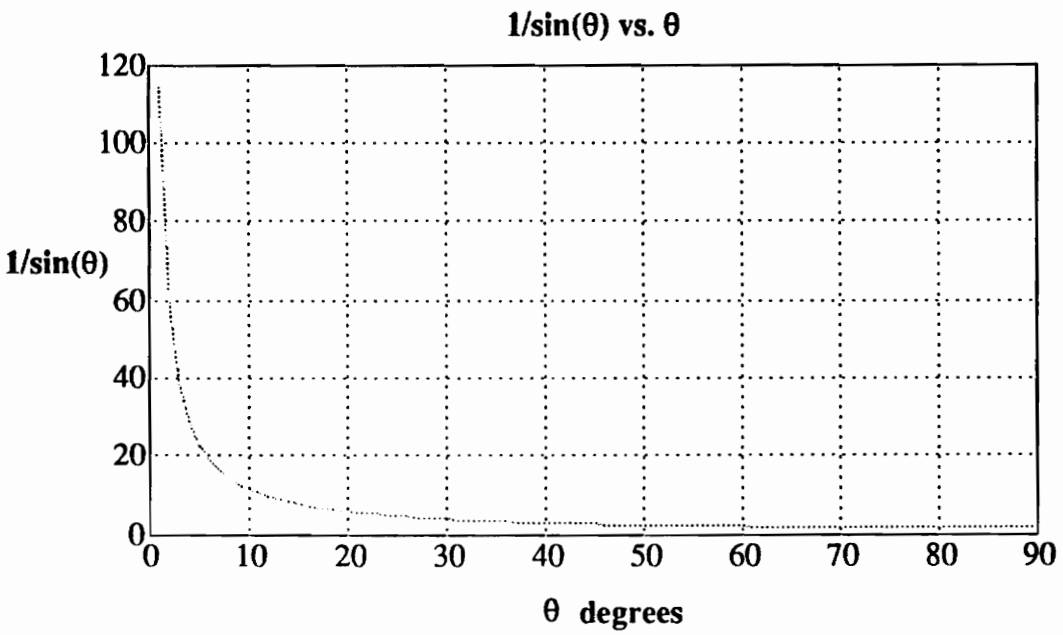

Moire Pitch Dependence on Angular Misalignment θ

Figure 2.11

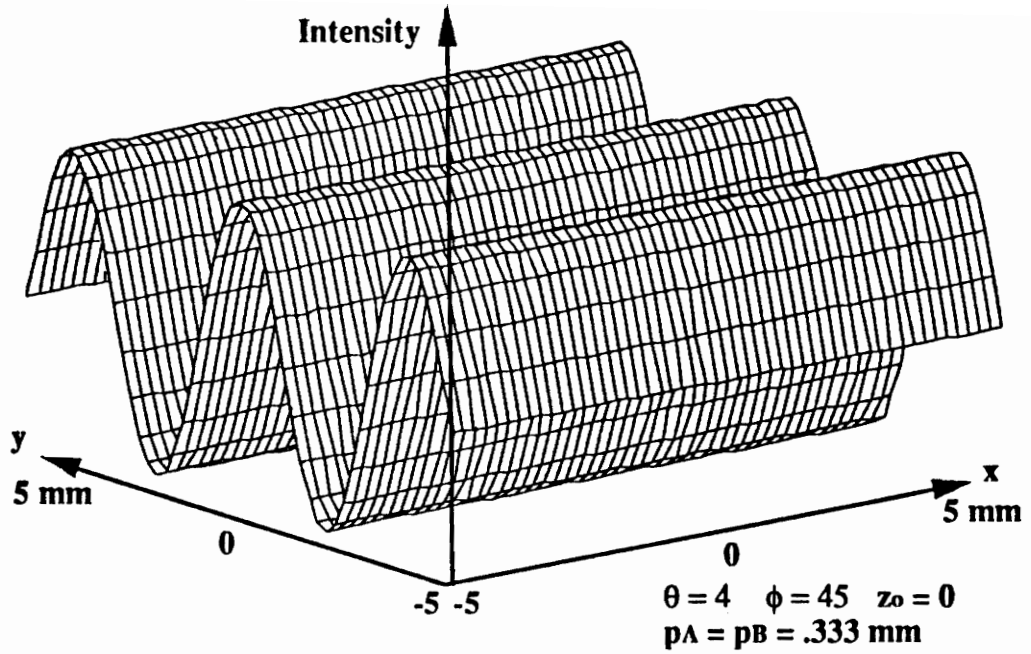

Moire Pattern Caused by Angular Misaglignment

Figure 2.12a

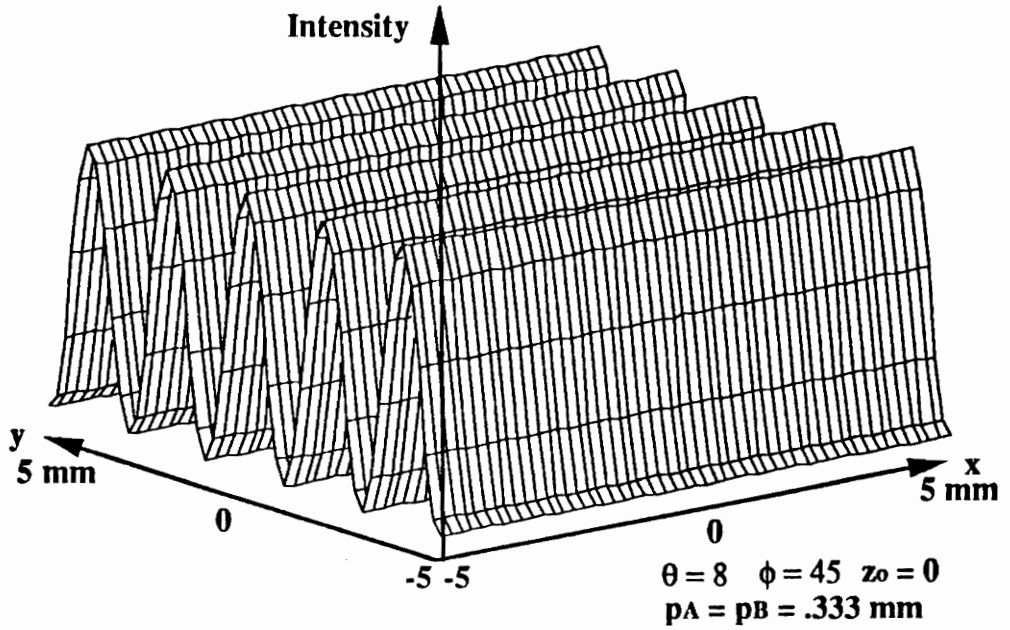

Moire Pattern Caused by Angular Misaglignment

Figure 2.12b

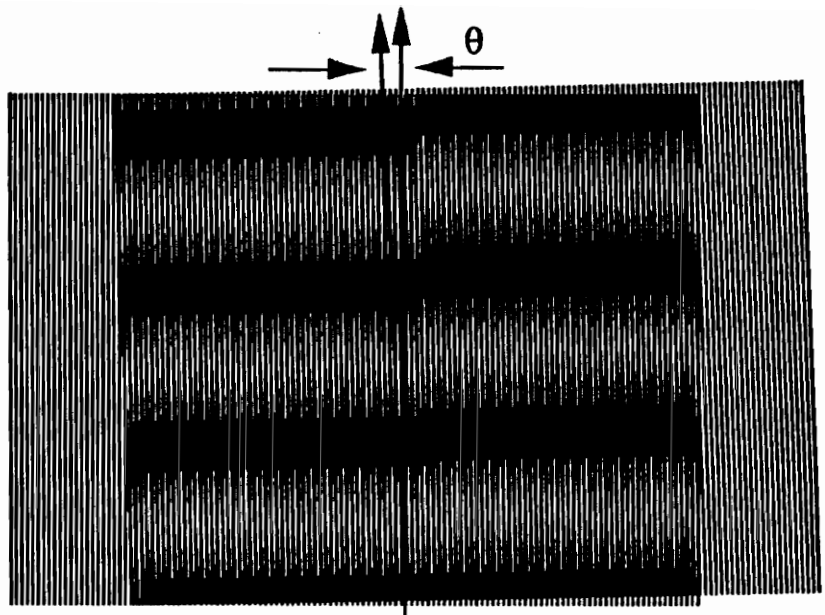

Moire Pattern Caused by Angular Misalignment of Ronchi Gratings

Figure 2.13a

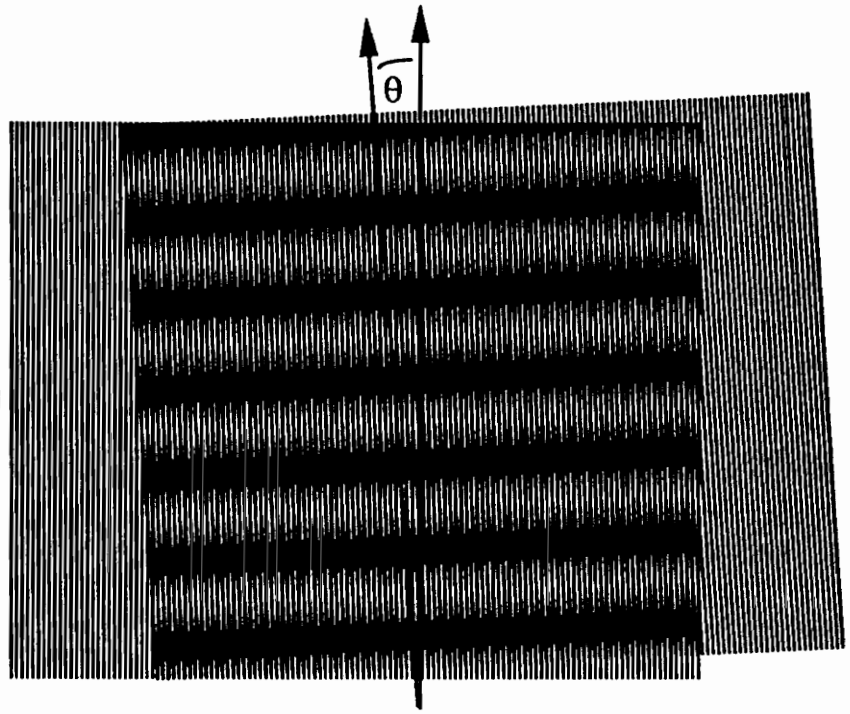

Moire Pattern Caused by Angular Misalignment of Ronchi Gratings

Figure 2.13b

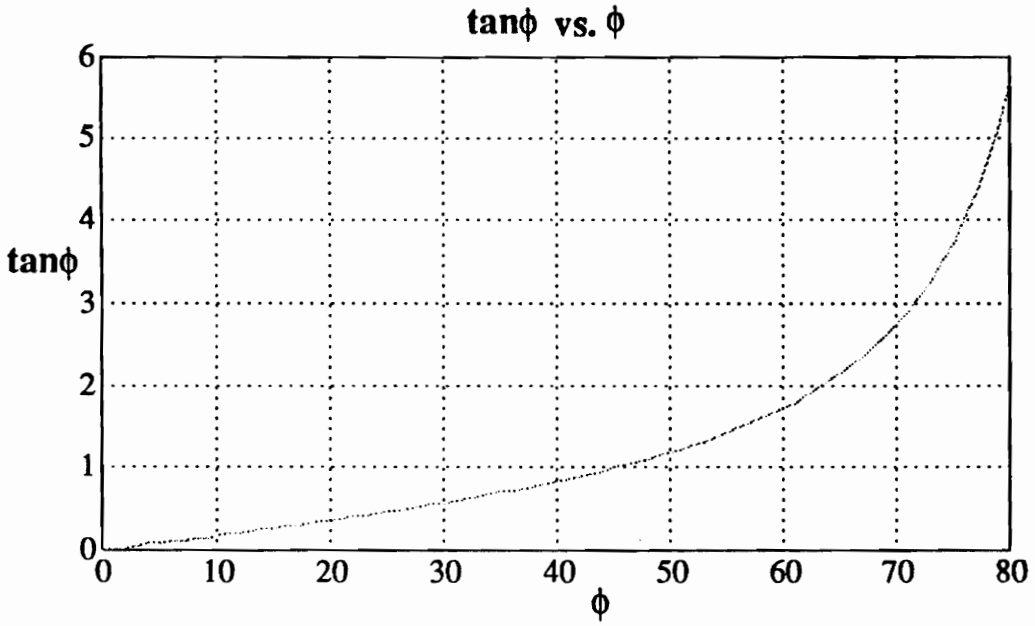

Sensitivity as a Result of Viewing Angle Variation

Figure 2.14

3.0 Interpretation of Moire Fringes

The goal is to determine the out-of-plane displacement of a surface Σ by monitoring the phase shift of the incoherent Moire fringe pattern. First, two approaches for determining the phase of the Moire pattern are described; 1) filtering and interpolating the intensity pattern and comparing the smoothed pattern against a reference sinusoid, and; 2) scanning the projected fringes across the surface Σ and determining the phase of the moving Moire pattern at each point in the image by comparing the phase of the output of a photodetector positioned at a point to a signal of the same frequency. Second, a method is described for processing the Moire fringe pattern to increase the resolution using coherent optical processing.

3.1 Intensity-Based Phase Detection

In general, it is difficult to measure the phase shift of the Moire pattern by measuring the intensity. The signal to noise ratio is often low and the intensity of the fringe pattern is affected by the nonuniformity of source illumination as well as surface reflectivity. In addition, the high frequency carrier patterns can hinder fringe visibility. Finally, to make the phase shift measurement the fringes must be identified by order number and tracked. This can be cumbersome. For these reasons, quantitative data is difficult to obtain.

A simple algorithm has been developed and implemented on a personal computer for filtering a digitized Moire pattern and matching the filtered pattern to a reference sinusoid. The digitized Moire pattern is post processed and user interaction is required to identify the fringes. Once the Moire fringes are identified by number, four fringes from the center of

the pattern are compared to a sinusoidal pattern. The sinusoidal pattern is matched in spatial frequency and adjusted in phase to match the Moire fringes. The phase is recorded as the average phase of the Moire pattern.

3.2 Frequency-Based Phase Detection

Many of the problems of an intensity-based phase measurement can be reduced or alleviated by making a frequency-based measurement. To make a measurement based on frequency it is necessary to scan the projected grid pattern or fringes over the surface. The intensity of the moving Moire pattern is detected at each point in the image using either an array of photodetectors or a single photodetector which, following a phase measurement, is stepped to a new position in the pattern [20]. Each photodetector is smaller in diameter than a fringe and as a result, the output of a photodetector as a function of time is sinusoidal. Using a phase meter or lock-in amplifier, the phase at each point in the Moire pattern is determined by comparing the output of each photodetector (or the output of a single photodetector at each position) to a reference signal of the same frequency.

The stability and sensitivity of a frequency-based phase measurement depends not only on the type of instrument used to measure the phase, but also on the technique used to scan the projected fringes. Following a brief discussion of the theory of electronic, or frequency-based phase detection, two techniques which have been used to scan projected fringes are described and compared. These techniques are: 1) using an acousto-optic modulator, and; 2) moving one arm of a Michelson interferometer with a piezoelectric translator. Descriptions of other techniques including mechanically moving a grating are found in reference [20].

3.2.1 Theory of Electronic Phase Detection

If a grating G_A is shifted in time at a constant velocity v, then, similar to the expression derived for the transmittance of a stationary grating (2.2.1), the expression for the transmittance of the moving grating is

$$\frac{1}{2} + \frac{1}{2}\cos\left(\frac{2\pi x}{p_o} - \frac{2\pi vt}{p_o}\right). \tag{3.2.1}$$

The image intensity of G_A at G_B is then

$$\frac{1}{2} + \frac{1}{2}\cos\left(\frac{2\pi x\cos\phi}{M_A M_B p_o} - \frac{2\pi z_o \sin\phi}{M_A M_B p_o} - \frac{2\pi vt\cos\phi}{M_A M_B p_o}\right), \tag{3.2.2}$$

The transmittance of G_B is

$$\frac{1}{2} + \frac{1}{2}\cos\left(\frac{2\pi x}{p_B}\right), \tag{3.2.3}$$

and if

$$p_A = \frac{p_o M_A M_B}{\cos\phi} \tag{3.2.4}$$

the Moire pattern of (3.2.2) and (3.2.3) is

$$I_{total} \propto \frac{1}{2} + \frac{1}{2}\cos\left(2\pi x\left\{\frac{1}{p_A} - \frac{1}{p_B}\right\} - \frac{2\pi}{p_A} z_o\tan\phi - \frac{2\pi}{p_A} vt\right). \tag{3.2.5}$$

Setting $p_A = p_B$ in (3.2.5),

$$I_{total} \propto \frac{1}{2} + \frac{1}{2}\cos\left(\omega t + \frac{2\pi}{p_A} z_o\tan\phi\right). \tag{3.2.6}$$

From (3.2.6) it can be seen that the Moire pattern is a traveling wave of frequency $\omega = 2\pi v/p_A$ and phase = $(2\pi\ z_o\tan\phi) / p_A$. This phase information can be extracted using a phase meter which compares the signal to a reference signal of frequency $\omega/2\pi$. Because the phase is determined by comparing the frequency of two signals, the measurement is not

as sensitive as an intensity based measurement. Analysis of the sensitivity of a representative phase detector, a lock-in amplifier, to the ratio of the input signal-to-noise is included in chapter four.

3.2.2 Methods for Generating Moving Fringes

Two techniques for generating moving fringes are now described. These techniques have been tested experimentally. The first technique described uses an acousto-optic modulator. The second technique uses a piezoelectric actuator to translate one arm of a Michelson interferometer.

An acousto-optic cell of window size D (figure 3.1), will transmit sound at a velocity V_S in T_S seconds. This cell when driven by a modulation frequency of F_{mod} will generate a grating of period p where

$$p_{AO} = \frac{V_s}{F_{mod}} \ . \tag{3.2.7}$$

The number of fringes over the window is

$$\#\ \text{fringes/window} = \frac{D}{p_{AO}} \ . \tag{3.2.8}$$

Therefore, the period and fringe density are based on the modulation frequency signal to the acousto-optic modulator. Equation (3.2.7) shows that the higher the modulation frequency, the smaller the grating period. The modulation frequency is also the frequency that the fringes move across the window in time. For example, if the velocity of sound in a typical acousto-optic modulator is .617 mm/μs and the window diameter is 25.4 mm, at a modulation frequency of 200 KHz, the pitch of the grating will be approximately 3 mm. With this pitch there will be eight fringes in the cell window.

A moving grating can also be generated using a Michelson interferometer with one moving mirror. The fringes of a Michelson interferometer are formed by the interference pattern of two beams with a slight optical path length difference (figure 3.2). Light travels through a beamsplitter and divides into two separate beams. Each beam encounters a mirror and is reflected back from where it came. The two beams enter the beamsplitter and reunite to form a fringe intensity pattern on the projection surface. From figure 3.2, the distance from the beam-splitter to the stationary mirror is d_1. The stationary mirror is assumed to be in the x-y plane normal to the optical axis z. The distance from the beamsplitter to the moving mirror at an instant in time is d_2. The intensity pattern of the two interfering beams yields a fringe pattern based on the difference $d = d_2 - d_1$ and the mirror alignment angle to the x-y plane (figure 3.3a) The optical path length difference determines the spacing and orientation of the fringe pattern,

$$I \propto \cos\left(\frac{2\pi}{\lambda}\text{path length difference}\right) \qquad (3.2.9)$$

where λ is the wavelength of the source illumination. The path length difference between the two mirrors is set to zero at one end along the x axis, as shown in Figure 3.3a. One mirror is rotated by φ around the y axis and γ around the x axis (not pictured in figure 3.3a). The other mirror is perpendicular to the optical axis z. The path difference between the mirrors is 2d where d is found in terms of the x and y coordinates of mirror one by using the rotation matrix (Appendix A, (A.6)). The distance d is multiplied by a factor 2 since each beam travels to a mirror and back again. The expression for the physical path difference is

$$2d = -2x \cos\gamma \sin\varphi + 2y \sin\gamma \ . \qquad (3.2.10)$$

Therefore, the intensity fringe pattern is

$$I \propto \cos\left(\frac{2\pi}{\lambda}\{-2x\cos\gamma\sin\varphi + 2y\sin\gamma\}\right) . \qquad (3.2.11)$$

In order to generate straight line fringes along the x direction, γ must be set to zero (as in figure 3.3a) so that with $\varphi = \sigma$, (3.2.11) can be simplified to

$$I \propto \cos\left(\frac{2\pi}{\lambda} 2x\sin\sigma\right) . \qquad (3.2.12)$$

The pitch of this fringe pattern is $\lambda / 2\sin\sigma$ and can be adjusted by changing the angle σ. If mirror one is shifted by a very small distance along the z axis as in figure 3.3b, the expression for intensity is

$$I \propto \cos\left(\frac{2\pi}{\lambda} 2x\sin\sigma + \frac{2\pi}{\lambda} 2d\right) . \qquad (3.2.13)$$

The expression in (3.2.13) is a fringe pattern along x. The phase shift with respect to x is dependent on d. If this distance d were to change in time by v in units of distance per second (3.2.13) becomes

$$I \propto \cos\left(\frac{2\pi}{\lambda} 2x\sin\sigma + \frac{2\pi}{\lambda} 2vt\right) . \qquad (3.2.14)$$

The expression in (3.2.14) is a moving grating of temporal frequency $2v/\lambda$ Hz and of spatial frequency $2\sin\phi/\lambda$ fringes per meter. Therefore, changing the velocity of the moving mirror alters the temporal frequency and changing the angular alignment alters the spatial frequency of the fringes.

3.3 Coherent Optical Processing of Moire Fringes

The Moire fringes from the projection Moire system are incoherent but can be transduced to coherent fringes by a spatial light modulator (SLM) (figure 3.4). The incoherent fringes are recorded and the information is sent to an SLM which acts as a mask for a coherent source. The output of the transducing system is a coherent Moire pattern that contains the same information as the original incoherent Moire pattern. Once in a coherent form, the pattern can then be optically filtered to increase visibility and the fringes can be interpolated. The coherent interpolation method discussed in this section is known as fringe multiplication.

3.3.1 Fringe Multiplication

Fringe multiplication occurs when light is doubly diffracted by two gratings which are superimposed and illuminated by a coherent source [18-19]. Light emerging from the first grating is diffracted into orders. The orders enter the second grating and are diffracted again as seen in figure 3.5. It is easier to understand and implement fringe multiplication if, instead of passing all of the diffracted orders from the first grating, all but two of the orders are filtered out. The technique of passing only selected orders in fringe multiplication was first described by Sciammarella in reference [17]. A schematic diagram illustrating an experiment setup for filtering only two orders is shown in figure 3.6. A derivation of the predicted intensity along the x axis at the output of the setup shown in figure 3.6 follows.

The transmittance of a Ronchi grating (figure 3.7) is a periodic function and therefore can be represented by a Fourier series. A Fourier series representation of a periodic

function f(x) with period p is

$$f(x) = \sum_{m=0}^{\infty} a_m \cos(mkx) + b_m \sin(mkx)$$

where

$$a_m = \frac{2}{p}\int_{-\frac{p}{2}}^{\frac{p}{2}} f(x)\cos(mkx)dx \qquad (3.3.1)$$

and

$$b_m = \frac{2}{p}\int_{-\frac{p}{2}}^{\frac{p}{2}} f(x)\sin(mkx)dx \ ,$$

and where the spatial frequency $k = 2\pi / p$. If grating G_1 in figure 3.7 is rotated about the z axis by an angle ψ, then the pitch of G_1 along x is scaled by $1/\cos\psi$ and for any position y the phase of the transmittance of G_1 along x is shifted by an amount $h = h(y) = -y\sin\psi$ (figure 3.7). Let the pitch of grating G_1 be $p_1 = \rho/\cos\psi$, and the finite width of G_1 (aperture width) be described by

$$\mathrm{rect}\left(\frac{x}{Np_1}\right) = \begin{Bmatrix} 1 & \text{for} & -\frac{Np_1}{2} < x < \frac{Np_1}{2} \\ 0 & & \text{elsewhere} \end{Bmatrix} , \qquad (3.3.2)$$

where N is the number of periods or slits, then for any y position, the transmittance of G_1 along x can be described by the Fourier series

$$T_1(x) = \left(\sum_{m=0}^{\infty} a_m \cos\left(\frac{2\pi mx}{p_1} + \frac{2\pi mh}{p_1}\right)\right) \mathrm{rect}\left(\frac{x}{Np_1}\right) ,$$

where

$$a_m = \mathrm{sinc}\left(\frac{m\pi}{2}\right)\cos\left(\frac{2\pi mh}{p_1}\right) , \qquad (3.3.3)$$

and where

$$\mathrm{sinc}(x) = \frac{\sin(x)}{x} .$$

In figure 3.6, it is assumed that G_1 is illuminated by a plane wave. For plane wave

illumination the (complex) amplitude of the light transmitted by G_1 is proportional to the transmittance T_1 . Furthermore, because G_1 is located in the front focal plane of the first lens, the complex amplitude of the transmitted wavefront in the plane of F_1 is proportional to the Fourier transform of the transmittance T_1. From equation (3.3.3) and the definition of the Fourier transform of a function f(x) as

$$F(u) = \frac{1}{2\pi} \int_{-\infty}^{\infty} f(x)\, e^{-jux}\, dx \ , \tag{3.3.4}$$

it follows that the Fourier transform of T_1 is

$$F(T_1) \propto \sum_{m=-\infty}^{\infty} \operatorname{sinc}\left(\frac{m\pi}{2}\right) \cos\left(\frac{2\pi mh}{p_1}\right) \operatorname{sinc}\left(Np_1\left[u - \frac{2\pi m}{p_1}\right]\right) . \tag{3.3.5}$$

The filter F_1 is constructed so as to pass only the +m and -m orders. That is, the slits are centered at the spatial frequencies +/- $2\pi m/p_1$ and are equal in width to the sinc(Np_1u) functions defined in equation (3.3.5). The amplitude transmitted by F_1 is reimaged by the second lens at G_2. As before, the complex amplitude of the wavefront at G_2 is proportional to the Fourier transform of the product of the complex amplitude of the wavefront incident on F_1 and the transmittance of F_1. Provided the widths of the slits in F_1 are equal to the widths of the sinc functions centered at +/- $2\pi m/p_1$, the effect of F_1 is to filter out the +m and -m orders without otherwise altering the amplitude of the wavefront. Therefore, the complex amplitude of the wavefront incident on G_2 can be obtained directly by taking the expression for the mth order of the transmittance T_1 as

$$A_m(x) \propto \operatorname{sinc}\left(\frac{\pi m}{2}\right) \cos\left(\frac{2\pi mh}{p_1}\right) \cos\left(\frac{2\pi mx}{p_1} + \frac{2\pi mh}{p_1}\right) . \tag{3.3.6}$$

The field amplitude behind G_2 is the product of the amplitude of the wavefront incident

on G_2 and the transmittance of G_2 , or $A_m(x)\, T_2(x)$. Like the transmittance of G_1, the transmittance of G_2, of pitch p_2 can be described by a Fourier series as

$$T_2(x) = \left(\sum_{n=0}^{\infty} a_n \cos\left(\frac{2\pi n x}{p_2}\right) \right) \mathrm{rect}\left(\frac{x}{N p_2}\right),$$

where

$$a_n = \mathrm{sinc}\left(\frac{n\pi}{2}\right). \qquad (3.3.7)$$

The symbol N, denotes the number of lines in the grating. The amplitude of the field in the plane of F_2 is proportional to the Fourier transform of the field amplitude directly behind G_2 . From the convolution theorem, it follows that the Fourier transform of the amplitude behind G_2 is the convolution of the Fourier transform of $A_m(x)$ with the Fourier transform of the transmittance of G_2,

$$F(u) = F(A_m) * F(T_2) . \qquad (3.3.8)$$

The Fourier transform of $A_m(x)$ is

$$F(A_m) \propto e^{-j2\pi mh/p_1}\, \delta\left(u - \frac{2\pi m}{p_1}\right) + e^{+j2\pi mh/p_1}\, \delta\left(u + \frac{2\pi m}{p_1}\right). \qquad (3.3.9)$$

It is assumed here that the aperture size of the second grating, G_2 is either the same size as grating one, G_1 or smaller than the aperture of G_1. The rect function in (3.3.9) is therefore omitted. From equations (3.3.8) and (3.3.9) and the fact that $f(x)*\delta(x-x_o) = f(x-x_o)$, it follows that except for a complex phase term, the field amplitude incident on F_2 is just the sum of two fields each of which is proportional to the Fourier transform of T_2. One is centered about $+2\pi m/p_1$ in spatial frequency space, the other is centered about $- 2\pi m/p_1$. This is shown more explicitly by solving for the field amplitude at F_2.

From equation (3.3.7), the Fourier transform of $T_2(x)$ is

$$F(T_2) \propto \left(\sum_{n=-\infty}^{\infty} \operatorname{sinc}\left(\frac{\pi n}{2}\right) \operatorname{sinc}\left(Np_2\left[u - \frac{2\pi n}{p_2}\right]\right) \right) \operatorname{rect}\left(\frac{x}{Np_2}\right) . \qquad (3.3.10)$$

Therefore, the amplitude of the field at the filter F_2 is

$$\begin{aligned} F(u) \propto e^{-j2\pi mh/p_1} & \left[\delta\left(u - \frac{2\pi m}{p_1}\right) * \sum_{n=-\infty}^{\infty} \operatorname{sinc}\left(\frac{n\pi}{2}\right) \operatorname{sinc}\left(Np_2\left[u - \frac{2\pi n}{p_2}\right]\right) \right] \\ + e^{+j2\pi mh/p_1} & \left[\delta\left(u + \frac{2\pi m}{p_1}\right) * \sum_{n=-\infty}^{\infty} \operatorname{sinc}\left(\frac{n\pi}{2}\right) \operatorname{sinc}\left(Np_2\left[u - \frac{2\pi n}{p_2}\right]\right) \right] \qquad (3.3.11) \\ = e^{-j2\pi mh/p_1} & \left[\sum_{n=-\infty}^{\infty} \operatorname{sinc}\left(\frac{n\pi}{2}\right) \operatorname{sinc}\left(Np_2\left[u - \frac{2\pi n}{p_2} + \frac{2\pi m}{p_1}\right]\right) \right] \\ + e^{+j2\pi mh/p_1} & \left[\sum_{n=-\infty}^{\infty} \operatorname{sinc}\left(\frac{n\pi}{2}\right) \operatorname{sinc}\left(Np_2\left[u - \frac{2\pi n}{p_2} - \frac{2\pi m}{p_1}\right]\right) \right] . \end{aligned}$$

Note that each of the n orders in equation (3.3.11) is scaled in width by the total width of the grating G_2, Np_2.

Figure 3.9a shows graphically the amplitude of equation (3.3.11) for m = 1, n = -9 through 9. Figures 3.9b and 3.9c show similar plots for the cases m = 2 and m = 3, respectively, n = -9 through 9. Notice that in each of the figures 3.10a-3.11b there are two peaks symmetric about the zero point for each order n. With increasing m, the distance between these two peaks per order n becomes larger. This implies higher spatial frequency content of the image for larger values of m. What happens physically is, the larger m, the higher the diffracted order off the first grating and the greater the number of fringes present in the output image. This becomes more evident when one spatial frequency is filtered through F_2 and reimaged at the viewing screen.

The exact increase in the number of fringes, or the multiplication factor will now be

established. Orders of n overlap with orders of n' = n + 2m where n is the smaller of the two order numbers. In figure 3.11a and b and equation (3.3.11) it can be seen that for each order n there exists two discrete peak spatial frequencies. Figures 3.10a and b show the locations of peak frequencies for n = 1 and n = -1. The plots in figure 3.11 show the shift in frequency content for n = 2 and n = -2. By comparing figures 3.11b and 3.12 the right peak of n = - 2 in figure 3.11b and the left peak of order n = 0 (figure 3.12) are located at approximately the same frequency. The left peak of any n order corresponds to the first term in (3.3.11) or the peak located at $2\pi n/p_2 - 2\pi m/p_1$ and the left peak of any n order corresponds to the second term of (3.3.11) or the peak located at $2\pi n/p_2 + 2\pi m/p_1$. The frequency location in which there is a peak of order n and a peak of order n' = n + 2m are what is typically referred to as an r group or r order [18-19]. For example, in figure 3.9a the discrete spatial frequencies are labeled as r-orders or as r-groups where the center peak is considered r = 0, the next r = 1 and so on. The relationship between r and n is n=r-m and n'=r+m.

Figure 3.13 illustrates the r groups for m = 1, 2 and 3. It is a single r group that is filtered by F_2. From equation (3.3.11) the field amplitude of an r order group is

$$\begin{aligned} F_r(u) \propto\ & e^{j2\pi mh/p_1}\,\mathrm{sinc}\left(\frac{n\pi}{2}\right)\mathrm{sinc}\left(Np_2\left[u-\left\{\frac{2\pi n}{p_2}+\frac{2\pi m}{p_1}\right\}\right]\right) \\ & + e^{-j2\pi mh/p_1}\,\mathrm{sinc}\left(\frac{n'\pi}{2}\right)\mathrm{sinc}\left(Np_2\left[u-\left\{\frac{2\pi n'}{p_2}-\frac{2\pi m}{p_1}\right\}\right]\right). \end{aligned} \tag{3.3.12}$$

The inverse Fourier transform yields the complex amplitude of the rth order group at the viewing screen which is

$$\begin{aligned} A_r(x) \propto\ & e^{j2\pi mh/p_1}\,\mathrm{sinc}\left(\frac{n\pi}{2}\right)\mathrm{rect}\left(\frac{x}{Np_2}\right)e^{-j\left\{\frac{2\pi n}{p_2}+\frac{2\pi m}{p_1}\right\}x} \\ & + e^{-j2\pi mh/p_1}\,\mathrm{sinc}\left(\frac{n'\pi}{2}\right)\mathrm{rect}\left(\frac{x}{Np_2}\right)e^{-j\left\{\frac{2\pi n'}{p_2}-\frac{2\pi m}{p_1}\right\}x}. \end{aligned} \tag{3.3.13}$$

Substituting n' = n + 2m, $p_1 = \rho / \cos\psi$, and $\rho = p_2$ into (3.3.13) and solving for the intensity, yields the image at the output screen of figure 3.6

$$I_r(x) \propto \text{rect}\left(\frac{x}{N\rho}\right)\left[\ \text{sinc}^2\left(\frac{n\pi}{2}\right) + \text{sinc}^2\left(\frac{\{n+2m\}\pi}{2}\right)\right.$$
$$\left. + 2\,\text{sinc}\left(\frac{n\pi}{2}\right)\text{sinc}\left(\frac{\{n+2m\}\pi}{2}\right)\cos\left\{\frac{4\pi mx}{\rho}(\cos\psi - 1) - \frac{4\pi mh\cos\psi}{\rho}\right\}\right]. \qquad (3.3.14)$$

The last term in (3.3.14) is the Moire pattern. The expression in (3.3.14) implies that as higher orders of m are chosen the sensitivity of the phase term increases, where

$$\text{phase} = \frac{4\pi mh\cos\psi}{\rho}\ .$$

Therefore, the sensitivity of the Moire fringe pattern to a translation h, in any r group monitored, can be adjusted by filtering through a different order pair m, from the first grating G_1. The pitch of the Moire pattern is multiplied by m as can be seen in (3.3.14).

The visibility of the Moire pattern is governed by the difference in amplitude between the n'th order and the nth order that form an r order group. The visibility is described mathematically as

$$\text{Visibility} = \frac{2\,\text{sinc}\left(\frac{n\pi}{2}\right)\text{sinc}\left(\frac{\{n+2m\}\pi}{2}\right)}{\text{sinc}^2\left(\frac{n\pi}{2}\right) + \text{sinc}^2\left(\frac{\{n+2m\}\pi}{2}\right)}\ .$$

The r order groups that contain the highest visibility are formed by n orders that are closest in magnitude when combined in the Fourier plane. Therefore, as one might expect based on symmetry, r = 0 will always have the highest visibility no matter what the value of m. However, except for the case where m = 1, r = 0 will not have the highest intensity.

3.3.2 Frequency Based Phase Detection of the Multiplied Moire Fringes

If the grating G_1 is translated along the x direction in time at a constant velocity then h becomes a function of time and can be written as

$$h(t) = h(y) + vt\,.$$

The intensity expression at the output screen for any r order group is then

$$I_r(x) \propto a_m^2 \,\mathrm{rect}\left(\frac{x}{N\rho}\right)\left[B + B'\cos\left\{\frac{4\pi mx}{\rho}(\cos\psi - 1) - \frac{4\pi mh(y)\cos\psi}{\rho} - \frac{4\pi mvt\cos\psi}{\rho}\right\}\right],$$

where

$$B = \mathrm{sinc}^2\left(\frac{n\pi}{2}\right) + \mathrm{sinc}^2\left(\frac{\{n+2m\}\pi}{2}\right),$$

$$B' = 2\,\mathrm{sinc}\left(\frac{n\pi}{2}\right)\mathrm{sinc}\left(\frac{\{n+2m\}\pi}{2}\right), \qquad (3.3.15)$$

and

$$a_m^2 = \mathrm{sinc}^2\left(\frac{n\pi}{2}\right)\cos^2\left(\frac{2\pi mh(y)\cos\psi}{\rho} + \frac{2\pi mvt\cos\psi}{\rho}\right).$$

The last term of (3.3.15) is the Moire pattern. The last term is found by the product of a_m^2 and the cosine term in $I_r(x)$ of (3.3.15) and is

$$\text{last term of } I_r(x) \propto \cos\left(\frac{4\pi mx}{\rho}(\cos\psi - 1)\right) + \cos\left\{\frac{4\pi mx}{\rho}(\cos\psi - 1) - \frac{8\pi mh(y)\cos\psi}{\rho} - \frac{8\pi mvt\cos\psi}{\rho}\right\}. \qquad (3.3.16)$$

To extract the phase information from the Moire pattern (last term) in (3.3.16), a detection system would lock in on the scanning frequency $\omega = 8\pi mv\cos\psi/\rho$. It is apparent from (3.3.16) that the frequency of the fringes scanning across x in time increases with increasing orders of m. Electronic phase detection of this moving fringe pattern would again yield a phase that is a function of h given by (3.3.16).

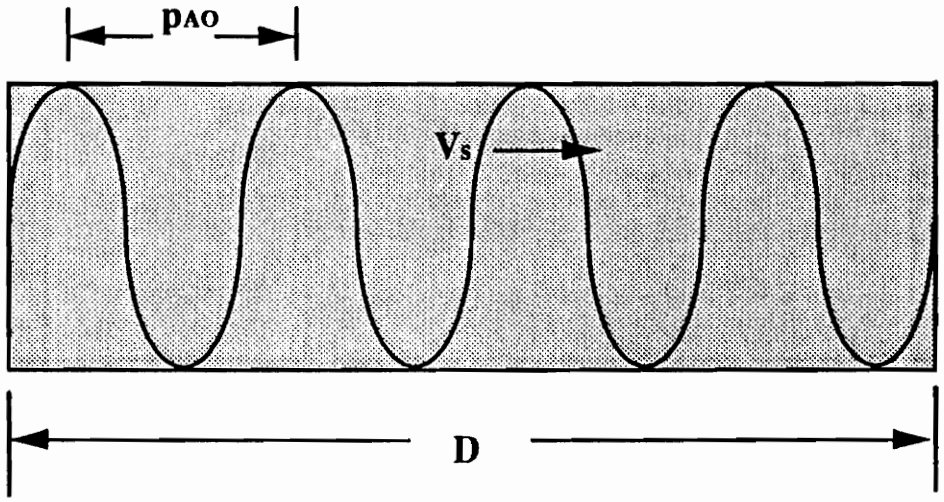

Acousto-Optic Modulator

Figure 3.1

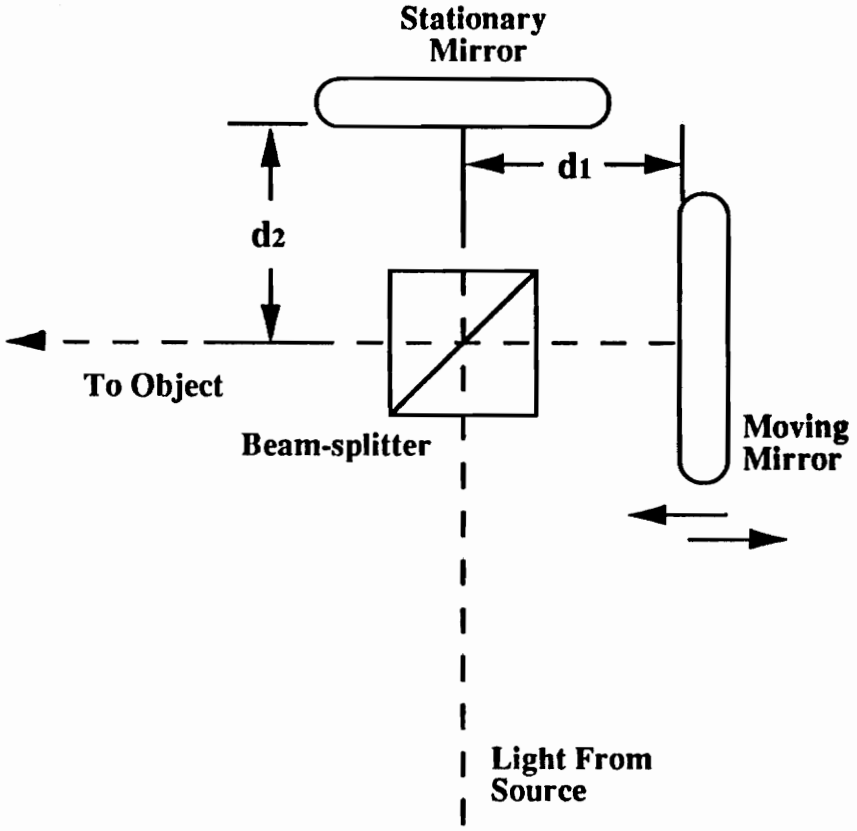

Michelson Interferometer With One Moving Mirror

Figure 3.2

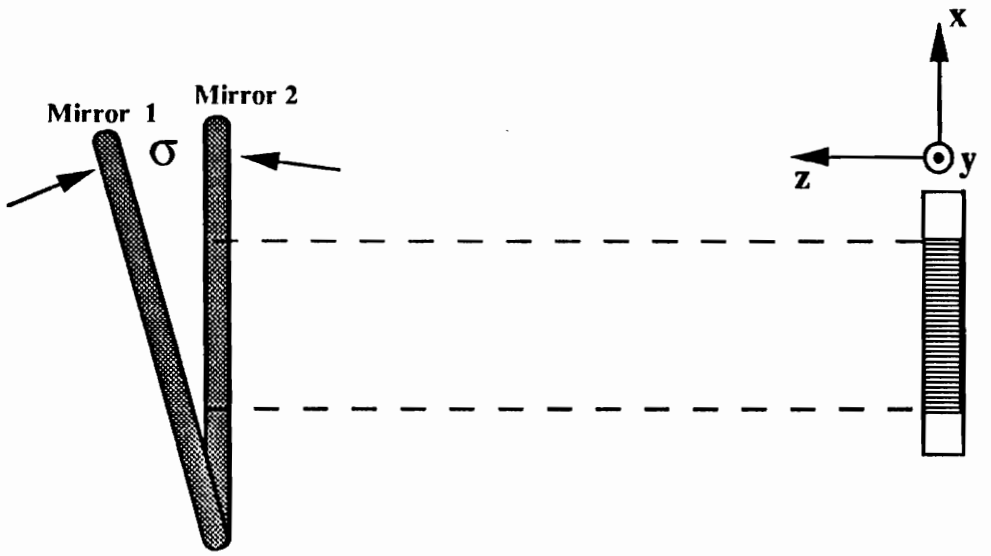

Two Mirrors of a Michelson Interferometer

Figure 3.3a

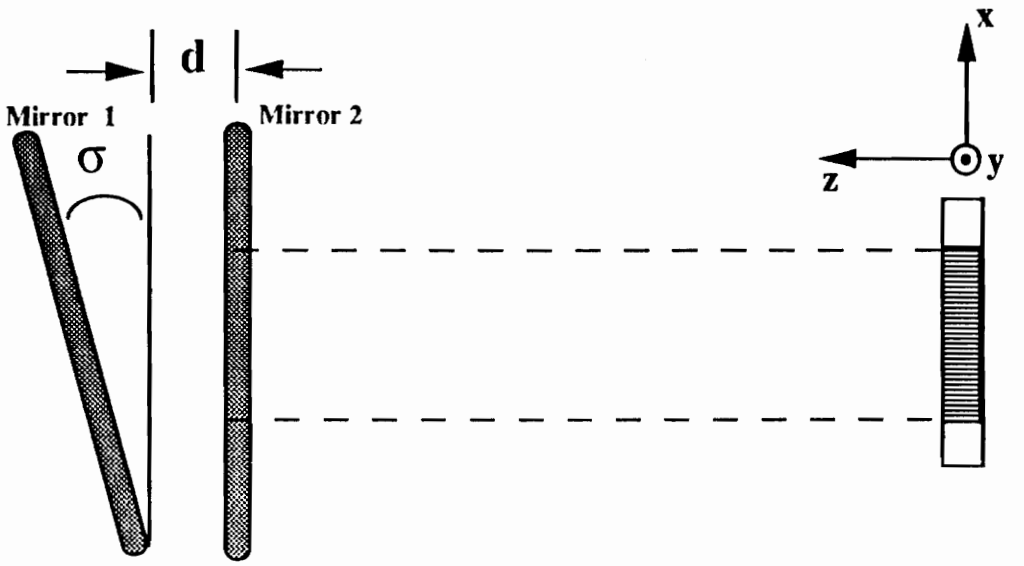

Two Mirrors of a Michelson Interferometer

Figure 3.3b

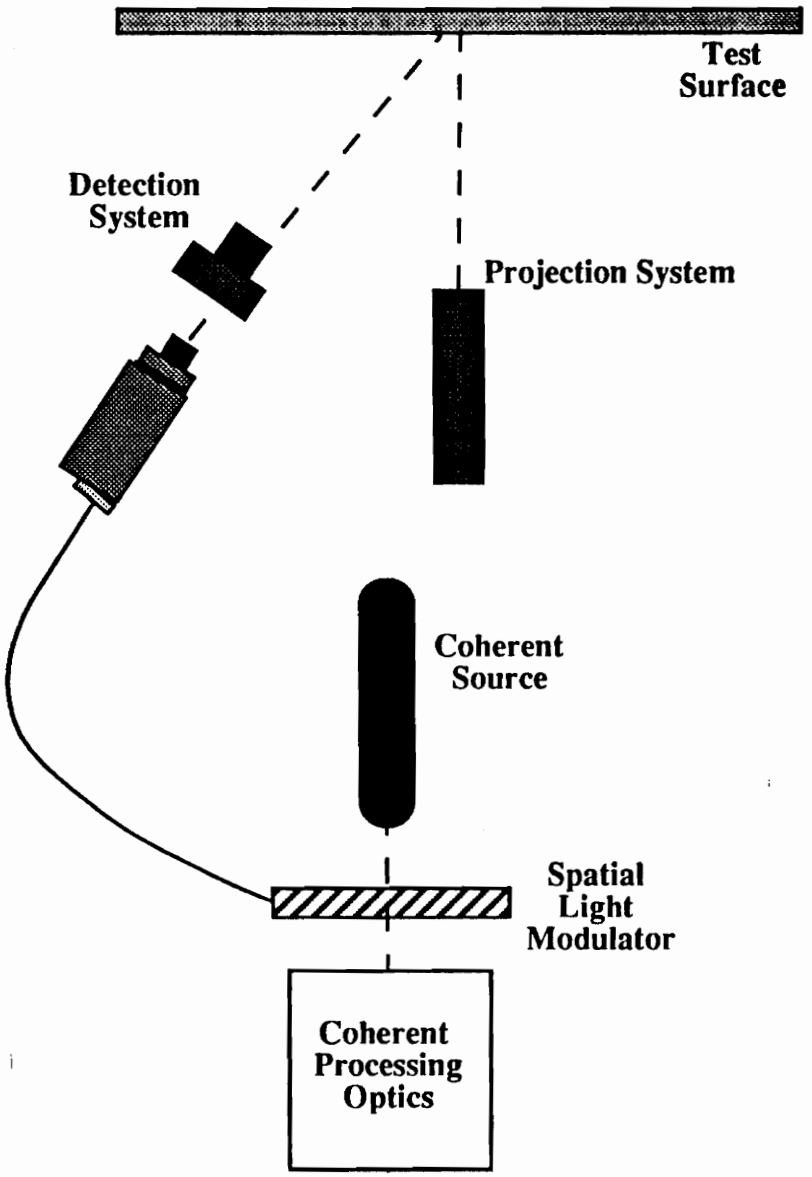

Transducing From an Incoherent System to a Coherent System

Figure 3.4

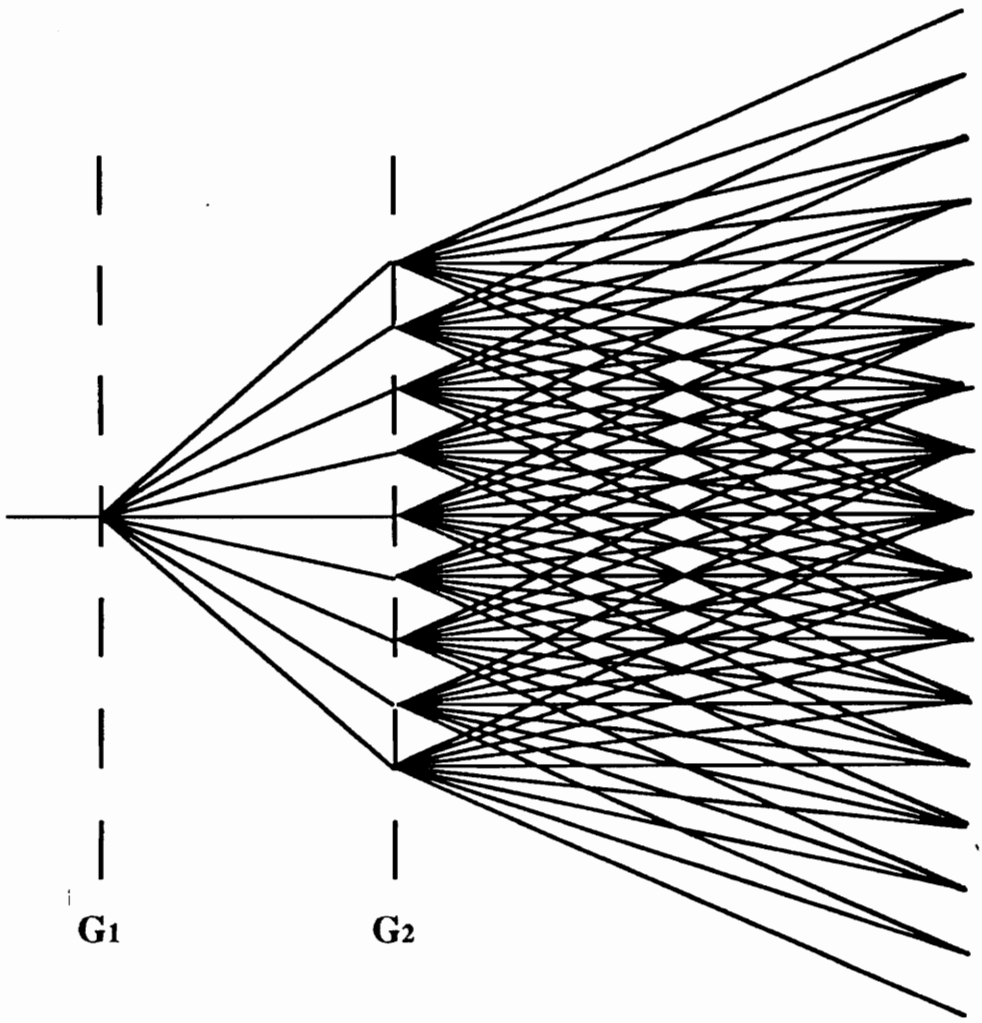

Double Diffraction from Two Gratings Superimposed

Figure 3.5

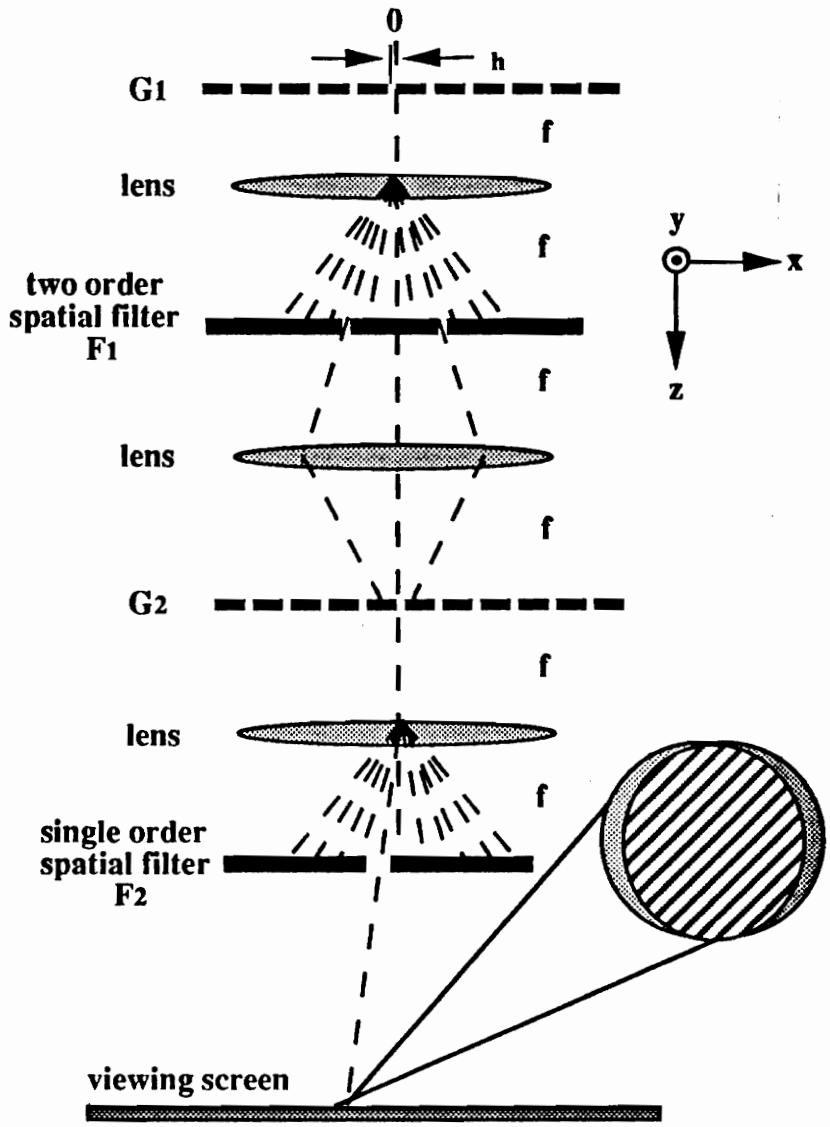

Schematic for Fringe Multiplication

Figure 3.6

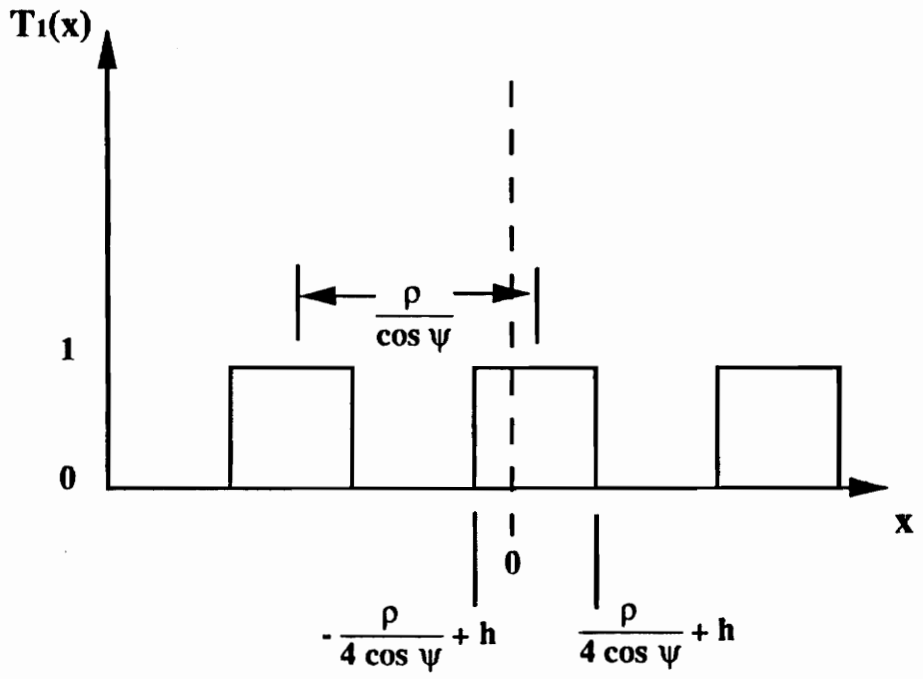

Ronchi Grating, G1
Figure 3.7

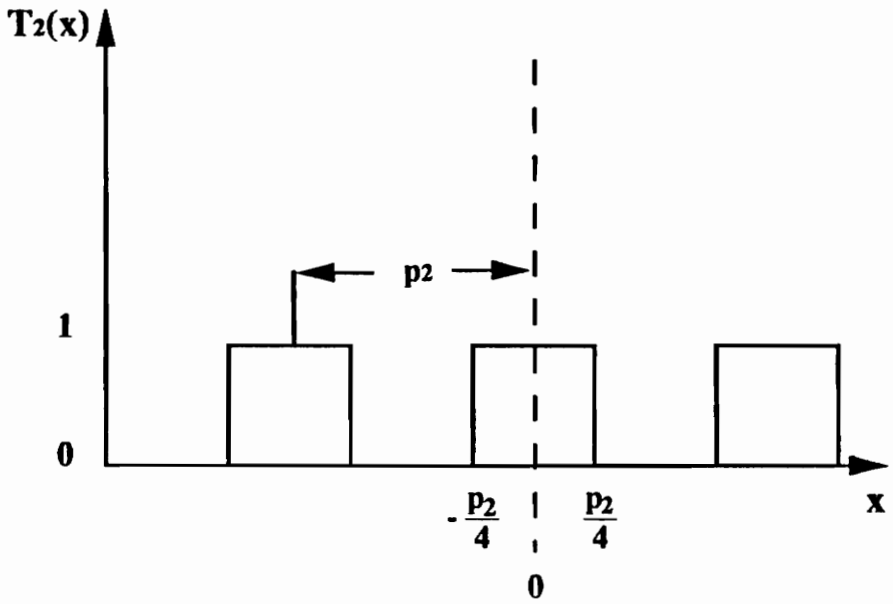

Ronchi Grating, G2

Figure 3.8

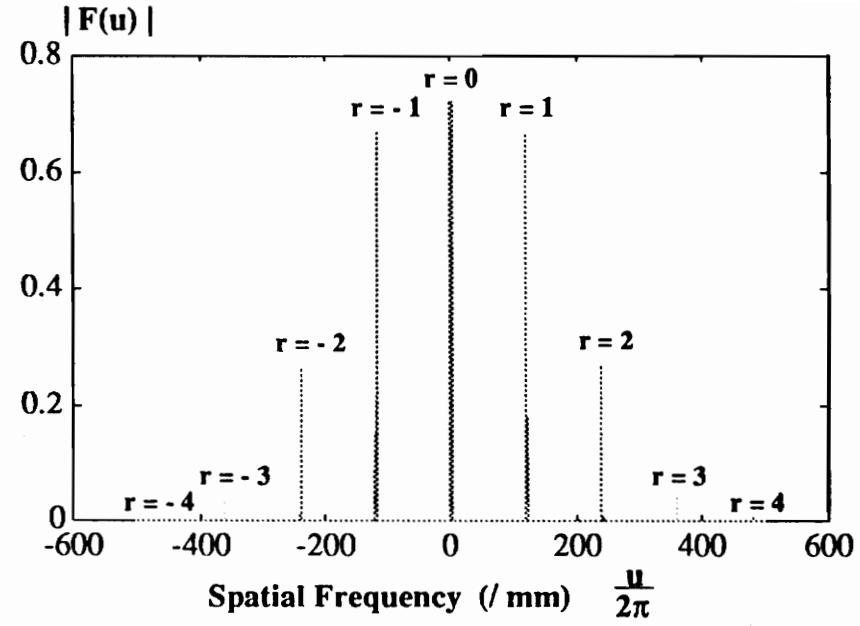

F(u) for m = 1 and n from -9 to 9

Figure 3.9a

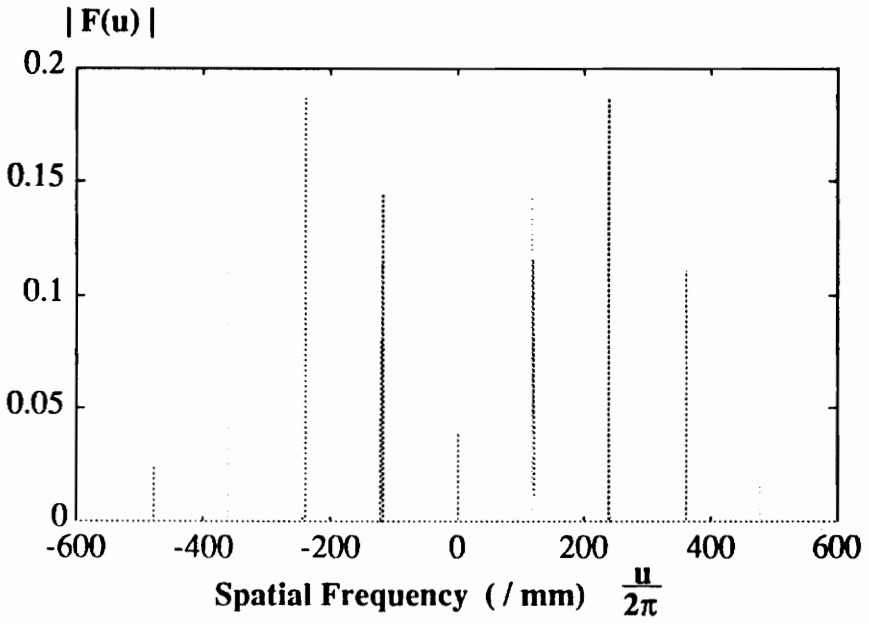

F(u) for m = 2 and n from -9 to 9

Figure 3.9b

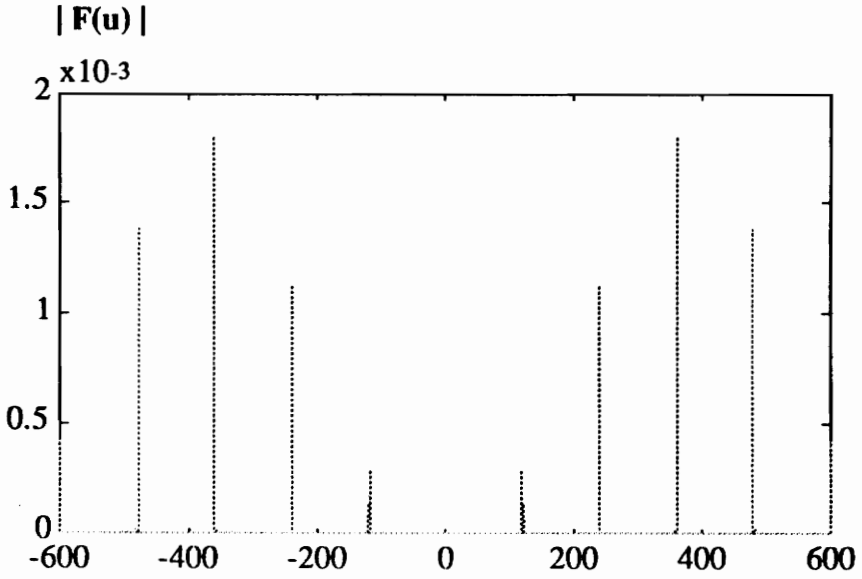

F(u) for m = 3 and n from -9 to 9

Figure 3.9c

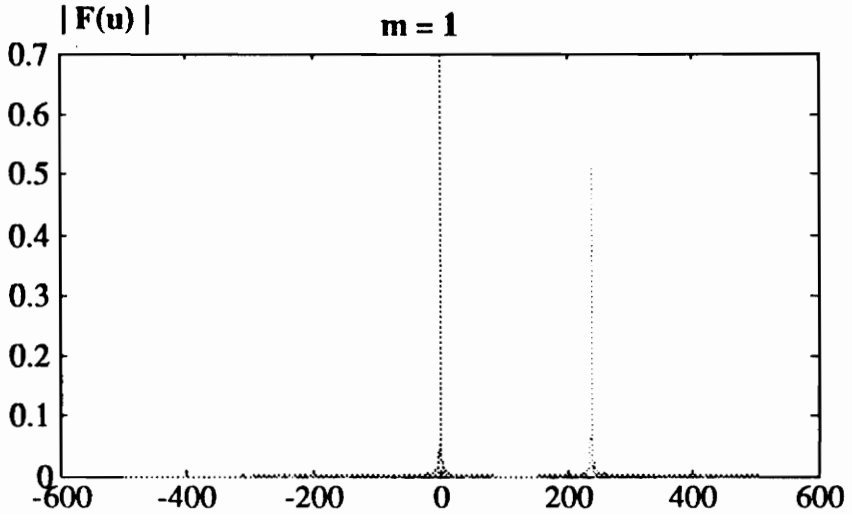

Magnitude of the n = 1st order of F(u)

Figure 3.10a

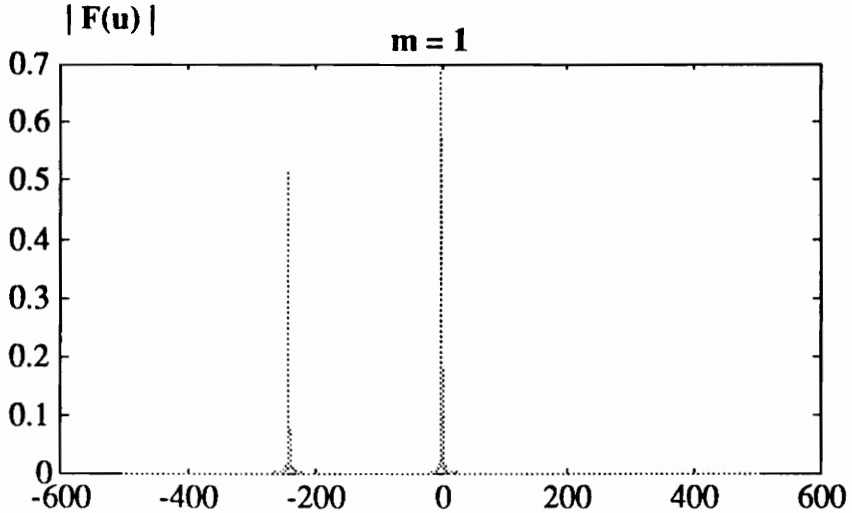

Magnitude of the n = -1st order of F(u)

Figure 3.10b

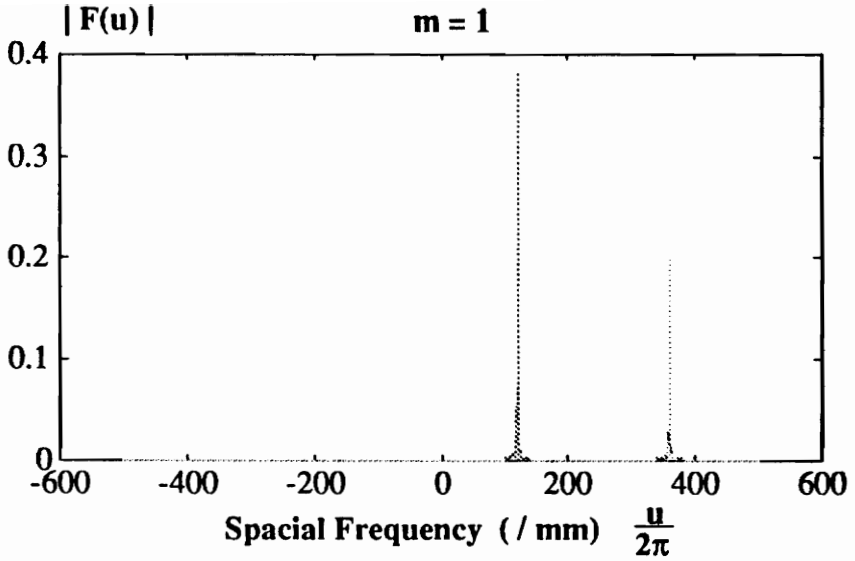

Magnitude of the n = 2nd order of F(u)

Figure 3.11a

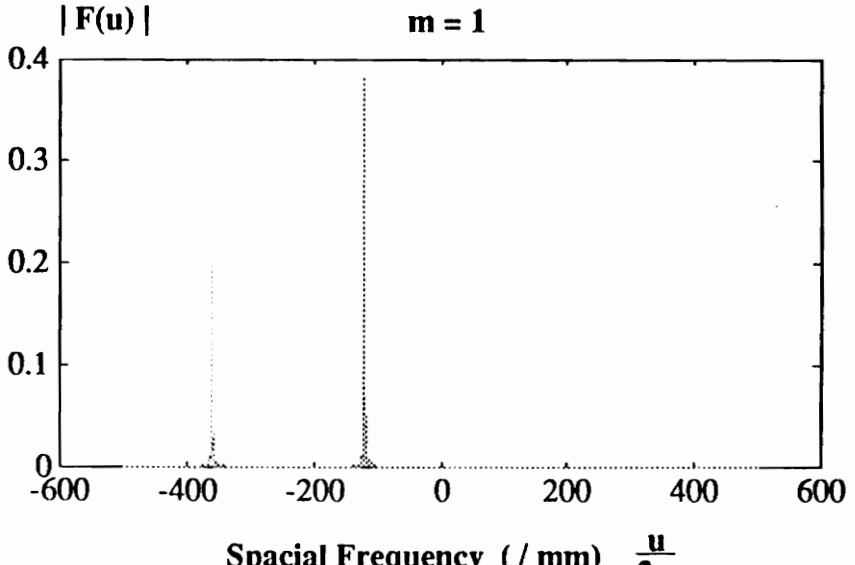

Magnitude of the n = - 2nd order of F(u)

Figure 3.11b

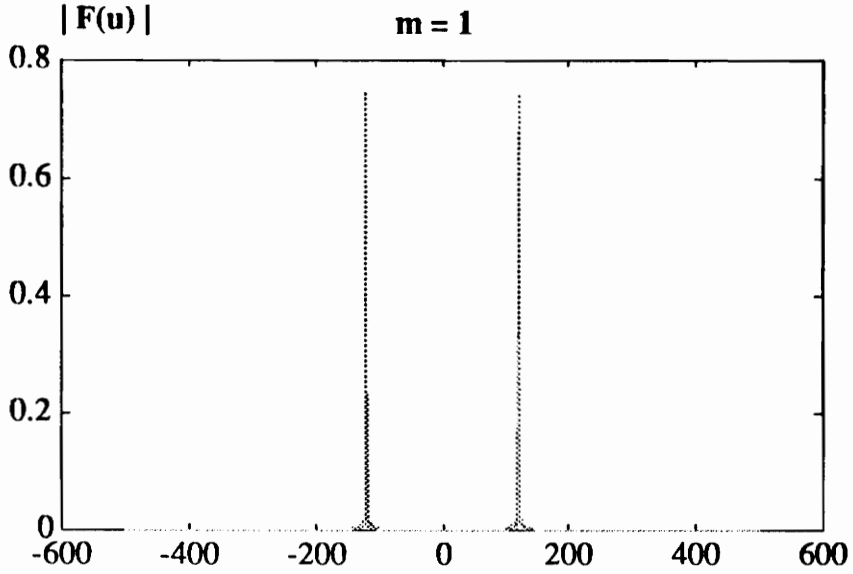

Magnitude of the n = 0th order of F(u)

Figure 3.12

m = 1

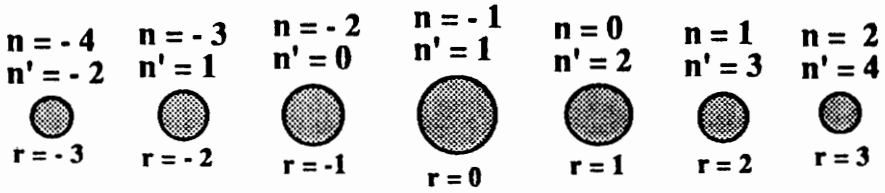

F(u) with m = 1 and n = -4 to 4

Figure 3.13a

m = 2

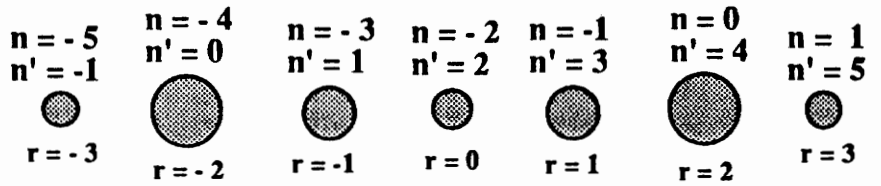

F(u) with m = 2 and n = -5 to 5

Figure 3.13b

m = 3

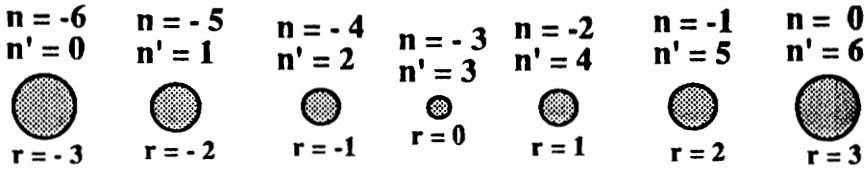

F(u) with m = 3 and n = - 6 to 6

Figure 3.13c

4.0 Projection Moire at Large Scale

The analysis of projection moire contour sensing with coherent processing at large scale can be divided in two sections. Section one considers the power, displacement sensitivity, and bandwidth at large scale of the incoherent projection moire system. Section two addresses the effects of large scale on the power, sensitivity and bandwidth of the coherent processing system.

4.1 The Incoherent Projection Moire System

4.1.1 Source Power

Let the power from the source illuminating G_A be P_S. The output beam from the source is focused, filtered, collimated and expanded before illuminating G_A. At each lens and filter the beam experiences power losses. If the transmission of the power after incurring these losses is represented as τP_s where τ is (1 - losses) and A_{col} is the area of G_A that is illuminated, then the intensity of the illumination at G_A can be written

$$I_{G_A} = \frac{\tau P_s}{A_{col}} , \tag{4.1.1}$$

where the units are watts/mm^2. Assume that the losses due to the projection optics to surface Σ are taken in account by τ in (4.1.1). The intensity at surface Σ, is scaled by the magnification M_A or

$$I_\Sigma = \frac{I_{G_A}}{M_A^2} , \tag{4.1.2}$$

where $(M_A)^2$ is the ratio of the area of Σ to the area of the collimated beam.

The intensity at the second grating G_B is a function of the scattering of light from the surface Σ. Assume that surface Σ is a diffuse surface which reflects all light incident upon it in the form of scattering. By Lambert's law, the intensity of the reflection from surface Σ is a fraction of the incident intensity. Therefore, let η be the symbol for the ratio of intensity reflected from Σ, M_B be the magnification from Σ to G_B and $F^{\#}_1$ be the f-number of the imaging lens to G_B. The intensity at G_B is

$$I_{G_B} = \frac{\eta I_\Sigma}{M_B^2 \left(2 F_1^{\#}\right)^2} \tag{4.1.3}$$

where $(M_B)^2$ is the ratio of the illuminated area at G_B to the illuminated area of Σ and the f-number is defined as $F^{\#}$ = focal length / diameter of lens. It is assumed that the image of the moire pattern behind G_B is recorded by a charge-coupled device camera (CCD camera). The camera lens will focus the moire pattern on a chip of integrated photodetectors. Let the magnification from the moire pattern image to the CCD chip be M_c, the ratio of the chip area to the moire pattern area be M_c^2 and the f-number of the camera lens be $F^{\#}_2$. The intensity at the CCD camera is

$$I_{CCD} = \frac{I_{G_B}}{M_C^2 \left(2 F_2^{\#}\right)^2} \ . \tag{4.1.4}$$

Substituting the expression for I_{G_B} into (4.1.4) the expression for the intensity at the CCD camera becomes

$$I_{CCD} = \frac{\eta \tau P_s}{16 \left(M_A M_B M_c F_1^{\#} F_2^{\#}\right)^2 A_{col}} \ . \tag{4.1.5}$$

To determine a numerical value for the total power losses in (4.1.5) assume the following: a reflectivity of 50 %, $M_A = 9$, $M_B = .04$, $M_c = .5$, 20% total loss due to lenses, $F^{\#}_1 = 20$,

and $F^{\#}_2 = 5.8$. Therefore, the intensity

$$I_{CCD} = (2.9*10^{-3})\cdot P_s / A_{col} \text{ (watts/mm}^2\text{)}.$$

The power from the source to the CCD camera can drop by three orders of magnitude if it is assumed that the source spot size is about one mm in diameter.

Continuous wave (CW) solid state lasers of two watts power output are available. A typical CCD camera can detect in the microwatt range with possibly a decrease in the bandwidth by a delay in shutter speeds. Using the above example a two watt laser would result in a 6 milliwatt signal which the camera is capable of detecting.

Using higher quality lenses (other than in the previous example) can increase τ and a larger reflectivity coefficient η, can result in a higher intensity output at the camera. The collimation area can be reduced but not without compromising the moire pattern resolution and limiting the sensitivity of the system to out of plane displacements of Σ. However, coarse resolution of the moire pattern is allowable since the coherent processing system functions to regain sensitivity lost in the incoherent moire system.

4.1.2 Resolution and Range

The sensitivity of the system to out of plane displacements z_o, is limited by the pixel dimensions of the camera. If the CCD camera circuit consists of pixels of width Δ_{CCD} then the pitch of the moire fringes can be no smaller than $2\Delta_{CCD}$ assuming one to one magnification, and still be resolved or

$$p_{moire} > 2\,\Delta_{CCD} \ . \qquad (4.1.6)$$

For a camera containing a chip with pixel dimension $\Delta_{CCD} = 6.6$ microns/pixel, the moire

spatial frequency can be no finer than 76 lp/mm.

The smallest z_o detectable by the system, based on only the CCD camera resolution can be determined by the smallest resolvable grating pitch. Assume that p_B is the grating pitch of G_B and that the magnification from behind G_B to the CCD camera chip is one. Recall from chapter two that the expression for p_{moire} is

$$p_{moire} = \frac{p_B}{\sin\left(\frac{\theta}{2}\right)}\left(\frac{\cos\phi}{\cos\phi + 1}\right) .$$

Substituting the expression for p_{moire} into (4.1.6), the limit on pitch of the gratings used in the projection system is

$$p_B > 2\,\Delta_{CCD}\,[1+\cos\phi]\,\sin\left(\frac{\theta}{2}\right) . \qquad (4.1.7)$$

The limit on pitch also affects the sensitivity of the phase shift per out of plane displacement z_o. Recall the expression for sensitivity from section two, $S = \text{phase}/z_o = M_B\sin\phi/p_B$. Substituting (4.1.7) into the sensitivity expression,

$$S = \frac{\text{phase}}{z_o} < \frac{M_B \sin\phi}{2\,\Delta_{CCD}\,[1+\cos\phi]\,\sin\left(\frac{\theta}{2}\right)} . \qquad (4.1.8)$$

Using (4.1.8) to calculate 1/S yields the maximum detectable out of plane displacement z_o as

$$\frac{1}{S} = \frac{z_o}{\text{phase}} > \frac{2\,\Delta_{CCD}\,[1+\cos\phi]\,\sin\left(\frac{\theta}{2}\right)}{M_B \sin\phi} . \qquad (4.1.9)$$

For example, if Δ_{CCD} = 6.6 microns/pixel, viewing angle ϕ = 45 degrees, and angular misalignment between the two gratings is $\theta/2$ = 2 degrees, then if a phase shift of 1 degree could be detected the smallest possible out of plane motion detectable would be $1/M_B$

microns. At a magnification $M_B = 1$ the smallest resolvable z_o would be 1 micron and at a magnification of .02, z_o would be 50 microns. A magnification as small as .02 would be used in the case where a 1 meter area is monitored and imaged on a grating approximately 2 cm wide. However, if the projection moire system is incoherent, diffraction effects impose a limit on how small the Ronchi grating pitches can be. From experience in the laboratory this limit appears to be at a pitch of 50 microns. When using a white light source, gratings of finer resolutions than 20 lp/mm diffract the illumination and decrease the visibility of the moire fringes. Therefore, the out of plane displacement per unit degree phase shift would be larger than 4.2 microns for a magnification of one and 210 microns for a magnification of .02 when 50 microns is used for the limit on the grating pitch (in place of $2\Delta_{CCD}$). Based on this diffraction limit the overall conclusion is that the larger the area being monitored, the lower the sensitivity to out of plane displacements. Each increase in magnitude of the monitored area on a test surface results in a decrease in magnitude of the sensitivity to displacements of the surface.

In contrast to the minimum displacement per phase shift possible is the largest displacement possible. In this case the pitch of the moire pattern would have to be less than half of the total length of the photodetector chip or,

$$p_{moire} < \frac{\text{N pixels} * \Delta_{CCD}}{2} \quad . \tag{4.1.10}$$

The effect on the largest detectable z_o per phase shift would be

$$\frac{z_o}{\text{phase}} < \frac{\text{N pixels } \Delta_{CCD} [1+\cos\phi] \sin\left(\frac{\theta}{2}\right)}{2 M_B \sin\phi} \quad . \tag{4.1.11}$$

Using the previous example where the total number of pixels is 512 across one dimension only, the largest z_o per unit of phase shift would be 142 microns for a magnification of one

and 7.1 mm for a magnification of .02. .

It is evident from the above discussion that for an incoherent projection moire system that uses a CCD camera, the smallest z_0 measurable is not affected by the camera resolution. The sensitivity of the system to z_0 is more limited by the use of incoherent illumination, in which to avoid diffraction effects at the cost of visibility, the grating pitch p_B can be no smaller than 50 microns. Based on the relationship between grating pitch and out of plane displacement, z_0 must be greater than 4.2 microns with unit magnification. At larger magnifications such as .02 which would be required to monitor a 1 meter area, the limit of zo is 210 microns. Measuring large displacments is limited by the size of the CCD array. Overall, the magnification of the system will be limited to the sensitivity required. Measuring large surfaces would then require some sensitivity enhancement. This arrangement would then meet the demand for monitoring a large diffuse surface while still maintaining high system sensitivity. Hence the motivation for sensitivity enhancement provided by the coherent processing system.

4.1.3 Bandwidth

The bandwidth of the moire projection system is limited by the bandwidth of the CCD camera. A typical CCD camera operates at 60 Hz frame rate and can have 20 MHz readout rate per pixel provided the intensity to the photodetector circuit of the camera is adequate. An entire 512 by 512 pixel screen can be downloaded in under 13 milliseconds. It is expected that a large flexible structure will not vibrate at frequencies any higher than a few Hz [1]. Therefore, this projection system is adequate.

4.2 The Coherent Processing System

To enter the coherent processing stage the signal from the CCD camera is used to drive an electronically addressable spatial light modulator (SLM). The SLM is used as a mask and illuminated by a coherent source to recreate the moire pattern in coherent form. The SLM mask is then the first grating G_1 in the coherent processing system of figure 3.6. Assume for this discussion that the overall magnification of the coherent processing system is one to one.

4.2.1 System Power Considerations

Let the power of the source illuminating the SLM (G_1 in Figure 3.6) be P_{sc}. The power reaching G_2 will be reduced by the losses due to the lenses and the losses caused by filtering only two orders by filter F_1. The power of the beam transmitted by F_1 is determined by the transmission coefficient of the order pair m passed through the filter.

The transmission coefficients $\tau_{m,}$ for all m sum to one. The transmission coefficients are found by the square of the amplitude magnitude of each Fourier component for order m over the sum of all the components in the Fourier transform at F_1. Assumming slit width / slit spacing is .5 the percentage of power transmitted through the filter F_1 is described by

$$\tau_m = \frac{2\,\mathrm{sinc}^2\left(\frac{m\pi}{2}\right)}{1 + \sum_{m=1}^{\infty} 2\,\mathrm{sinc}^2\left(\frac{m\pi}{2}\right)} \qquad (4.2.1)$$

for each m order pair. Note that the one in the denominator of (4.2.2) is the power

component of the m = 0 order or 1 = $\text{sinc}^2(0)$ of which there is only one. Figure 4.1 shows a table of values of τ_m for m order pairs up to 20 and a graphic representation of (4.2.2) for m order pairs up to 10. It is apparent from the graph and table in Figure 4.1 that only the odd m order pairs contain significant power and that the component m = 19 has three orders of magnitude less power than the m = 0 component.

The transmission of power to G_2 is,

$$P_{G_2} = P_{sc}\ \tau_{lenses}\ \tau_m\ , \tag{4.2.2}$$

where τ_{lenses} is the transmission through the lenses from G_1 to the second grating G_2. After G_2, the beam experiences losses from two more lenses and the filter F_2 which only passes a single r order group. Power at the detector is given by

$$P_{det} = P_{G_2}\ \tau_{lenses}\ \tau_r \tag{4.2.3}$$

where τ_{lenses} is the transmission coefficient based on the losses from the lenses and τ_r is the transmission coefficient of a particular r order group. The expression for the transmission coefficient, τ_r for any r group, is the percentage of total power of the spectrum located at F_2, passed through F_2 and is written

$$\tau_r = \frac{\left\{\text{sinc}\left(\frac{n\pi}{2}\right) + \text{sinc}\left(\frac{(n+2m)\pi}{2}\right)\right\}^2}{\sum_{r=-\infty}^{\infty}\left\{\text{sinc}\left(\frac{n\pi}{2}\right) + \text{sinc}\left(\frac{(n+2m)\pi}{2}\right)\right\}^2}\ , \tag{4.2.4}$$

where r - m = n. Figure 4.2 is a graph of (4.2.4) with m = 1 for r groups zero through ten. The transmission coefficients τ_r for r groups 0 through 20 are listed in: Table 4.1 for m = 1, Table 4.2 for m = 3, and Table 4.3 for m = 5. Notice that the largest amount of power can be found in the r = m component for m = 3 and m = 5. This is true for all m order pairs with the exception of m = 1. Using the m = 1 order pair, the largest amount of power is

contained in the r = 0 group. Notice that at the odd r groups for any given m (with the exception of r = m) the transmission drops to zero. Since the r = m group contains the largest amount of power of all the other components in the spectrum , it would seem logical to pass the r = m order group with F_2. However, the component r = m also has the lowest visibility of fringes when reimaged at the detector. Figures 4.3a-d are visibility of fringes plots for r groups 0 to 20 with m = 1, 3, 5 and 7, respectively. The r group of lowest visibility is the r = m order group. It is also true that the visibility is one in odd r order groups where $\tau_r = 0$ and in the r = 0 group where $\tau_0 > 0$ for all m. Therefore, the r group that would provide the best visibility for all order pairs m, with a transmission coefficient greater than zero is the r = 0 group. Table 4.4a lists the transmission coefficients for order pairs 3 through 19 and Table 4.4b lists the transmission coefficients of the r = 0 group for m = 3 through 19. Under the assumption that the r = 0 group is passed by filter F_2, the transmission coefficients τ_m and τ_r are determined by the amount of sensitivity required from the system or by the order pair m.

The power at the detector is determined by substituting (4.2.2) into (4.2.3) and is

$$P_{det} = P_{sc}\ \tau_m\ \tau_r\ \tau_{all\ lenses} \tag{4.2.5}$$

where $\tau_{all\ lenses}$ is the percentage of power transmission after propagation through all the lenses in the processing system. If the lenses decrease the power by no more than 30% and the m = 19 order pair is passed by filter F_1 (Table 4.4a,b), the power at the detector would be

$$P_{det} = P_{sc}\ (9 \bullet 10^{-7}).$$

Therefore, it can be concluded that when selecting a high system sensitivity to h or a large m, the power from the source to the detector can drop by seven orders of magnitude. However, if the m = 3 order pair is chosen the power decreases by three orders of

magnitude and only one order of magnitude for m = 1. The power required for the coherent processing system would therefore depend on the sensitivity requirement for the system. The higher the sensitivity requirement the more power required from the source used to illuminate the SLM.

The power is also influenced by the visibility of the fringe pattern on the SLM. If the visibility is poor the r = 0 order group power content will decrease as the power to the r = +/- m orders increase. In this case, it may be more beneficial to monitor the r = 2 or r = -2 order groups since the visibility in these orders is high and these orders are closer to the r = m order group.

4.2.2 Sensitivity

The sensitivity of h per phase shift will depend on the resolution of the SLM, the size of photodetector, and the choice of m (system sensitivity required), the order pair filtered from the first grating. If the size of a single pixel in the SLM is Δ_{SLM} along the x direction then the pitch ρ (G_1 is the SLM mask) must be greater than twice the pixel size or,

$$\rho > 2\,\Delta_{SLM} \ . \tag{4.2.6}$$

Recall, that the phase term of the moire pattern containing h is

$$\text{phase} = \frac{8\pi m h \cos\psi}{\rho} \ .$$

The sensitivity of h per degree phase shift is therefore,

$$\frac{h}{\text{phase}} = \frac{\rho}{4m\cos\psi} \ . \tag{4.2.7}$$

Substituting (4.2.6) into (4.2.7)

$$\frac{h}{\text{phase}} > \frac{\Delta_{SLM}}{2\,m\cos\psi}\,, \tag{4.2.8}$$

the sensitivity of h is limited by the pixel size of the SLM.

The pitch of the moire pattern p_{moire} is limited by the size of the photodetector, which also places restrictions on sensitivity (4.2.8). The size of the detector used must be smaller than a single fringe of the moire pattern. If the size of the photodetector along the x direction is w_{det} then the restraint on the pitch of the moire pattern is,

$$p_{moire} > 2\,w_{det} \tag{4.2.9}$$

From chapter three the pitch of the moire pattern is contained in the term

$$\frac{4\pi m x}{\rho}(1 - \cos\psi) \quad \text{where} \quad p_{moire} = \frac{\rho}{2m(1 - \cos\psi)}$$

Substituting the expression for the pitch of the moire pattern in to (4.2.9) the condition is

$$\frac{\rho}{2m(1 - \cos\psi)} > 2\,w_{det}\,. \tag{4.2.10}$$

It is possible to determine ρ such that the condition in (4.2.10) is satisfied but the condition in (4.2.6) is not. In order to meet both conditions for any order pair m, a further condition, from combining (4.2.6) and (4.2.10) must be placed on ψ where,

$$1 - \frac{\Delta_{SLM}}{2m\,w_{det}} < \cos\psi\,, \tag{4.2.11}$$

and solving for ψ

$$\psi < \cos^{-1}\left[1 - \frac{\Delta_{SLM}}{2m\,w_{det}}\right]. \tag{4.2.12}$$

A typical value for the pixel size of an SLM is $\Delta_{SLM} = 7.0$ microns. Photodetectors that have high bandwidths can have diameters of $w_{det} = 1.0$ mm. Since it is unlikely that an m higher than 19 would be used due to power losses, using an m = 19 should suffice for meeting the condition of (4.2.12). With these assumptions the misalignment angle ψ must be smaller than 1.1 degrees. Substituting 1 degree for ψ in (4.2.8) the sensitivity of h per unit phase is

$$\frac{h}{\text{phase}} = \frac{3.5 \cdot 10^{-3}}{m} .$$

Table 4.5 lists the values of displacement h per unit phase. For m = 1 an h of 3.5 microns is detectable for each degree of phase shift and for m = 19 an h of .18 microns is detectable per degree phase shift. Therefore, based on these estimates for pixel size of the SLM, diameter of the point photodetector, and an m no larger than 19 the smallest h resolvable per degree phase would be 180 nm. However, it is also possible to measure phase shifts of less than a degree with a high performance lock-in amplifier which would improve the resolution limit on h.

4.2.3 Bandwidth

The bandwidth of the coherent processing system will be mainly dependent on the frame rate of the SLM coupled with the response of the lock in amplifier, the required sensitivity (m), and the scan rate of the apparatus used to scan the entire two dimensional moire pattern. If the frame rate of the SLM is f_r and the size of a single pixel is Δ_{SLM}, then the limit on the velocity of the moving fringes v_{SLM} is

$$v_{SLM} < f_r \Delta_{SLM} \quad . \tag{4.2.13}$$

Recall from chapter two that the frequency in radians per second of the scanning fringes is

$$\omega = \frac{8\pi m v \cos\psi}{\rho} \quad .$$

Substituting (4.2.13) into the expression for frequency of the scanning fringes ($v = v_{SLM}$)at the detector,

$$f < \frac{4\, m\, f_r\, \Delta_{CCD} \cos\psi}{\rho} \quad . \tag{4.2.14}$$

Typical SLM's can respond at f_r = 100 frames per second. The fringes will therefore be able to move no faster than 0.7 mm/s. Using the restrictions on ρ and ψ from section 4.2.2 the frequency of the scanning fringes at the detector is

$$f < 200 \bullet m \quad .$$

Therefore, under these assumptions the frequency limit at the detector for the minimal sensitivity requirement where m = 1, is 200 Hz. For the maximum sensitivity requirement where m =19 the frequency limit is 3.8 KHz.

The frequency of the scanning fringes must always be less than 3.8 KHz. The low frequency of this signal from a photodetector will be the limiting factor on the system bandwidth. Typical photodetectors can respond in the nanosecond range and will not hinder the data acquisition. However, realistically the amount of noise from the detector circuit will decrease the bandwidth by forcing the lock-in to filter the low frequency signal with a longer integration time. This being so, the bandwidth of the system will be higher when the system sensitivity is higher or when m is large. Finally, the largest limiting factor will be the apparatus that scans the photodetector over the entire two dimensional moire

fringe pattern.

m	τ_m
1	0.4061
2	0
3	0.0451
4	0
5	0.0162
6	0
7	0.0083
8	0
9	0.0050
10	0
11	0.0034
12	0
13	0.0024
14	0
15	0.0018
16	0
17	0.0014
18	0
19	0.0011
20	0

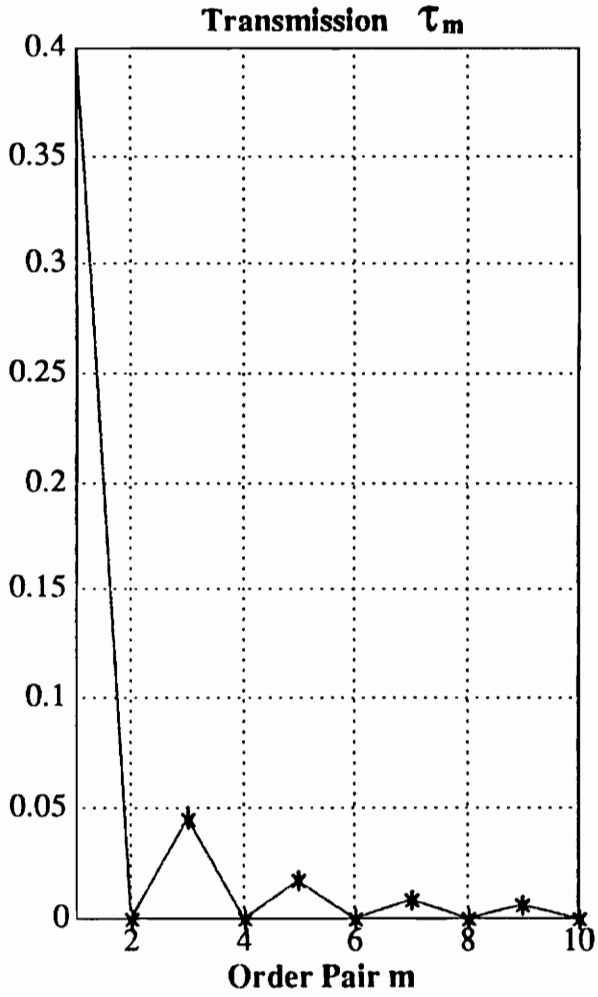

Transmission Coefficients of the mth Order Pair

Figure 4.1

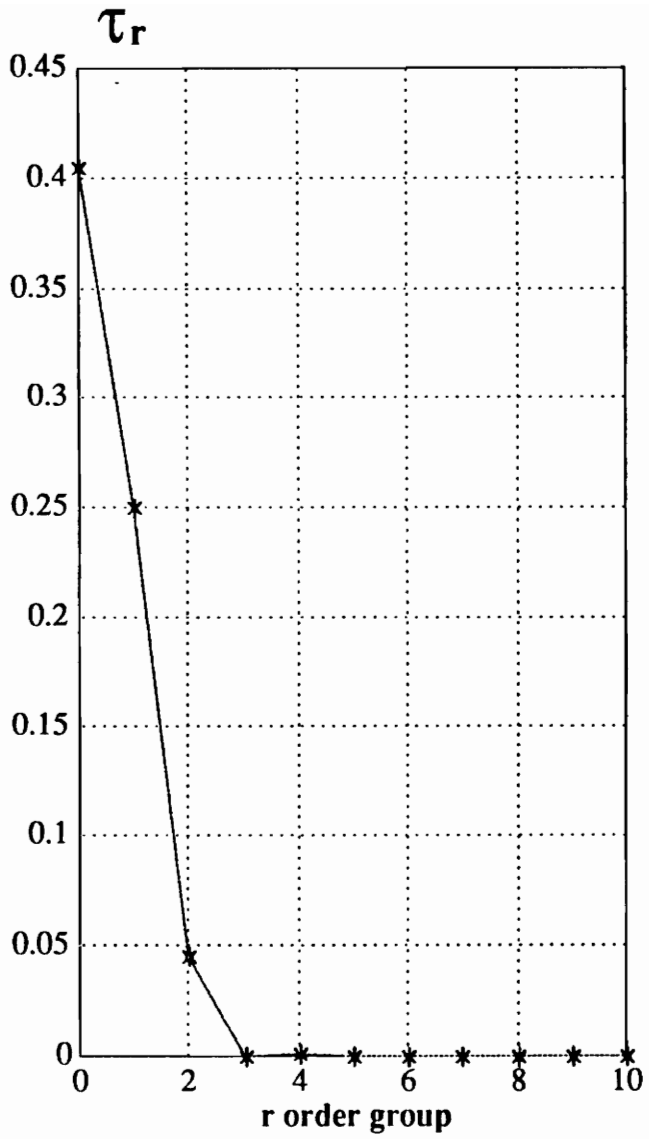

Transmission Coefficients for r Order Groups with m = 1

Figure 4.2

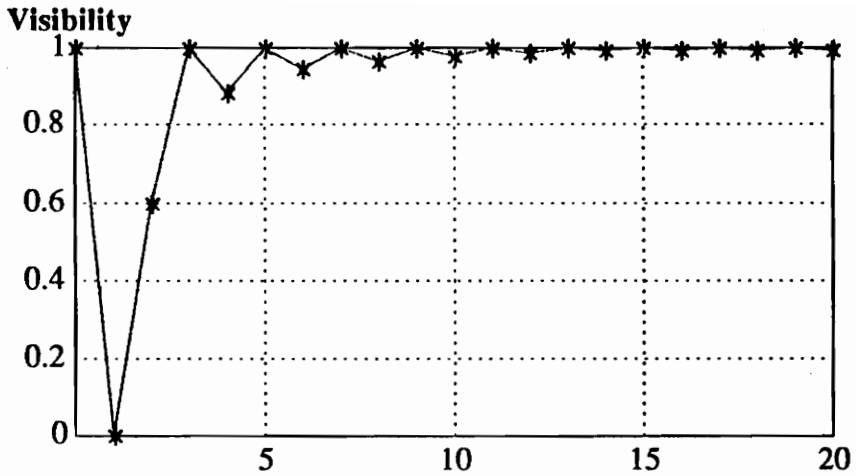

Visibility of Fringes in r Groups for m = 1

Figure 4.3a

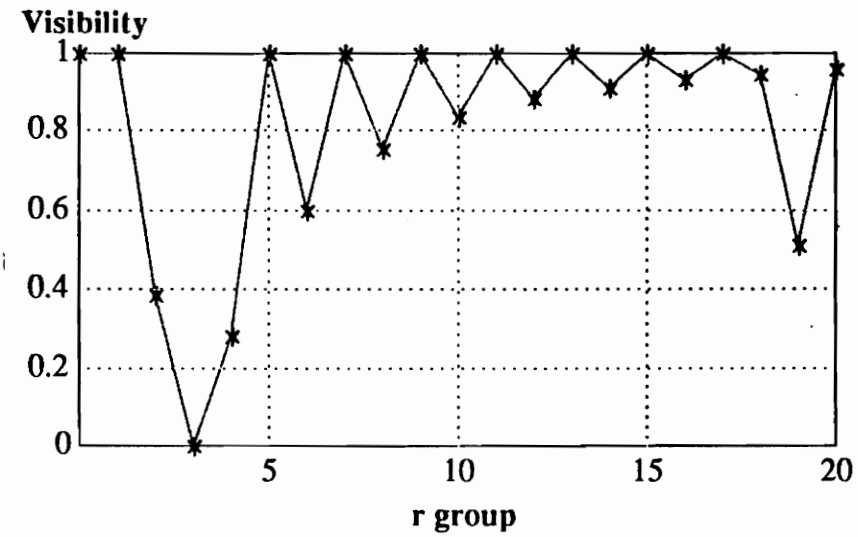

Visibility of Fringes in r Groups for m = 3

Figure 4.3b

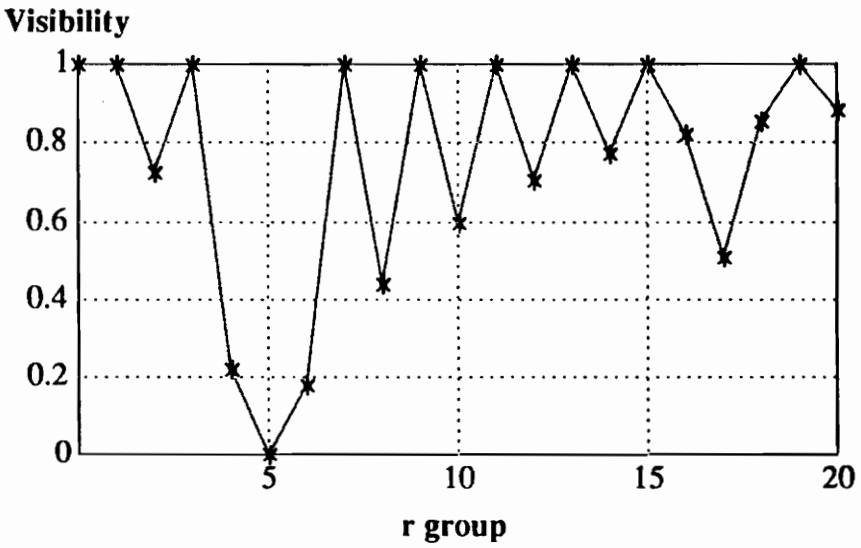

Visibility of Fringes in r Groups for m = 5

Figure 4.3c

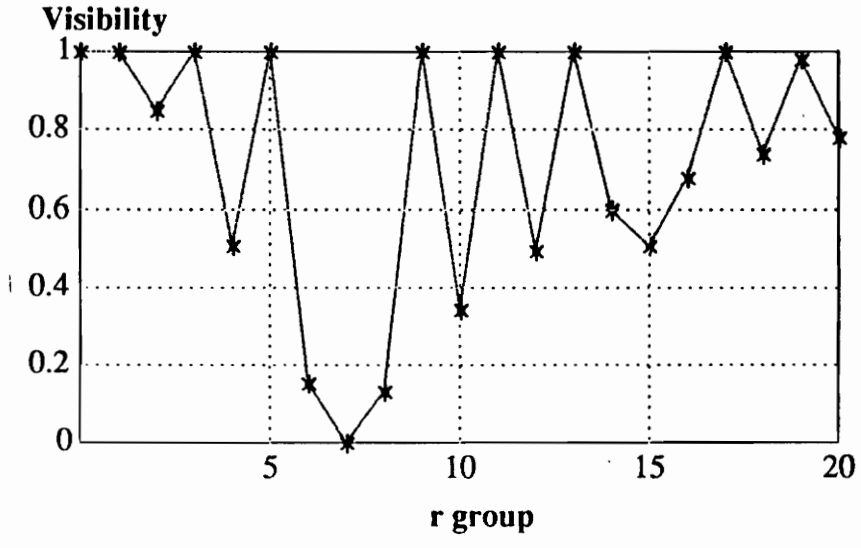

Visibility of Fringes in r Groups for m = 7

Figure 4.3d

Table 4.1

Transmission Coefficients of r Order Groups

m = 1

r	τ_r
0	0.40528478934974
1	0.25000003379130
2	0.04503164326108
3	0
4	0.00180126573044
5	0
6	0.00033084472600
7	0
8	0.00010211256975
9	0
10	0.00004135137122
11	0
12	0.00001981929627
13	0
14	0.00001065837710
15	0
16	0.00000623275339
17	0
18	0.00000388468009
19	0
20	0.00000254574274

Table 4.2

Transmission Coefficients of r Order Groups

m = 3

r	τ_r
0	0.04503169227154
1	0
2	0.14590268295979
3	0.25000030588032
4	0.07444014436724
5	0
6	0.00500352136350
7	0
8	0.00120580729719
9	0
10	0.00044047422703
11	0
12	0.00020014085454
13	0
14	0.00010430858972
15	0
16	0.00005978736045
17	0
18	0.00003676056512
19	0
20	0.00002385886457

Table 4.3

Transmission Coefficients of r Order Groups

m = 5

r	τ_r
0	0.01621144512082
1	0
2	0.02297540408279
3	0
4	0.12508831111741
5	0.25000085955068
6	0.08373680331000
7	0
8	0.00666150769264
9	0
10	0.00180127168009
11	0
12	0.00071549701296
13	0
14	0.00034650501695
15	0
16	0.00018987937259
17	0
18	0.00011333377927
19	0
20	0.00007205086720

Table 4.4a

Transmission Coefficients of m Order Pairs

m	Transmission Coeff τ_m
3	0.04512307258934
5	0.01624430613216
7	0.00828791129192
9	0.00501367473215
11	0.00335626159755
13	0.00240300386570
15	0.00180492290357
17	0.00140521679344
19	0.00112495194821

Table 4.4b

Transmission Coefficients of the r = 0 Order Group

m	Transmission Coeff τ_r
3	0.04503169227154
5	0.01621144512082
7	0.00827117375007
9	0.00500357330231
11	0.00334952041573
13	0.00239819650359
15	0.00180133014777
17	0.00140243724575
19	0.00112274426120

Table 4.5

Sensitivity of h per unit degree for Odd Orders m = 1 to 19

m	h/phase (μm/degree)
1	3.5000
3	1.1667
5	0.7000
7	0.5000
9	0.3889
11	0.3182
13	0.2692
15	0.2333
17	0.2059
19	0.1842

5.0 Experimental Results

The results for the projection moire experiments and the fringe interpolation experiments are presented here. The intensity projection moire experiment is described first. Second, are the results from the electronic phase detection experiment and last the results of the fringe multiplication experiments.

5.1 Intensity Projection Moire

Figure 5.1 shows the experimental set-up for the intensity projection moire sensing scheme. The grating G_A was generated by a Michelson interferometer shown in figure 5.1. G_A was projected on the test surface and monitored through G_B which was a Ronchi grating of spacing 4.0 +/- .014 lp/mm which remained untilted. The Michelson was adjusted to a period $p_o M_A$= 6.5 +/- 1.0 mm measurable on the test surface. The Michelson fringes were tilted by an angle θ = 14 +/- 3 degrees, the magnification M_B (from the surface to G_B) was .035 +/- .001 and the viewing angle ϕ was 28.6 +/- .3 degrees. The magnification from the moire pattern to the CCD photodetector array was M_{CCD} = .63 +/- .04. The height of the projected grating image on the surface was approximately 160 +/- .5 mm and therefore, at the CCD detectors was 3.5 +/- .1 mm in length along the y'' direction. The vernier translation stage was moved in the -z' direction in increments of Δz_o = .635 +/- .0003 mm and after each increment a vertical data scan was recorded.

5.1.1 Data Analysis of Intensity Patterns

Each data set gathered is of a vertical plot of the moire pattern image behind G_B collected by a charge coupled device (CCD) camera and digitized using an eight bit analog to digital converter (figure 5.2). For each displacement of .635 mm a new vertical data scan was collected beginning with the zero position $z_o = 0$ in the first scan (figure 5.2). After all data was collected the Δy fringe shift in the fringes of these scans was determined by averaging over four fringes taken from the center of the patterns.

The processing of the data sets began with low pass filtering each data set. Figure 5.2 is a plot of the first vertical scan with $z_o = 0$ and figure 5.3 is a plot of that same vertical scan low pass filtered by a MATLAB algorithm. The data was then truncated to include only the center four fringes for tracking purposes (figure 5.4). Figure 5.5 shows the simulated sinusoidal fringes that were used to track the average pixel shift of the data scans. Figure 5.6 illustrates the phase difference between the sinusoidal fringe group and the Moire intensity pattern fringe group extracted from the first data set where $z_o = 0$. Figure 5.7 shows the sinusoidal fringes shifted in phase by - 24 pixels such that the phase of the sinusoid matches the average phase of the data fringe group. Figure 5.8 shows the sinusoidal fringe group shifted by -20 pixels to match the average phase of the second data set in which z_o was .635 mm. This technique of shifting the sinusoidal fringe group until it matches the moire pattern was repeated for each data set and the amount in pixels it took to match the sinusoid with the Moire fringe group was noted. The pixel width Δ_{CCD} is 6.60 +/- .005 microns and so the Δy fringe shift in microns is calculated by multiplying the pixel shift determined by the processing method and Δ_{CCD}.

5.1.2 Processing Results

The pitch of the moire pattern at the CCD detectors was calculated to be .6 +/- .3 mm based on the previous values where $p_{moire} = M_C M_B M_A p_o / \sin\theta$. The error of .3 mm is based on the propagation of systematic errors. The experimental value for p_{moire} was p_{moire} = .44 mm +/- .02 mm. The error of .02 mm is an estimated experimental error based on uncertainty associated with the pitch of the sinusoidal pattern that was used to analyze the moire fringes. Based on the measured parameters, the calibration constant of z_o and Δy calculated for this experiment is C = (change in Δy) / Δz_o = $M_{CCD} M_B \sin\phi / \sin\theta$ = .044 +/- .01. The error .01 on C is based on the propagation of systematic errors. For the displacement for Δz_o, the calculated value for change in $\Delta y = \Delta z_o \cdot C$ = 28 +/- 6 microns.

The data is graphed in Figure 5.9 along with the best straight line fit to the data. The slope of the straight line in figure 5.9 is .044 with an unexplained error of +/- .003 microns. The result is within the tolerance on the calculated C specified previously or in the range between .034 and .054 microns and varies by less than the tolerance based on systematic errors. Therefore, based on the results shown in Figure 5.9 the mean Δy was 28.0 +/- 1.8 microns per Δz_o. The experimental value of the calibration constant was $\Delta y / \Delta z_o$ = .044 +/- .003.

5.2 Electronic Phase Detection

Figure 5.10 is the schematic of the electronic phase detection experiment. The source used was a 514 nm wavelength argon laser. The source was filtered, collimated and then

focused by a cylindrical lens into an acousto-optic modulator. The acousto optic modulator was used to project the moving fringes on the test surface which was mounted to a vernier translation stage.

In order to generate a moving grating mask, the modulator requires a carrier frequency of 45 MHz. The light diffracts in to various orders based on the index variations due to the carrier frequency as is emerges from the AO cell. For this reason a single order was passed by a spatial filter in the Fourier plane of the AO cell. Each order contains an image of the a moving grating of a spacing proportional to the modulation frequency F_{mod}. The spacing of the moving grating is determined by the 50 microsecond window and the modulating frequency in the relationship # of fringes /1.2 inches = Fmod * 50 microseconds since the window is 1.2 inches long. For example, using a modulation frequency 100 KHz results in five fringes across the entire window. Therefore the grating is moving at 100 KHz and the pitch of these fringes is about 5.0 mm. The choice for modulation frequency was limited by the frequency response of the other components in the system such as the lock-in amplifier and the photodetector circuit. Therefore, for purposes of collecting data the modulation frequency was set to 55 KHz which yielded a grating pitch of 9.2 +/- .05 mm on the test surface since $M_A = 1$.

The lenses in the system all had focal lengths of 150 mm with the exception of the moire viewer lenses. A second cylindrical lens was used after the modulator to image the moving grating on the test surface. The projected pattern was imaged by the moire viewer on the second grating at a viewing angle of 29.6 +/- 0.4 degrees. The moire pattern was detected behind the second grating by a photodetector where the magnification M_B was .039 +/- .001. The spacing of the second grating G_B was 2.0 +/- .014 lp/mm. The output signal of the detector placed just behind G_B was analyzed by the lock-in amplifier to

determine the phase shift in the moving moire pattern. With the lock-in set to 55 KHz the phase of the moire pattern was monitored by measuring changes in the DC output voltage from the lock-in with an oscilloscope. The DC output of the lock-in amplifier for a range of -1 volt to 1 volt corresponded to phase measurements in the range ($-\pi/4$ to $\pi/4$). A measurement was taken after each increment in z_o of .127 +/- .0003 mm starting at $z_o = 0$.

5.2.1 Data and Results

The relationship between Δz_o and Δphase is $\Delta\text{phase} / \Delta z_o = (2\pi \sin\phi / M_A p_o) = .33$ +/- .003 radians, based on the measured parameters and the error .003 is based on propagation of systematic errors. The prediction on the mean phase shift would be $\Delta\text{phase} = \Delta z_o * .33$ +/- .003 radians. For the known out of plane displacement of .127 mm the average predicted Δphase = .042 +/- .0005 radians based on measured parameters.

Figure 5.11 illustrates the experimental results for the electronic phase detection experiment. The mean slope of the data was .042 radians with a random unexplained error of .03 radians. The experimental calibration constant = .042 +/- .03 radians. Although the mean Δphase was within the predicted tolerance the large unexplained error may have been due to instability of the laser. The projected fringes may have been shifting in time while the measurements were being made.

5.3 Fringe Multiplication

The schematic for the fringe multiplication experiment is in Figure 5.12. The grating G_1 was mounted on a vernier translation stage. The Fourier transform of G_1 was filtered

by F_1 to pass only the m =1 order pair for the first experiment and the m = 3 order pair for the second experiment. The filtered orders were reimaged against G_2. The spacings of both gratings was 10.0 +/- .014 lp/mm. The Fourier transform of G_2 was filtered by F_2 to pass a single r order group. G_1 was tilted angularly until the fringe pattern appeared to have a coarse fringe pattern with vertical fringes. The first grating G_1 was translated in increments of h = 3 +/- 1.0 microns (the vernier stage measured in mils and 1/10 mil had to be roughly estimated) and after each increment a measurement from the detector was recorded. The translation along x of the first grating caused a phase shift in one dimension of the output intensity pattern located at the detector. The magnification of the system was 1:1 and the lenses all had focal lengths of 150 mm.

5.3.1 Experimental Results

Results of the two experiments are shown in Figure 5.13a (experiment one with m = 1) and Figure 5.13b (experiment two with m = 3). To extract the relationship between phase and h from the experimental data, the data was analyzed to determine what Δh was for a 2π phase shift in the moire fringe pattern. Measuring the 2π phase shift of the m = 1 intensity fringe pattern corresponded to a 44 +/- 4 microns translation of h or Δh. The average 2π phase shift for the m = 3 data set corresponded to 15 +/- 2 microns Δh. Therefore, with m = 3, a 2π phase shift results from a Δh 1/3 smaller than the Δh with m = 1. The sensitivity for the system (Δphase/ Δh) using m = 1 was .14 +/- .02 and the sensitivity for the m = 3 system was .40 +/- .05 based on the results approximated for a 2π phase shift. As shown in chapter 3.0, the sensitivity to a translation of h is enhanced by increasing m.

Figure 5.14a shows the two dimensional moire pattern using fringe multiplication for m = 1, and Figure 514b shows the two dimensional image for m = 3. The orientation of these fringes was made vertical for the one dimensional experiments mentioned previously by adjusting the angular alignment of the first grating. The patterns in Figures 5.14a and 5.14b were of the r = 0 order group for both the m =1 and m = 3.

To demonstrate how the visibility of fringes varies with r order group, Figure 5.15a shows the image of the r = -1 order group for m = 1 and 5.15b shows the image of the r = -3 order group for m = 3. Notice that although the pattern in Figure 5.15b is brighter than the pattern in Figure 5.14b (m = 3 for both), the visibility of fringes in 5.15b has decreased by a considerable amount as compared with 5.14b. The visibility of the r = -1 order group with m = 1 in Figure 5.15a is poor compared with the visibility of the r = 0 order group for m = 1. This correlates with the theoretical analysis in Chapter 3.3 that the visibility is best at the r = 0 order groups for all m.

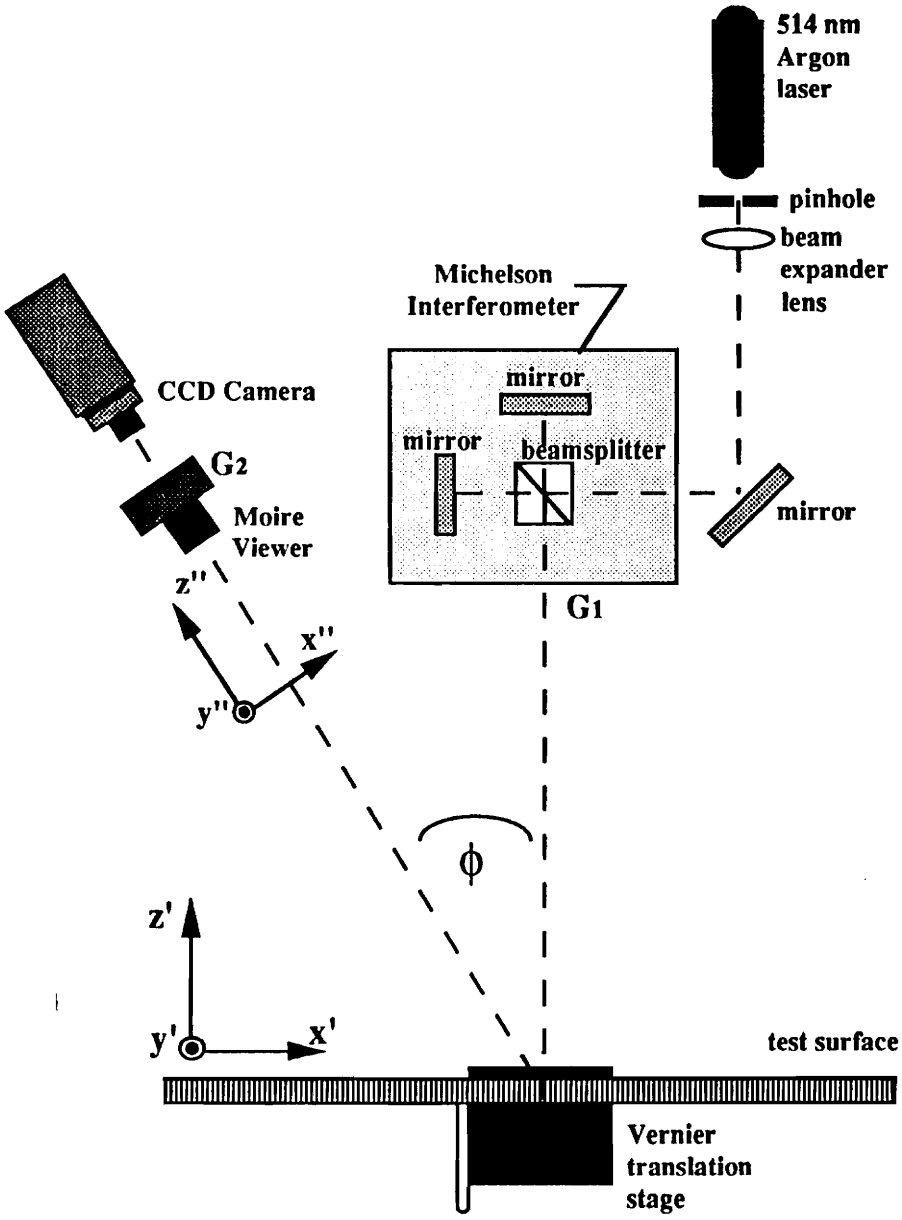

Experimental Set-up for Intensity Projection Moire

Figure 5.1

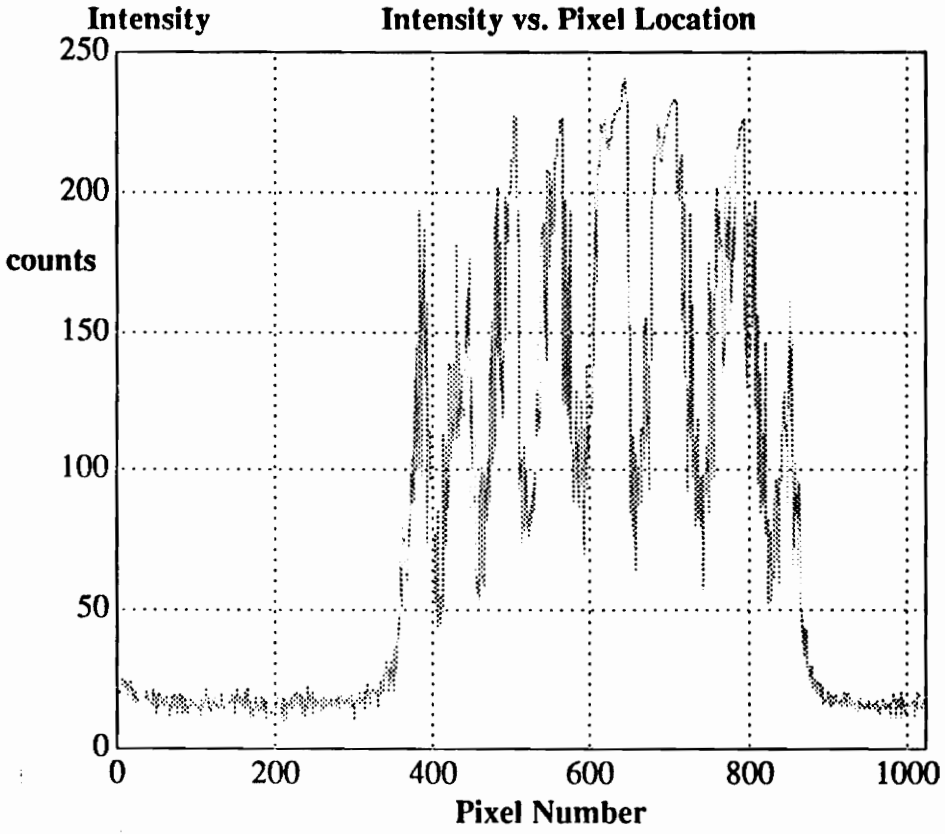

Unfiltered Data of Moire Vertical Intensity Plot for $z_o = 0$

Figure 5.2

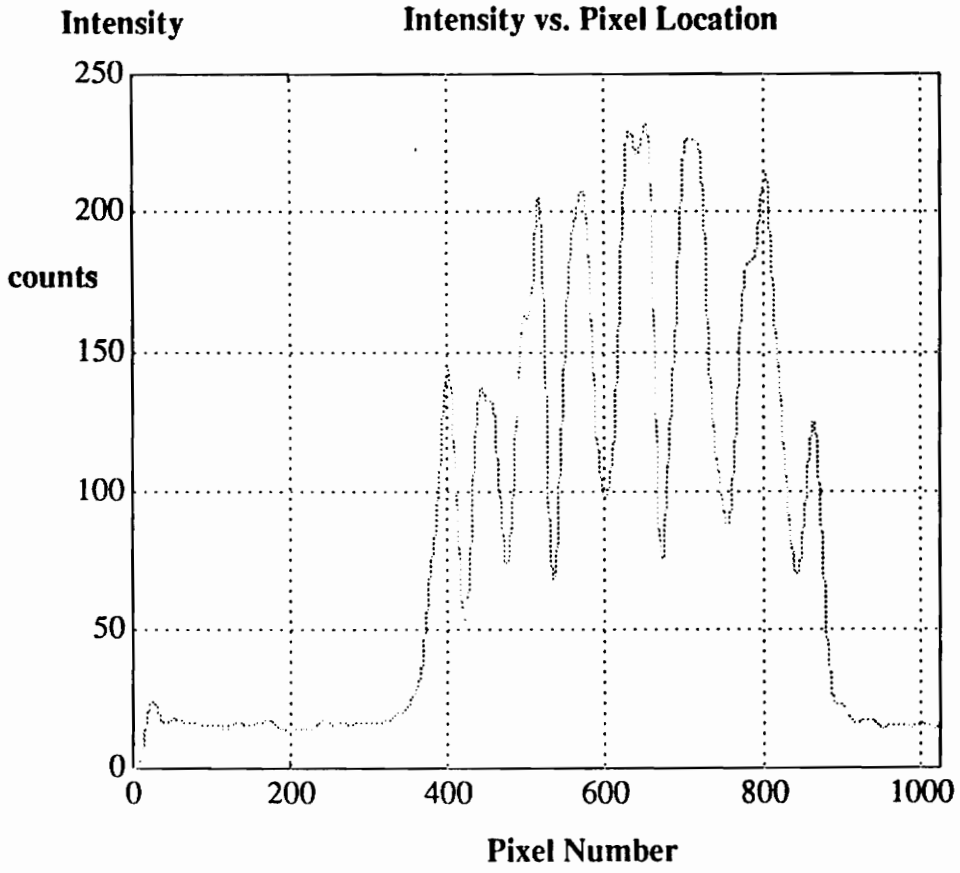

Filtered Data of Moire Vertical Intensity Plot for $z_o = 0$

Figure 5.3

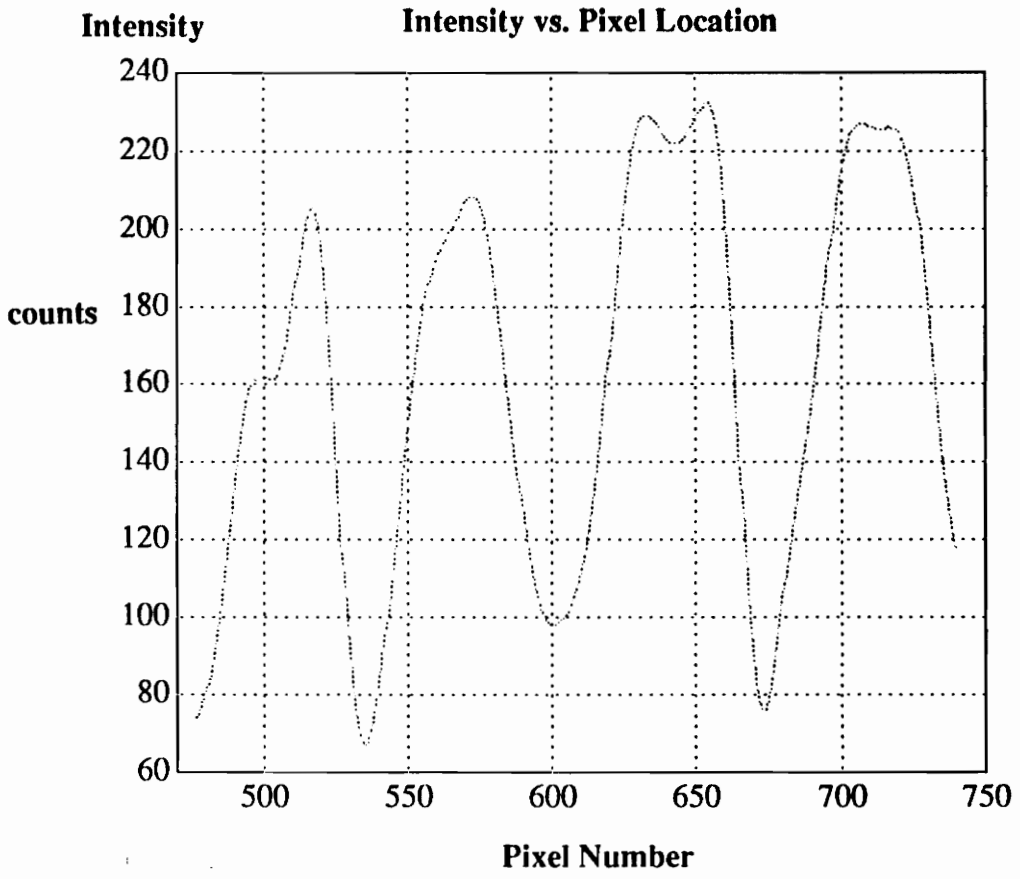

Center Four Fringes from theMoire Intensity Pattern with $z_o = 0$

Figure 5.4

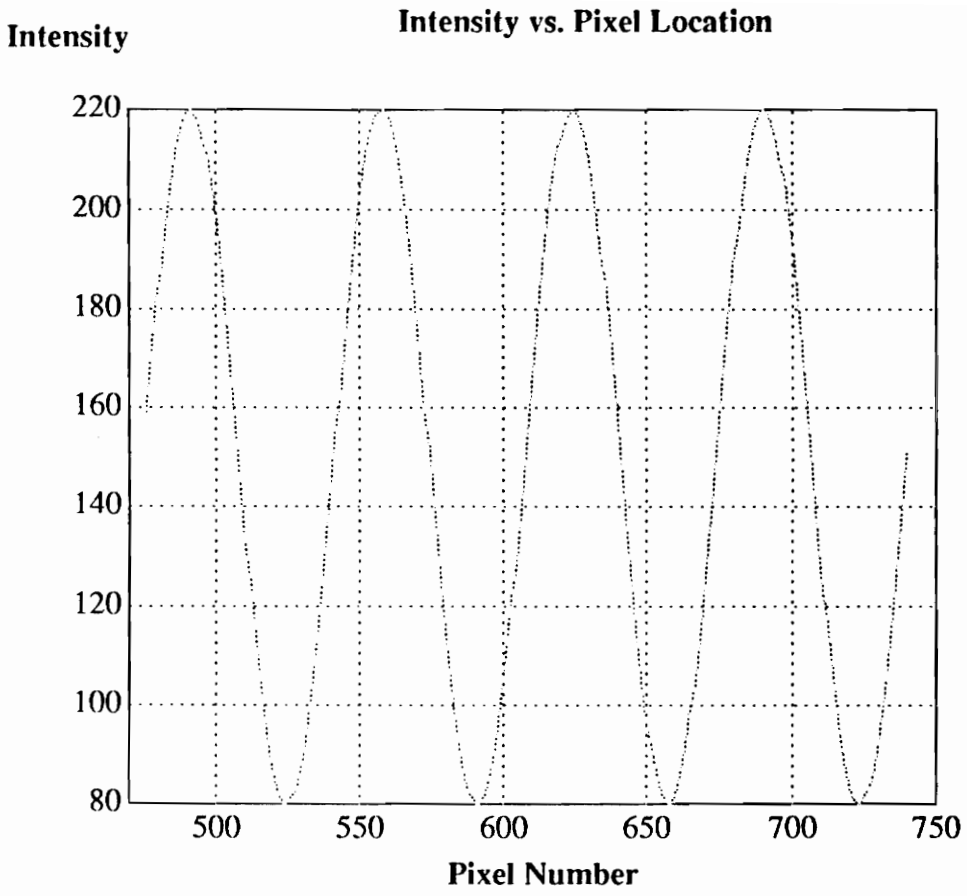

$$y = 150 + 70 \sin\left\{\frac{2\pi}{66.2}(x + \text{phase offset})\right\}$$

where $476 \leq x \leq 740$

Simulated Sinusoidal Fringe Pattern to Average Moire Fringe Group Position

Figure 5.5

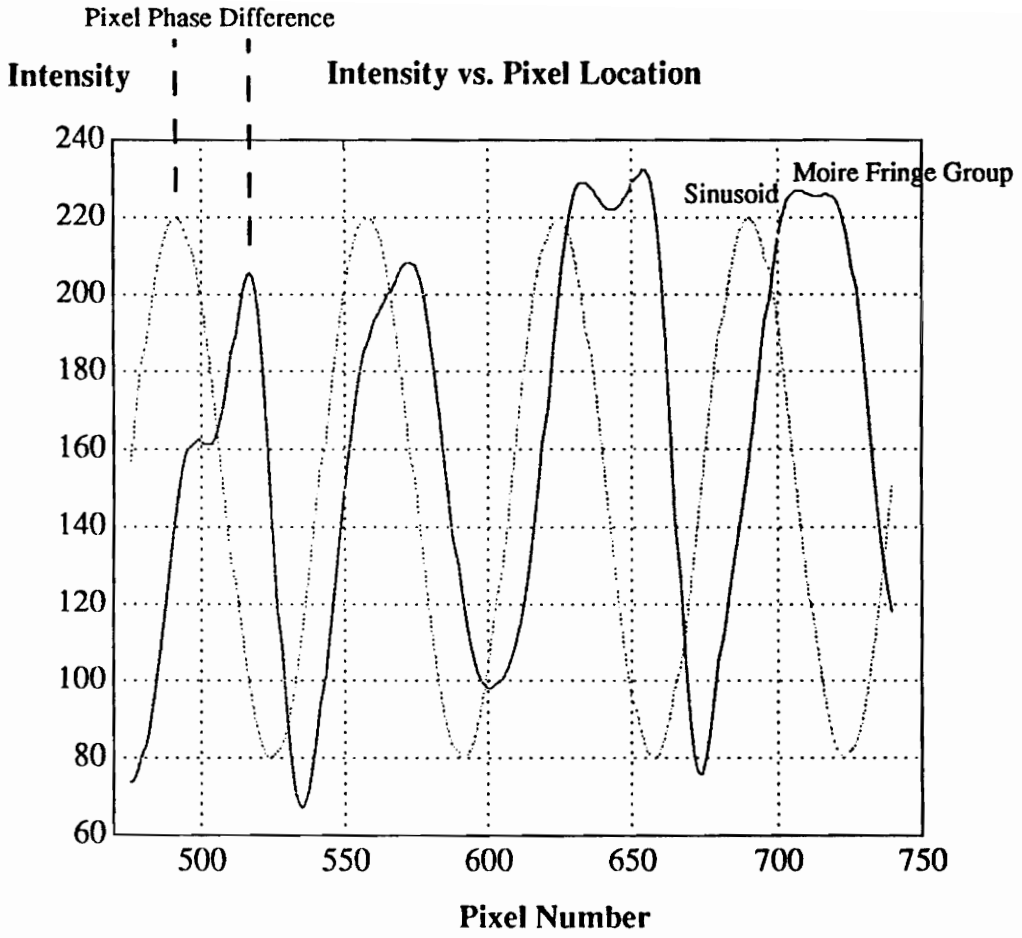

Out of Phase Sinusoidal Pattern and Moire Fringe Group $z_o = 0$

Figure 5.6

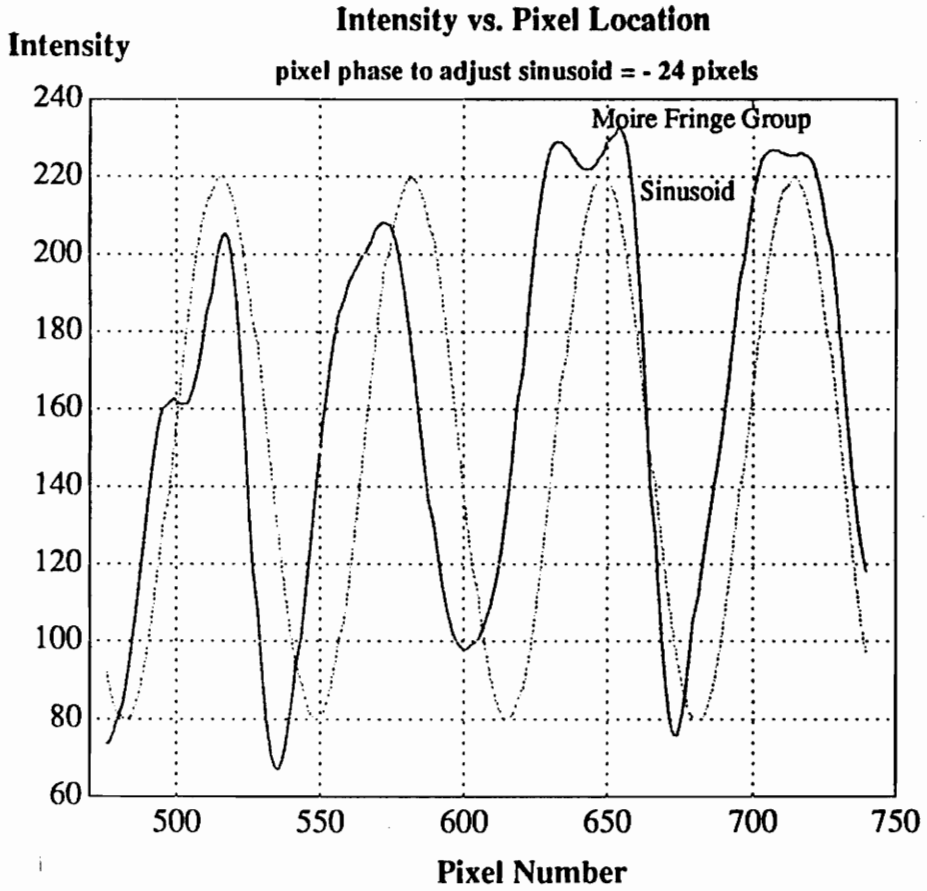

Sinusoidal Pattern and Moire Fringe Group $z_o = 0$, In Phase

Figure 5.7

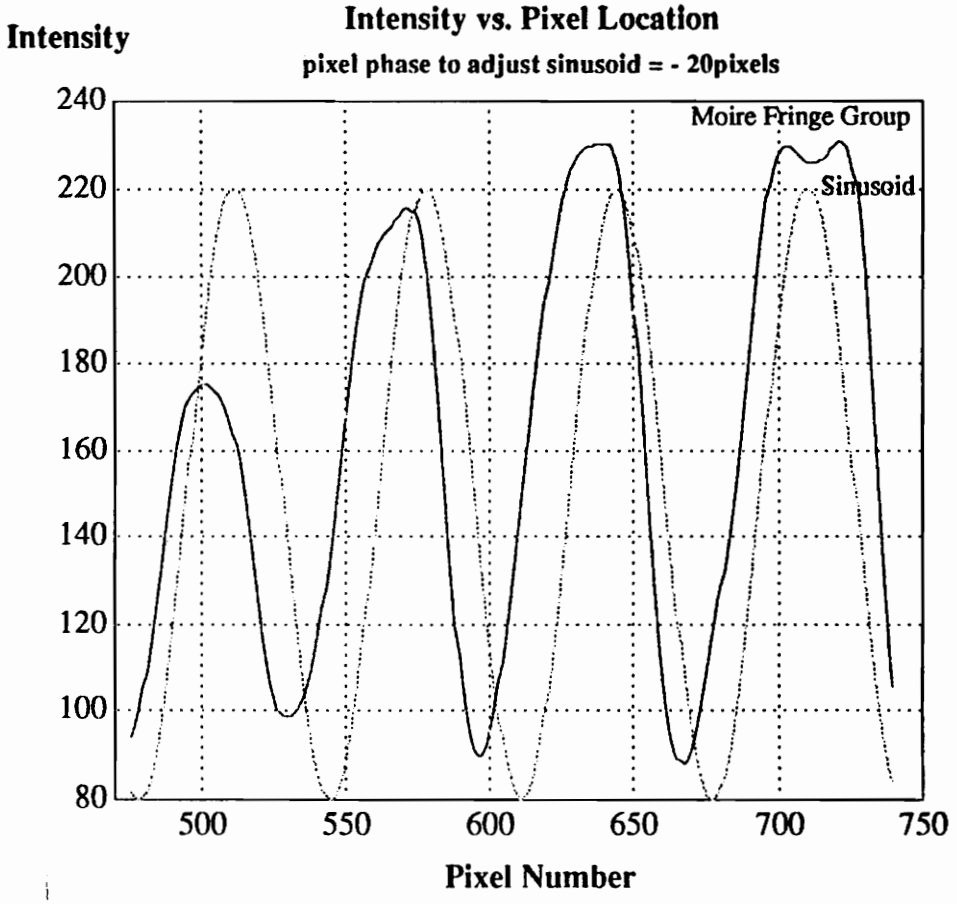

Sinusoidal Pattern and Moire Fringe Group z_o = .635 mm, In Phase

Figure 5.8

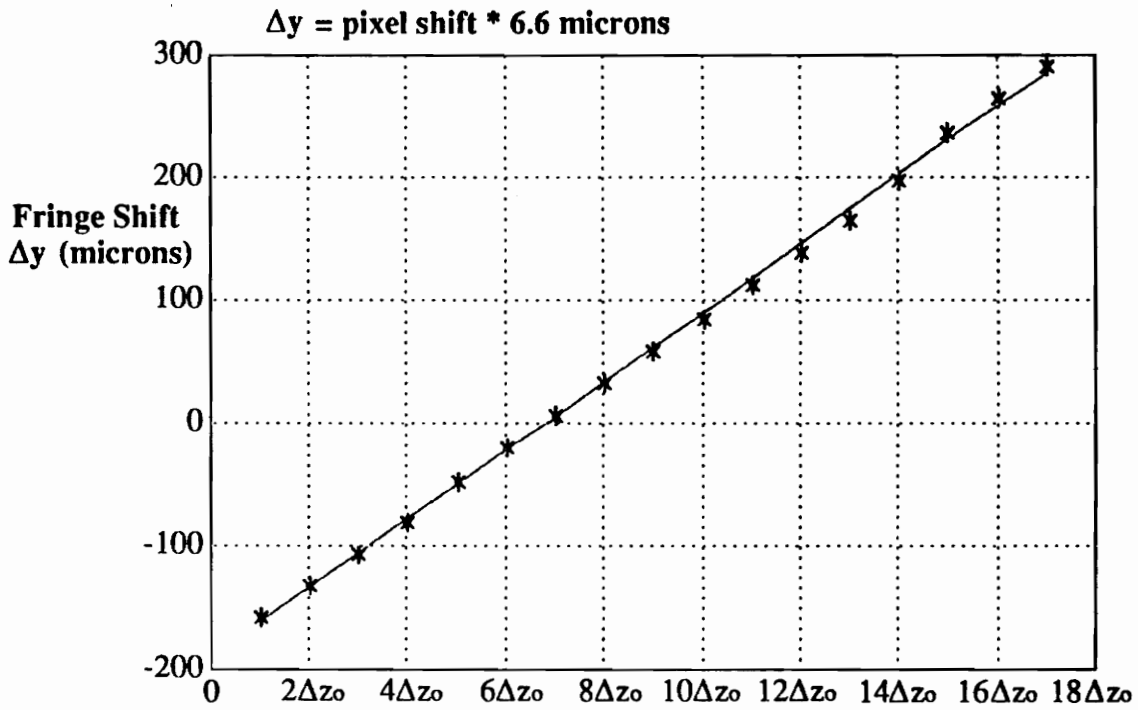

$$\text{slope} = \frac{28}{\Delta z_0}$$

$$\text{Root Mean Square Regression} = \frac{1.8}{\Delta z_0}$$
(standard deviation)

For known $\Delta z_0 = 635 \pm .3\ \mu m$

Calibration Constant = .044 +/- .003

Experimental Data for Intensity Projection Moire
(with a Linear Fit)

Figure 5.9

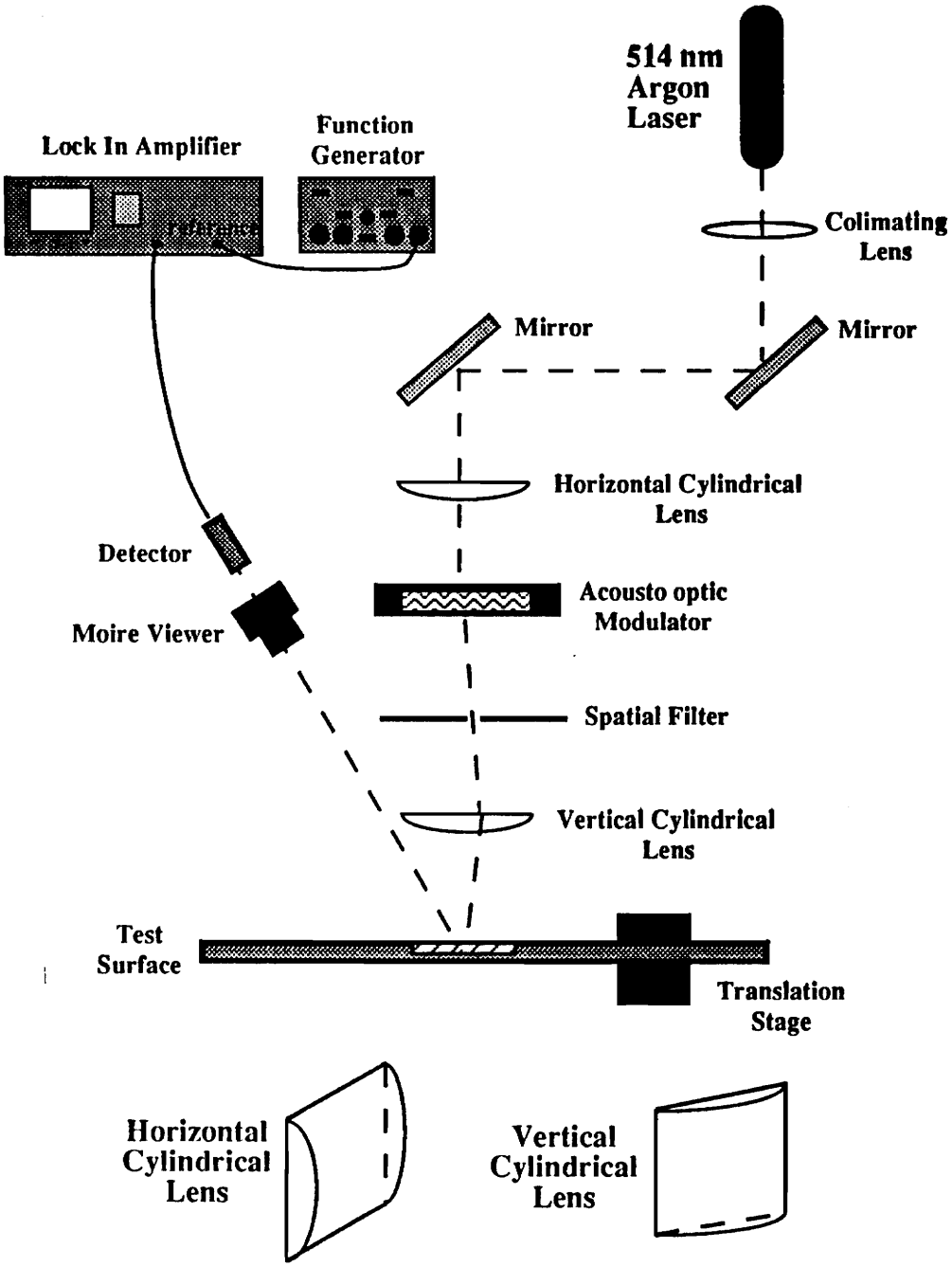

Experimental Set-up For Phase Detection

Figure 5.10

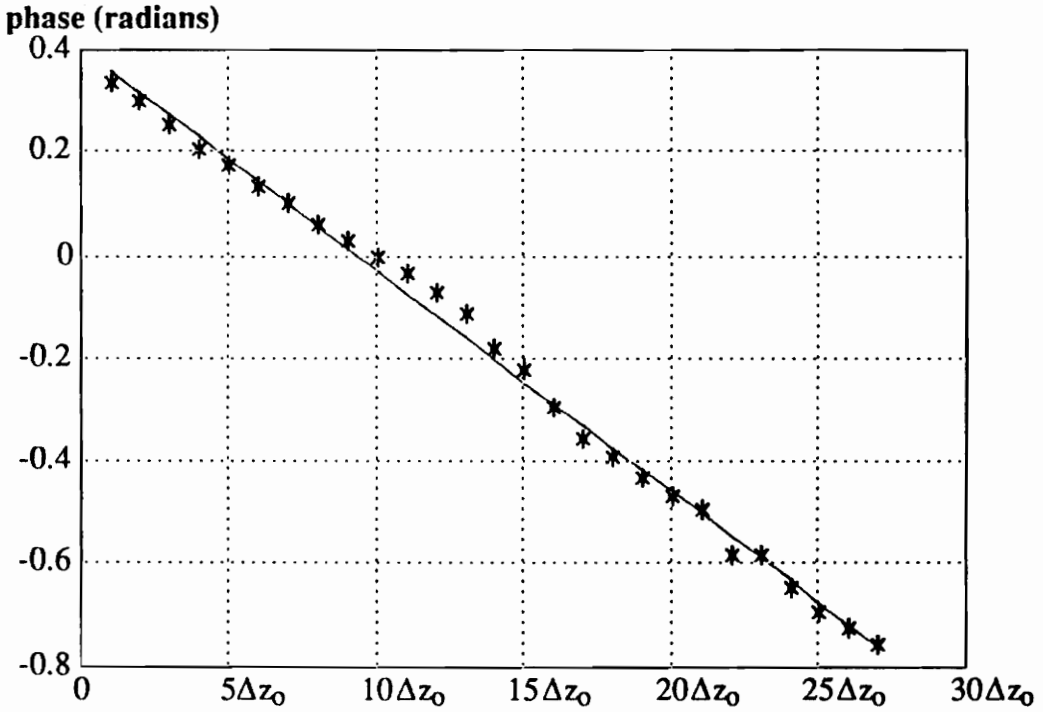

$$\text{slope} = \frac{.042}{\Delta z_0} \text{ radians / mm}$$

$$\text{Root Mean Square Regression (standard deviation)} = \frac{.03}{\Delta z_0} \text{ radians / mm}$$

for known $\Delta z_0 = 127\ \mu m$ +/- .3

Calibration Constant = .33 +/- .03 radians / mm

Electronic Phase Detection Experimental Data with Linear Fit

Figure 5.11

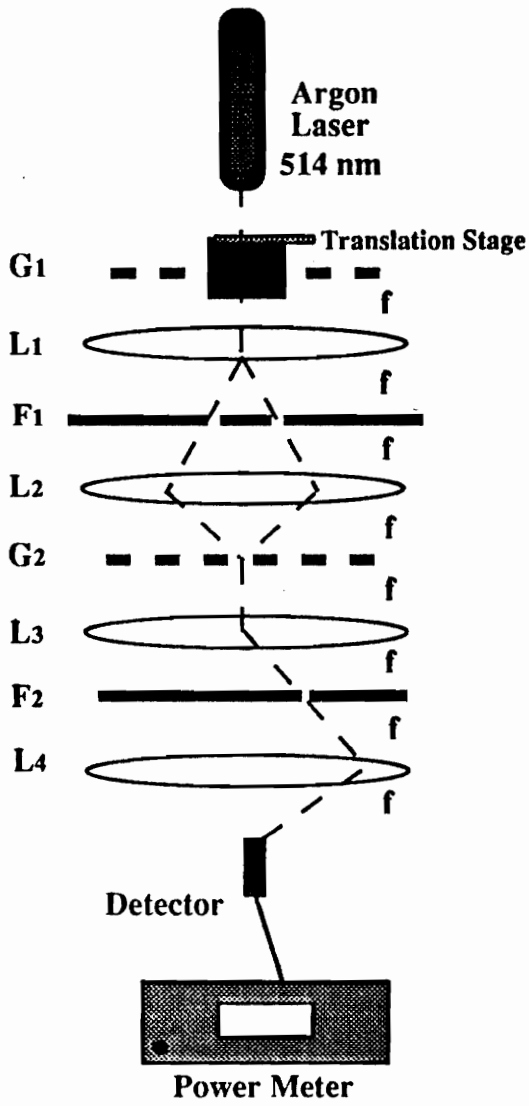

Experimental Set-up for Fringe Multiplication

Figure 5.12

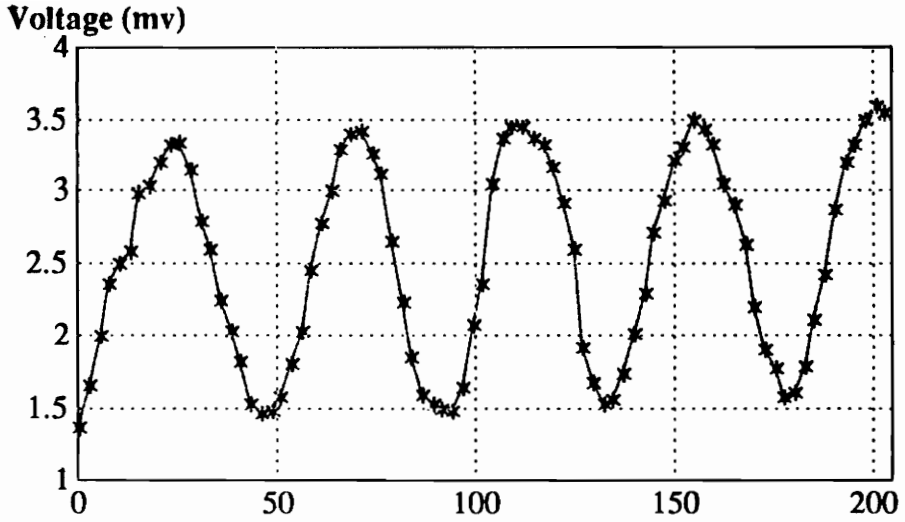

Translation h, (microns)
increments of 3 microns
Experimental Data for Fringe Multiplication
With Grating Frequency 10 lp/mm and m = 1
Figure 5.13a

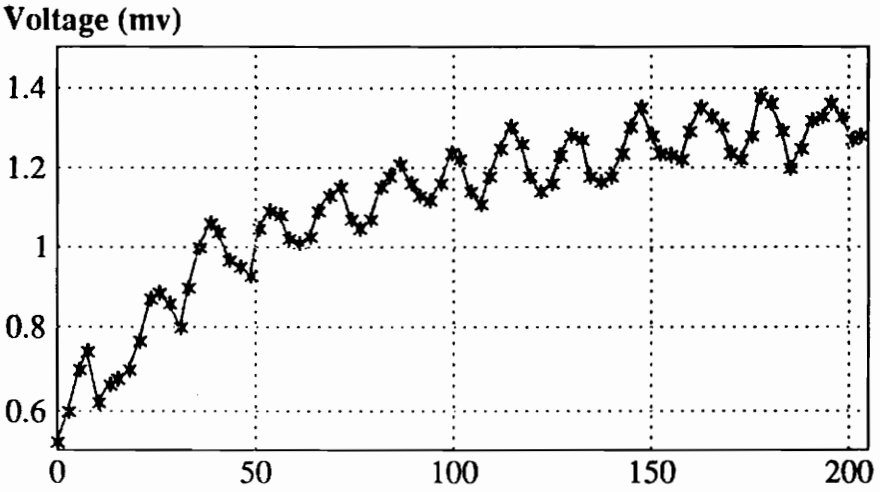

Translation h, (microns)
increments of 3 microns
Experimental Data for Fringe Multiplication
With Grating Frequency 10 lp/mm and m = 3
Figure 5.13b

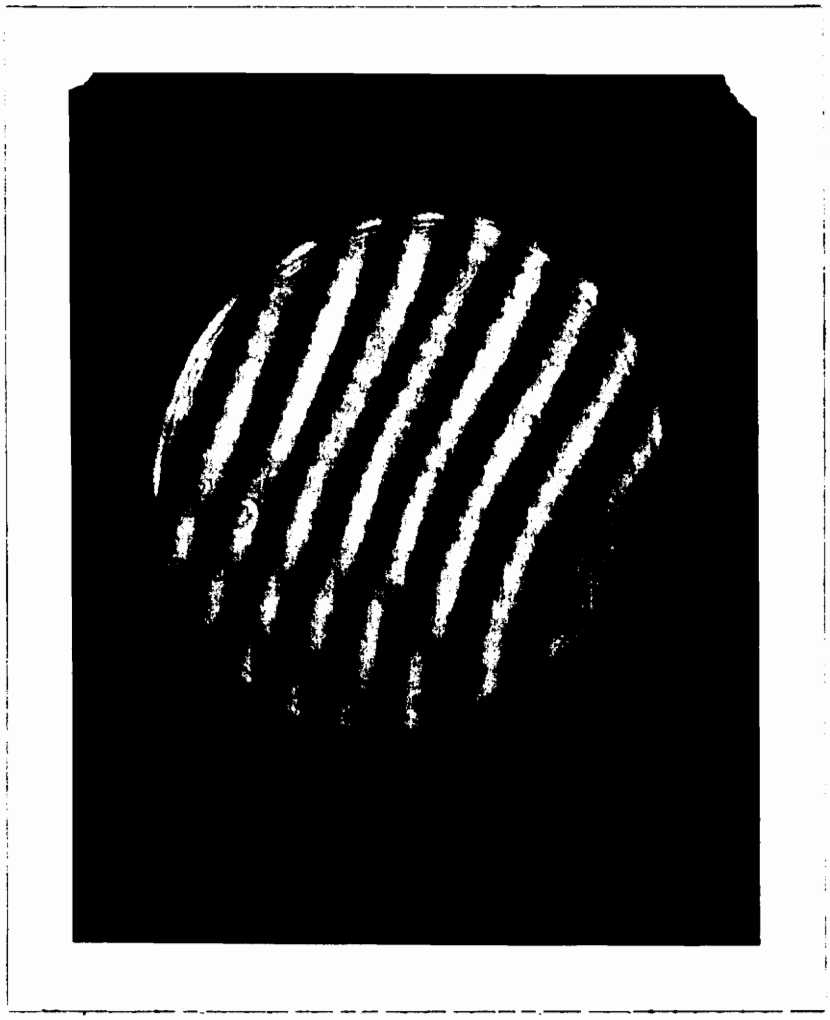

Figure 5.14a
Moire Pattern Using Fringe Multiplication
of r group = 0 and m order pair = 1

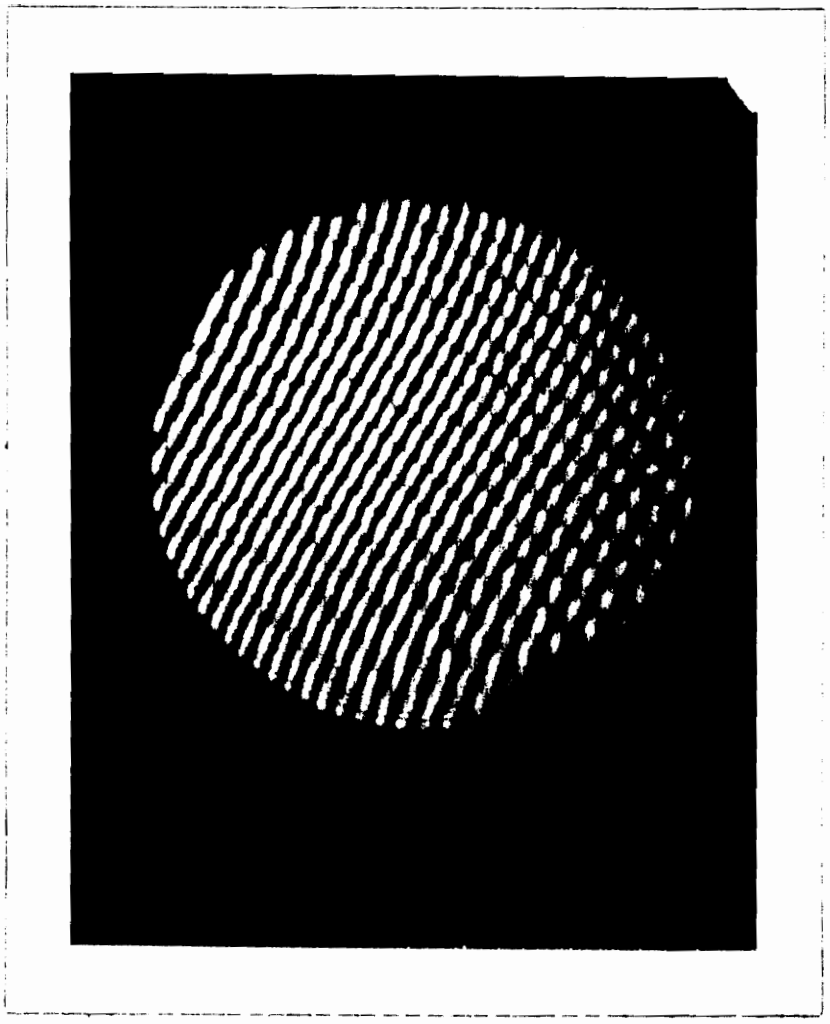

Figure 5.14b
Moire Pattern Using Fringe Multiplication
of r group = 0 and m order pair = 3

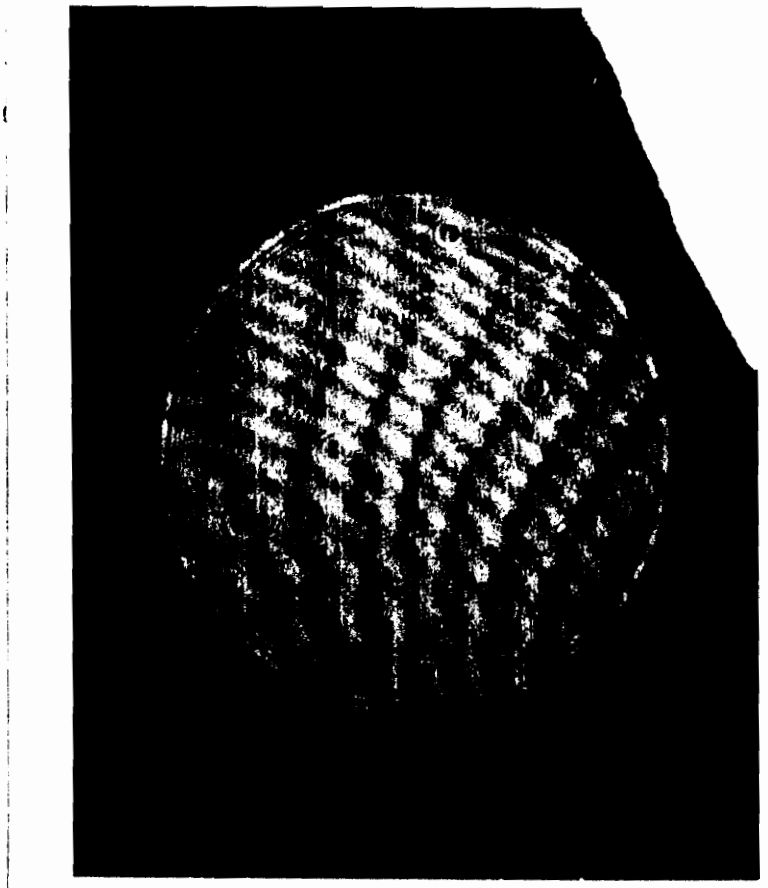

Figure 5.15a
Moire Pattern Using Fringe Multiplication
of r group = -1 and m order pair = 1

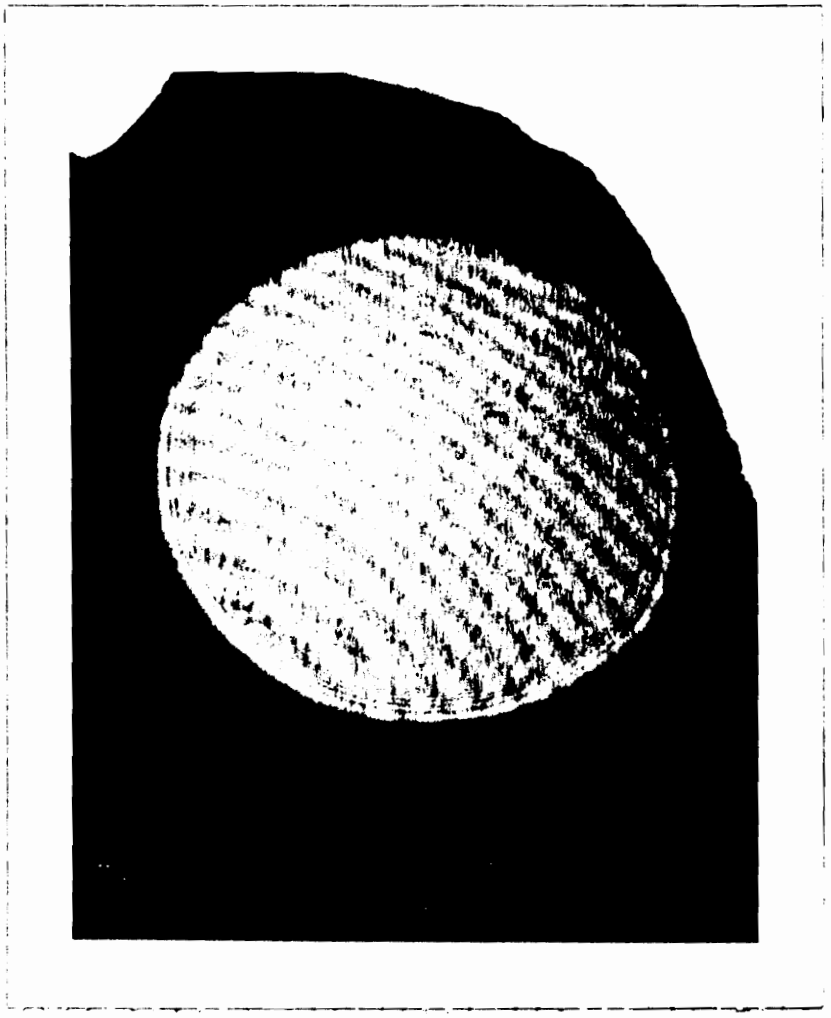

Figure 5.15b
Moire Pattern Using Fringe Multiplication
of r group = -3 and m order pair = 3

6.0 Conclusions

Demonstrated in this paper were the components of an incoherent projection moire system with coherent processing for contour sensing of large flexible structures. The theory of each component was explained and experimental results presented.

The first component was the incoherent projection moire system in which a grating was projected on to a test surface and imaged on to a second grating positioned at an oblique angle to the optic axis. The result of imaging the projected grating against the second grating is an interference moire fringe pattern. The objective was to measure out of plane displacements of a diffuse test surface. The out of plane displacements of a test surface resulted in a phase shift of the intensity fringe pattern. The system sensitivity to such displacements was determined to have dependence on the pitch of the gratings used to form the moire fringes, the angular misalignment between the two gratings, and the viewing angle of the detection system. The experimental results and theoretical analysis of the intensity based measurement showed that the system could measure out of plane displacement of a large diffuse surface but had low sensitivity at large magnifications and poor accuracy. The conclusion was that the system could adequately provide intensity based information about the surface displacement. To remedy the limiting factors, the incoherent moire pattern could be converted to a coherent pattern, processed and then interpreted using a frequency based sensing scheme.

Coherent processing techniques in conjunction with a frequency based technique was discussed as the solution for raising the sensitivity of the system and quantizing the results. The incoherent moire image would be transduced to a coherent image. Once the moire pattern was in a coherent form the fringes could be interpolated by fringe multiplication and

quantized using electronic phase detection. Using the two methods together results in a coherent processing system with an adjustable sensitivity to test surface displacements.

It was explained through theory and verified with experiments that the fringe pattern can be filtered to enhance the system sensitivity using a method called fringe mulitplication. It was discussed and demonstrated that by passing different diffraction order pairs from the coherent moire pattern through to a second grating that different sensitivities could be achieved. It was also demonstrated that by scanning the fringe pattern in time that the phase shift of the moire pattern could be quantized as well as sensitivity enhanced using a method called electronic phase detection. The overall conclusion is that by coupling the intensity based incoherent projection moire system with the coherent processing technique of fringe multiplication and using electronic phase detection to make a frequency based measurement, that out of plane displacements of large diffuse surfaces can be measured quantitativly with adjustable sensitivity.

7.0 References

[1] Phillips, D. J., Hyland D. C., Collins Jr., E. G., "Experimental Demonstration of Active Vibration Control For Flexible Structures," Proceedings of the 29th Conference on Decision and Control, December 1990.

[2] Mason, B., Hogg, D., Measures, R. M., "Fiber Optic Strain Sensing For Smart Adaptive Structures," Proceedings of the European Conference on Smart Structures and Materials, Glasgow 1992.

[3] Shaikh, N., Chen, S., Lu, Y., Timm, D., "Smart Structural Composites with the Ability to Monitor Vibration and Damage," Proceedings of the European Conference on Smart Structures and Materials, Glasgow 1992.

[4] Schoess, J. N., Sullivan, C. T., "Conformal Acoutic Waveguide Technology For Smart Aerospace Structures," Proceedings of the European Conference on Smart Structures and Materials, Glasgow 1992.

[5] Rogers, C. A., Stutzman W. L., "Large Deployable Antenna Program, Phase I: Technology Assessment and Mission Architecture," NASA contract report 4410, October 1991.

[6] Chanan, G. A., Nelson, J. E., Mast, T. S., "Segment Alignment for the Keck Telescople Primary Mirror," *Advanced Technology Optical Telescopes III*, SPIE Vol. 628, 1986, pp. 466 - 470.

[7] Madec, P-Y., Sechaud, M., Rousset, G., Michau, V., Fontanella, J-C., "Optical Adaptive Systems: recent results at ONERA," Office National D'Etudes et de Recherches Aerospatiales, B.P. 72-92322 Chatillon- France.

[8] Goad, L., Roddler, F., Beckers, J., Eisenhardt, P., "National Optical Astronomy Observatories (NOAO) IR Adaptive Optics Program III: criteria for the wavefront sensor selection," *Advanced Technology Optical Telescopes III*, SPIE Vol. 628, 1986, pp. 305 - 313.

[9] Merkle, F., "Real-Time Wavefront Sensing and Adaptive Optics," *Diffraction-Limited Imaging with Very Large Telescopes*, 237-248, 1989.

[10] Peters, W. N., Arnold, R. A., Gowrinathan, S., "Stellar Interferometer for Figure Sensing of Orbiting Astronomical Telescopes," *Applied Optics* Vol. 13, No. 8, August 1974, pp. 1785 -1795.

[11] Rayleigh, Lord, "On Manufacture and Theory of Diffraction Gratings," Philos. Magazine, series 4, Vol. 47, No.310, February 1874, pp. 81-93. Reprinted in SPIE Milestone Series "Optical Moire and Applications, editors: Indebetouw, G. and Czarnek, R., Vol MS64.

[12] Weller, R., Shepard, B.M., "Displacement Measurement by Mechanical Interferometry," Experimental Stress Analysis, Vol 6, No. 1, 1948, pp. 35 - 38. Reprinted in SPIE Milestone Series "Optical Moire and Applications, editors: Indebetouw, G. and Czarnek, R., Vol MS64.

[13] Dykes, B. C., "Analysis of Displacements in Large Plates by the Grid-Shadow Moire Technique," Paper 14, Experimental Stress Analysis, 1970, pp. 125 - 134.

[14] Takasaki, H., "Moire Topography," Applied Optics, Vol. 9, No. 6, June 1970.

[15] Duffy, D., "Measurement of Surface Displacement Normal to the Line of Sight," Experimental Mechanics, September 1974, pp. 378-384.

[16] Robinson, D. W., "Automatic fringe analysis with a computer image-processing system," Applied Optics, Vol. 22, No. 14, July 15 1983, pp 2169 - 2176.

[17] Sciammarella, C. A., Lurowist, N., "Multiplication and Interpolation of Moire Fringe Orders by Purely Optical Techniques," Optical Moire and Applications, Indebetouw, G., Czarnek, R. editors, SPIE Milestone series, Vol. MS 64, 1992, pp. 210 - 215.

[18] Post, D., "Sharpening and Multiplication of Moire Fringes," *Experimental Mechanics*, April 1967, pp. 154 -159.

[19] Post, D. "Analysis of Moire Fringe Multiplication Phenomena," *Applied Optics*, Vol. 6, No. 11, November 1967, pp. 1938 - 1942.

[20] Indebetouw, G., "Profile measurement using projection of running fringes," Applied Optics Vol. 17, No. 8, September 15, 1978, pp 2930 - 2933.

[21] Stricker, J., "Moire deflectometry with deferred electronic heterodyne readout," Applied Optics, Vol. 24, No. 15, August 1 1985, pp. 2298 - 2299.

[22] Stricker, J., "Electronic heterodyne readout of fringes in moire deflectometry," Optics Letters, Vol. 10, No. 6, June 1985, pp. 247 - 249.

[23] Blatt, J. H., Hooker, J. A., Chang Ho, H.- C., Young, E. H., "Application of acousto-optic cells and video processing to achieve signal-to-noise improvements in variable resolution moire profilometry," Optical Engineering, Vol. 31, No. 10, October 1992, pp. 2129 - 2138.

[24] McGlone, J. C., "Chapter 4, Analytic Data-Reduction Schemes in Non-Topographic Photogrammetry," *Non-Topographic Photogrammetry and Remote Sensing, second ed,* editor: Karara, H.M., American Society for Photogrammetry, pp 37-43.

[25] Jenkins, F. A., White, H. E., "Section 13.8 Division of Amplitude. Michelson Interferometer," *Fundamentals of Optics*, fourth edition, McGraw-Hill, 1976.

Appendix A

Derivation of the 3-D Rotation Matrix

The 3x3 orthogonal rotation matrix is the transformation matrix used to express the coordinates of one coordinate system in terms of another system. Both systems are right-handed and Cartesian. The method for deriving the rotation matrix is found in reference [24] where the process is divided into three steps. Each step involves derivation of a matrix that is orthogonal to the other two relating one coordinate system to the other. Each of these matricies focuses on rotation about one axis at a time in the sequential order x,y and z respectively. For example, the first matrix is denoted as M_γ and is the three dimensional relationship between two coordinate systems when one has been rotated about the x axis by an angle γ. When all three of the matrices have been derived the multiplication of these three matrices in the same sequential order yields the total three dimensional rotation matrix.

The three positive orthogonal axes are defined by illustration in figure A1. The first matrix is determined by rotation about the x axis (figure A2) where the y' and z' axes have been rotated by γ from the y and z axes. The relationship between the x', y', z' axes and the x, y, z axes is

$$\begin{aligned} x' &= x \\ y' &= y\cos\gamma - z\sin\gamma \\ z' &= y\sin\gamma + z\cos\gamma \ , \end{aligned} \tag{A.1}$$

where γ is the angle made by rotating axes y, z to y',z' around the x axis. The rotation matrix for rotation about the x axis is

$$M_\gamma = \begin{bmatrix} 1 & 0 & 0 \\ 0 & \cos\gamma & -\sin\gamma \\ 0 & \sin\gamma & \cos\gamma \end{bmatrix} \tag{A.2}$$

The relationships are found in the same way for the rotation about the y axis where x, z are rotated around y to x', z' making an angle φ (figure A3). The rotation matrix about y is

$$M_\varphi = \begin{bmatrix} \cos\varphi & 0 & \sin\varphi \\ 0 & 1 & 0 \\ -\sin\varphi & 0 & \cos\varphi \end{bmatrix} . \tag{A.3}$$

Finally, the matrix found from rotation of coordinates about the z axis (figure A4) is

$$M_\kappa = \begin{bmatrix} \cos\kappa & -\sin\kappa & 0 \\ \sin\kappa & \cos\kappa & 0 \\ 0 & 0 & 1 \end{bmatrix} , \tag{A.4}$$

where M_κ describes the relationship between the x, y and the x', y' axes when rotated about the z axis by an angle κ. The entire three dimensional rotation matrix is found by multiplying the three individual matrices for sequential rotations about the x, y and finally z axis or

$$M_{rot} = M_\gamma M_\varphi M_\kappa . \tag{A.5}$$

The expression for the total rotation matrix is

$$M_{rot} = \begin{bmatrix} m_{11} & m_{12} & m_{13} \\ m_{21} & m_{22} & m_{23} \\ m_{31} & m_{32} & m_{33} \end{bmatrix} \tag{A.6}$$

where

$$\begin{aligned} m_{11} &= \cos\varphi \cos\kappa \\ m_{12} &= -\cos\varphi \sin\kappa \\ m_{13} &= \sin\varphi \\ m_{21} &= \cos\gamma \sin\kappa + \sin\gamma \sin\varphi \cos\kappa \\ m_{22} &= \cos\gamma \cos\kappa - \sin\gamma \sin\varphi \sin\kappa \\ m_{23} &= -\sin\gamma \cos\varphi \\ m_{31} &= \sin\gamma \sin\kappa - \cos\gamma \sin\varphi \cos\kappa \end{aligned}$$

$$m_{32} = \sin\gamma\cos\kappa + \cos\gamma\sin\varphi\sin\kappa$$
$$m_{33} = \cos\gamma\cos\varphi \qquad (A.7)$$

Therefore to determine a new coordinate system x', y', z' in terms of the old coordinate system x, y, z, the relationship is

$$\begin{bmatrix} x' \\ y' \\ z' \end{bmatrix} = M_{rot} \begin{bmatrix} x \\ y \\ z \end{bmatrix} \qquad (A.8)$$

To express the old coordinate system in terms of the new coordinate system the relationship is

$$\begin{bmatrix} x \\ y \\ z \end{bmatrix} = M_{rot}^{-1} \begin{bmatrix} x' \\ y' \\ z' \end{bmatrix} \qquad (A.9)$$

This implies that rotating from old coordinate system x, y, z, to new coordinate system x', y', z', requires an angular rotation about x of γ, an angular rotation around y of φ and finally an angular rotation about z of κ with all positive rotations in the right hand direction. Extending this to the experimental set-up of figure 2.1, the assumption is that the gratings are in the x, y plane and therefore $\gamma = 0$ and $\varphi = 0$ for any rotation about z only. However, when considering the detection position of the moire projection system, the detector is placed at an oblique angle to optical axis z as defined in figure 2.1. This angle φ is defined by the system and used for tranforming from the coordinates of the surface Σ to the coordinates of the detection plane at G_A. Therefore, the gratings themselves are rotated around the z axis to attain a angular misalignment where κ = constant and the system detector is rotated about the y axis , φ = constant, to alter the phase and frequency of the projected grating on the surface Σ.

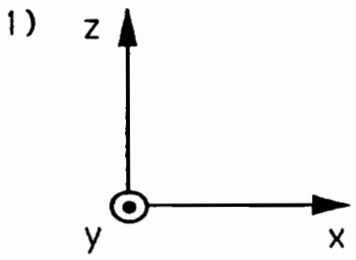

definition of positive axes

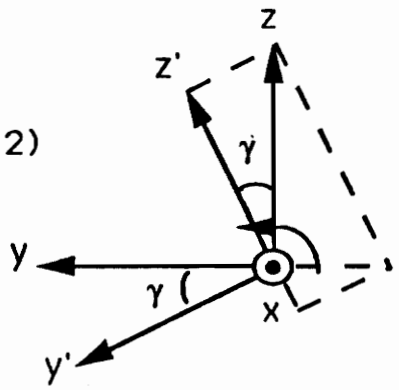

rotation around the x axis

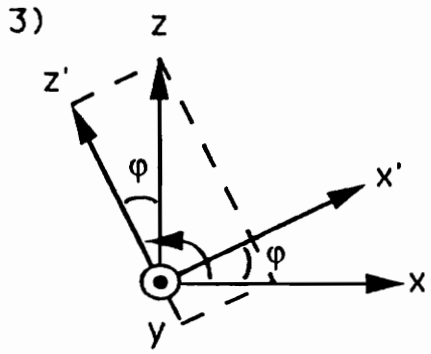

rotation around the y axis

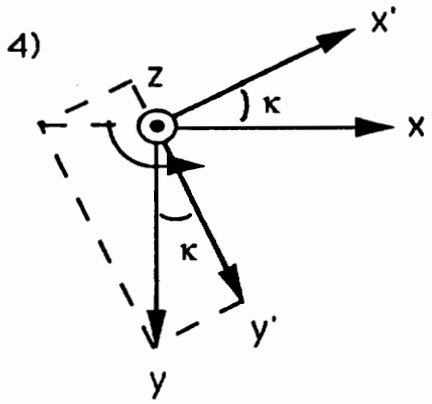

rotation around the z axis

Figure A

VITA

Melanie N. Ott was born in Baltimore, Maryland on January 25, 1964. Ms. Ott received an Associate in Engineering degree from Howard Community College, Columbia, Maryland. In December of 1989 she received a Bachelor of Science in Electrical Engineering from Virginia Polytechnic Institute and State University (Virginia Tech). In October of 1993 she received a Master of Science degree in Electrical Engineering from Virginia Tech.

Ms. Ott's professional interests include development of optical sensing techniques with emphasis on electro-optic materials and devices.

Melanie N. Ott